UNIVERSITY OF CAPE TOWN
IYUNIVESITHI YASEKAPA • UNIVERSITEIT VAN KAAPSTAD

A patient–specific FSI model for vascular access in haemodialysis

by

Andie de Villiers

Thesis Presented for the Degree of

Doctor of Philosophy in Engineering in Mechanical Engineering

University of Cape Town

March 15, 2017

cerecam
Centre for Research in Computational and Applied Mechanics

A PATIENT-SPECIFIC FSI MODEL FOR VASCULAR ACCESS IN HAEMODIALYSIS

Ph.D candidate: Anna M. de Villiers

Supervisors: Prof. B.D. Reddy and Dr. A.T. McBride

Abstract

This research forms part of an interdisciplinary project that aims to improve the understanding of haemodynamics and vascular mechanics in arteriovenous shunting. To achieve the high flow rates that enable patients with renal disease to receive haemodialysis, a fistula is created between an artery and a vein. The patency rate of fistulas, especially those located in the upper arm, is low.

The approach adopted here makes use of new magnetic resonance image (MRI) technology and computational modelling of blood flow, with a view to improving therapeutic strategies of disease requiring vascular interventions. This thesis presents the construction and development of a 3D finite element model of the fluid-structure interaction in a brachial–cephalic patient–specific fistula.

An overview of the mathematical models that describe the vessel wall and fluid behaviour as well their interaction with each other is given. An Arbitrary Lagrangian-Eulerian (ALE) framework is used together with a transversely isotropic hyperelastic constitutive model for the vessel walls, while blood flow is modelled as a Newtonian fluid. A three-element Windkessel model is used to allow the fluid to move through the outlets of the computational domain without causing non–physical reflections.

Flow data acquired from MRI is used to prescribe the flow at the inlet. The parameters of the Windkessel-model at the two outlets are calibrated to resemble the flow acquired

from the 2D MRI. The model is validated against the flow patterns acquired from the 4D MRI.

The flow patterns of the blood, and stress present in the vessel are investigated. Of special significance are the flow and wall shear stress at the anastomosis. An area of very high velocity in the anastomosis is followed by an area of recirculation and low velocity. The propagation of pressure waves and their reflection at the anastomosis are studied. Areas that are subjected to low wall shear stress, high oscillatory wall shear stress or flow circulation are identified as areas where intimal hyperplasia may develop. The flow results from the simulation show good qualitative agreement with the MRI data.

Acknowledgements

First and foremost, I would like to thank and acknowledge my supervisors Professor Daya Reddy and Dr. Andrew McBride.

Professor Reddy is an outstanding role model and I have learned so much from him, both in an academic sense and in his approach to life. His work ethic and the way that he treats people have challenged and inspired me. The gentle manner he uses when correcting ideas has made a lasting impression on me. He has exposed me to a wide range of subject matter and promoted critical thought by sending me to conferences and organising seminars at Cerecam.

Dr. McBride is my hero. I appreciate the countless hours he spent helping me to diagnose problems, explaining mistakes and thinking of new ways to tackle obstacles. His big-hearted care and patience guided me through many tears of despondency. He played an enormous role in building my knowledge and confidence.

I would like to thank everyone that formed part of the multidisciplinary project for their contribution. The principal investigator of the project "Cardiovascular MRI and Modelling" is Professor Thomas Franz. Patient selection and conduct of MRI procedures were carried out under the supervision of Professor Delawir Kahn (Surgery) by Dr. Jennifer Downs. Development of MRI protocols and data analysis were carried out under the supervision of Professor Ernesta Meintjies (MRC Unit on Medical Imaging) by Stephen Jermy. Dr. Bruce Spottiswoode assisted with the capturing and processing of data. Craig Basson spent many hours processing the MRI data to create patient–specific geometries. Winston Guess worked on a parallel project and I am grateful for the exchange of ideas between us.

Cerecam's tea room facilitated many insightful conversations. It would have been difficult to stay motivated without the daily jokes and encouragement that could be found here during lunch time. I would like to thank each member of Cerecam who all contributed in a unique way to ideas contained in this thesis and to many stimulating discussions about life and politics. I am especially grateful for all the advice on computer–related issues I received from Ritesh Rama, Timothy Povall and Maien Hamed. I would also like to thank Professor Daya Reddy in his capacity as director of Cerecam for creating an atmosphere that made coming to the lab a joy.

I am extremely thankful for the support, love and "willing ears" I received from family and friends. I would like to thank Jana, Rudolf, my extended family, my in-laws, my second mother Joan, my sisters Ria and Brechtje and my loving mother Annamie for their constant encouragement. The memories of my father were a source of strength to me. Lastly, I would like to thank my rock and husband Willem for his boundless support, patience and unconditional love.

To have the opportunity to tackle a Ph.D is a wonderful privilege. The extent of the impact these years had on me can not be captured by a thesis. I have learned a great deal academically and my thought horizons have expanded in many other directions as well. God's providence is abundant. Soli Deo Gloria.

Contents

List of Figures

List of Tables

Nomenclature

$\boldsymbol{a}$	acceleration
$\boldsymbol{A}_i$	matrix associated with i-th fibre direction
$\boldsymbol{a}_i$	vector associated with i-th fibre direction
$\boldsymbol{Q}$	orthogonal tensor
$\boldsymbol{R}$	rotation component of deformation gradient
$\boldsymbol{T}$	Piola-Kirchoff traction vector
$\boldsymbol{t}$	Cauchy traction vector
$\boldsymbol{U}$	stretch component of deformation gradient
$\boldsymbol{C}$	Cauchy-Green strain tensor
$\boldsymbol{c}$	convective velocity
$\boldsymbol{F}$	deformation gradient
$\boldsymbol{g}$	traction on boundary
$\boldsymbol{N}$	normal in material configuration
$\boldsymbol{n}$	normal in deformed configuration

$\boldsymbol{P}$ first Piola-Kirchhoff stress tensor

$\boldsymbol{S}$ second Piola-Kirchhoff stress tensor

$\boldsymbol{S}_0$ pre-stress tensor

$\boldsymbol{u}$ displacement

$\boldsymbol{v}$ velocity

$\boldsymbol{x}$ position

A Jacobian matrix of residual or tangent

C capacitance

D vessel diameter

$D_{\boldsymbol{u}}$ directional derivative in the direction of $\boldsymbol{u}$

I invariants of tensor

J volume ratio

J_q mapping from reference element

k_1 stress-like parameter associated with fibres

k_2 non-dimensional parameter associated with fibres

p pressure

p_0 initial pressure

Q flow

R resistance

R_d downstream resistance

t time

w_q quadrature weights

α mesh diffusion parameter

α_m time integration parameter

α_f time integration parameter

β time integration parameter

$\mathcal{A}$ tangent in terms of $\boldsymbol{P}$

$\mathit{\Gamma}$ boundary of domain

γ_s strong damping coefficient

γ_w weak damping coefficient

γ time integration coefficient

κ dispersion of fibres

λ stretch

ν viscosity

$\mathit{\Omega}$ domain

$\boldsymbol{\phi}$ motion

$\mathit{\Psi}$ free-energy function

$\boldsymbol{\Phi_0}$ mapping from material to spatial domain

$\boldsymbol{\Phi}$ mapping from reference to spatial domain

ϕ weight functions

Π potential energy

$\boldsymbol{\Psi}$ mapping from reference to material domain

ρ density

ρ_∞ spectral radius

$\boldsymbol{\sigma}$ Cauchy stress

τ relaxation parameter

ϱ line search damping parameter

Subscripts

0 variable in material configuration

D Dirichlet

f fluid

fib fibres

g ground matrix

i interface

iso isochoric

m mesh

N Neumann

s solid

t variable in spatial configuration

vol volumetric

1

Introduction

This research forms part of an interdisciplinary project that aims to improve the detailed understanding of haemodynamics and vascular mechanics in arteriovenous shunting. The shunts are studied in the form of haemodialysis access fistulas in the upper arm. A combination of new magnetic resonance image (MRI) technology and computational modelling of in vivo blood flow characteristics aims to improve therapeutic strategies and subsequent monitoring of diseases requiring vascular interventions.

This work will focus on a computational model of fluid–structure interaction (FSI). While several models exist for vessel walls and blood flow as well as strategies for their interaction (e.g. [51, 54, 82, 90]), a comprehensive patient–specific FSI model of arteriovenous vascular access configurations, that is, verified by in vivo data, does not exist.

An important aim is to use patient–specific geometry and inlet conditions for the problem derived from MRI data. The MRI data will add another benefit, which is the ability to validate the model.

1.1 Context

The most common treatment for end stage renal disease (ESRD) is haemodialysis. During haemodialysis blood is obtained from the body by inserting a tube into a blood vessel. The blood is circulated though a filter that removes fluids and waste products before returning to the body. To achieve the high flow rates necessary to make haemodialysis possible (at least 350 ml/min [69]), an arteriovenous shunt is formed to bypass terminal resistance (Fig. 1.1). To avoid recirculation and vein collapse, the access blood flow should be at least 100 ml/min higher than the required flow for dialysis [4]. In more proximal access sites, where the brachial artery is connected to either the basilic vein or the cephalic vein, developed flow can be as high as 1000-2000 ml/min [92]. The resulting flow rate is up to 30 times higher than normal flow rates [53].

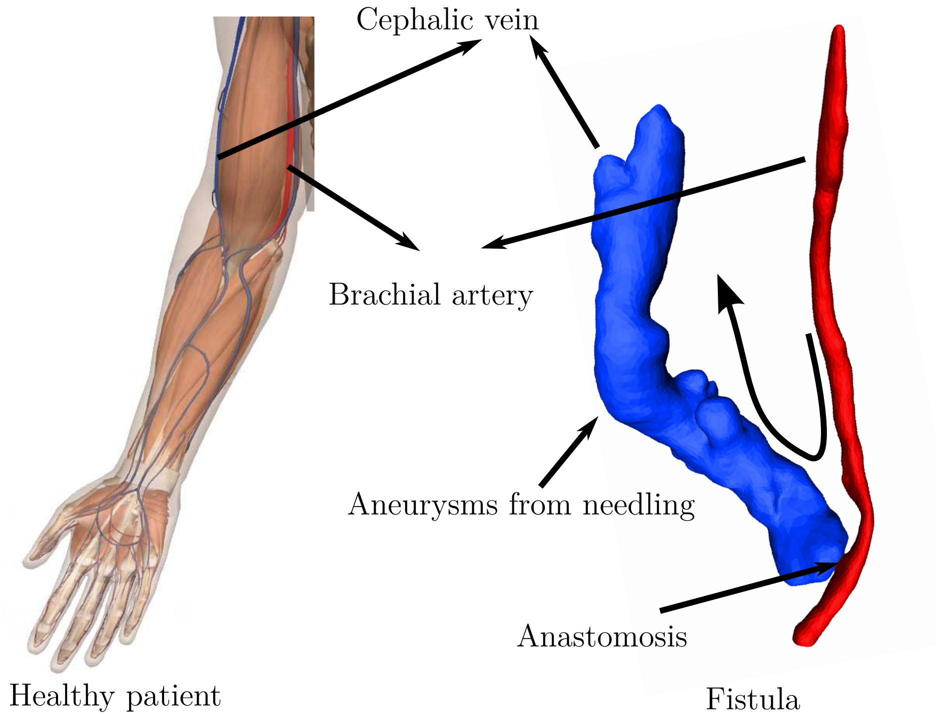

Fig. 1.1: Anatomy of a healthy patient showing the site where a fistula is formed (left), and a MRI of a patient–specific fistula (right).

The preferred form of vascular access is the arteriovenous fistula (AVF), a connection between the artery and vein [4]. When a patient's native vasculature does not allow a fistula or when there is no time to wait for the fistula to mature, an artificial arteriovenous graft (AVG) is used to connect the artery with the vein. There is however a greater risk of infection and intimal hyperplasia, the thickening of the innermost layer of a blood vessel, when using a foreign material. Because of the high failure rates of accesses, surgeons choose the most distal site available to preserve proximal vessels for later procedures.

The patency rates, or time that it remains without obstruction, of AVGs are lower than those of AVFs [25]. The primary pathology of vascular access is thrombosis. Thrombosis is caused by progressive stenosis, abnormal narrowing in the blood vessel, which is primarily found at the heel and toe of the anastomosis and also in the vein downstream of the junction where flow is turbulent [45].

The flow in the vein changes significantly after vascular access creation making the haemodynamics of the AVF and AVG unique in the vasculature; the pressure increases from about 20 mmHg to between 60 mmHg and 120 mmHg, flow increases and changes from steady to pulsatile and the wall shear stress (WSS) is much higher. The combination of pulsatile flow and the high WSS creates high oscillatory wall shear stress (OSI) and large spatial and temporal gradients of the wall shear stress. To complicate matters further, pseudo–aneurysms may form as a result of the frequent needling necessary for dialysis. These changes in conjunction with elastic property mismatch between the graft and blood vessel, the angle between the graft (or artery) and the vein and vein wall vibrations [65] cause intimal hyperplasia (IH). IH is the underlying mechansim of the stenosis [92].

There have been various approaches aimed at improving the computational modelling of vascular access. Huberts et al. [53] developed a 1D model to predict the post–operative flow for vascular access surgery using a network approach. To study flow features such as recirculation, stagnation and separation in more detail computational fluid dynamics (CFD) has been used [14, 15, 20, 65, 77]. Most CFD studies simulated blood as a Newtonian fluid, but the effects of shear thinning have been investigated [32, 85]. CFD models have been used to study different configurations of AVFs [32] and catheter angles for AVGs [85]. Validation of these models remains a difficult task; some researchers compare their results to data from in vitro studies or in vivo flow obtained by Doppler anemometry.

Compared to the abundant CFD studies of arteriovenous shunts, FSI studies are rare. An FSI model might lead to new insights with regard to the onset of IH by including stresses in vessel walls and pressure wave propagation in the investigation. Ngoepe et al. [76] developed a coupled numerical tool to study both haemodynamics of blood and solid mechanics of the blood vessels in a simplified artery–graft–vein configuration. Decorato et al. [29] found that WSS is overestimated by 10-13% using rigid wall simulation in a patient–specific AVF. Both these studies used a partitioned approach for the interaction by coupling two commercial codes. A study by McGah et al. [72] coupled a finite element code to a commercial fluid flow solver. There appear to be no studies in the literature that use a monolithic approach in FSI investigations of arteriovenous shunts.

1.2 Objectives

The aim of this thesis is to study the FSI of patient–specific fistulas by employing finite element simulations. The results from this analysis will contribute to improved haemodialysis procedures such as specifying the optimal angle for the anastomosis.

The objectives of this thesis are to:

- develop a finite element code using an open source finite element library deal.II [8], for a 3D FSI simulation;
- verify isolated parts of the model against benchmark problems in literature;
- include non–reflecting boundary conditions for the outlet;
- create patient–specific geometry from MRI data;
- obtain inflow conditions from MRI data;
- validate the model with MRI data;
- compare wall shear stress, spatial and temporal gradients of wall shear stress and oscillatory wall shear stress to regions where intimal hyperplasia may develop;
- demonstrate how the model will shed light on flow features where MRI flow data is not available.

1.3 Methodology

The interaction of an incompressible Newtonian fluid and an incompressible transverse isotropic hyperelastic structure will be studied, using a monolithic approach within a ALE framework to implement the FSI model. The finite element method will be used to find approximate solutions for the governing differential equations. For this purpose the C++ based finite element library deal.II [8] will be used. The aim of deal.II is to enable a rapid development of finite element codes, by employing a program library that takes care of details such as handling degrees of freedom, input of meshes and output of results in graphics formats. A deal.II finite element code for a monolithic 2D fluid–structure problem is available [99]. This code can be extended for the specific geometry, materials and boundary conditions necessary for our problem.

Results from processed MRI data will be used to calibrate the material parameters used in the constitutive relations.

1.4 Thesis overview

The structure of the thesis is as follows.

Chapter 2 gives a brief overview of the available literature on the different parts needed for a complete model of vascular access. These parts comprise blood, the vessel wall, fluid–structure interaction and boundary conditions. Attention is given to the rheology of blood and the assumptions that can be made at high shear rates. One section elaborates on the histology of the vessel walls in order to understand the mechanical properties of the different layers of the walls. The need to use the Arbitrary Lagrangian–Eulerian (ALE) framework for the fluid–structure interaction is explained. The way that the MRI data is used for boundary conditions and geometry is mentioned, as well as a realistic approach to represent the downstream vasculature.

The continuum mechanics of the ALE framework are introduced in Chapter 3. The notation to differentiate between the spatial, reference and material domains is given, along with the stress measures that will be used in the governing equations. The balance equations and equation describing the mesh motion are given in the strong form and weak form. Attention is given to the constitutive model chosen to represent the fibre–reinforced vessel wall. The temporal and spatial discretizations are also discussed. The last section gives an overview of how the equations are solved with emphasis on the form of the linearized stress tensors.

The considerations necessary for biomedical applications are discussed in Chapter 4. The inlet and outlet boundaries result from truncating the computational domain; attention is given to prescribing the boundary conditions in such a way that the waves can move unhindered through the domain. The process followed to generate a computational mesh for patient–specific geometries is discussed. The generated geometry is not in a stress free configuration; the method used to determine the pre–stress is introduced along with a method to determine the local fibre directions.

Chapter 5 elaborates on the numerical and computational implementation of the governing equations. A number of algorithms are shown to illustrate aspects of the deal.ii implementation. Attention is given to the form of the linear system of equations and the tools available to solve these equations using multiple processors.

Results from the patient-specific simulations are shown in Chapter 6. Each part of the code is verified separately by comparing results to those from benchmark tests. The influence of numerical and physical damping on the flow and pressure are shown. Flow results from the patient-specific simulation are compared to those acquired from MRI. The calculated wall shear stress and oscillatory wall shear stress are presented and discussed. Finally, flow features in a fistula of a patient where the geometry but not the flow data is available are investigated using the model.

Chapter 7 summarises the findings and contribution of this work, discusses the shortcomings, and recommends areas for future investigations.

2

Biomechanics of the fistula

This chapter gives an overview of the literature on models of vascular access.

A model of the vascular access consists of different parts (see Fig. 2.1) to describe the fluid dynamics of the blood, the solid mechanics of vascular walls, and the fluid–structure interaction. Attention will also be given to the various boundary conditions.

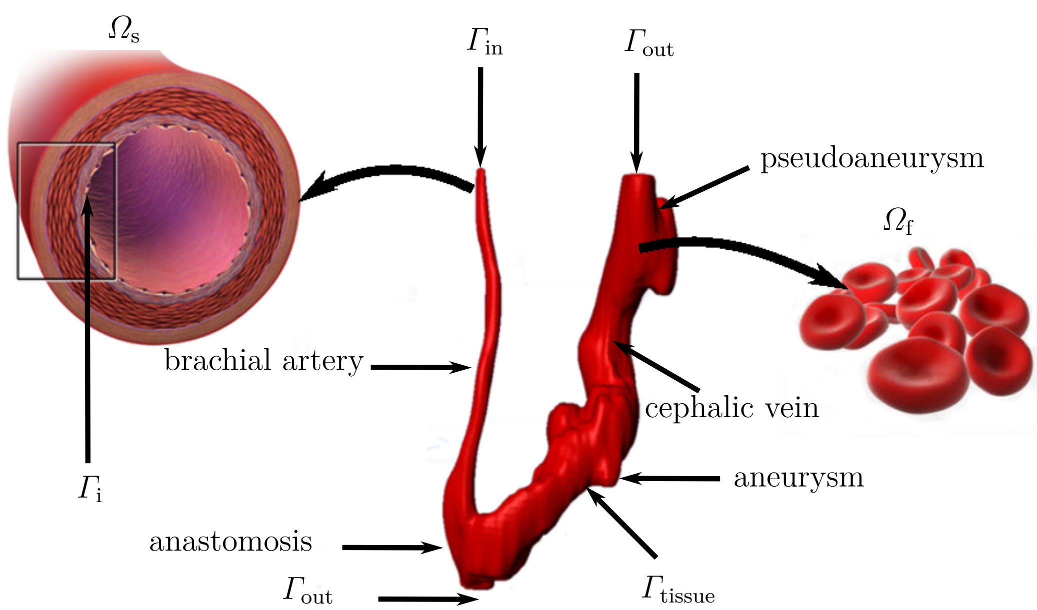

Fig. 2.1: The solid and fluid domains Ω_s and Ω_f, interface Γ_i, inlet and outlet boundaries Γ_{in} and Γ_{out} and surrounding soft tissue Γ_{tissue}.

2.1 Blood flow

The rheology of blood is complex. Strictly speaking blood is a visco–elastic fluid which exhibits thixotropic behaviour, but these effects are negligible [37]. Blood is composed approximately of half plasma and the other half of cells suspended in the plasma. The bulk of these particles are red blood cells and their influence on the rheology can be observed. The tendency of red blood cells to form rouleaux that couple different fluid regions increases the viscosity of blood at low shear rates.

At high shear rates red blood cells align their longitudinal axes with streamlines thereby decreasing the viscosity. Thus blood behaves like a shear–thinning fluid. In large vessels blood is assumed to be a Newtonian fluid. This is due to the fact that for shear rates greater than $100\,\mathrm{s}^{-1}$ the viscosity of blood can be treated as constant [33]. Non–Newtonian effects become more apparent in smaller vessels such as the brachial artery [16, 17]. It is assumed that the increased flow rate in the brachial artery as a consequence of the shunt will increase the shear rate to such an extent, compared to that in a brachial artery without a vascular access, that Newtonian flow will again be a good first approximation.

Although most researchers have modelled flow as Newtonian in vascular access regions [29, 77, 93], some researchers have used a non–Newtonian fluid when simulating flow in an AVF [32]. No comparison between Newtonian and non–Newtonian flow in the AVF has been made. This work will be confined to Newtonian fluids.

High Reynolds and Womersley numbers reflect that inertial forces dominate flow in vascular access regions. Although not often higher than 2000 [35], Reynolds numbers of 800 - 1600 have been reported [32, 61, 64, 85]. This is much higher than elsewhere in the body, except the aorta, and must be kept in mind when deciding on the mesh size used in the computational model. Womersley numbers between 6.25-9.4 [91] show that the velocity profile is somewhere between parabolic and flat and that there might be a slight phase lag between flow and pressure gradient.

2.2 Vessel wall

The walls of the arteriovenous shunt consist of two parts for an AVF, namely, the artery and the vein. Although these sections differ in function and material properties, all healthy vessels (in particular the brachial artery and cephalic vein) can be modelled as hyperelastic materials.

Arteries are elastic vessels that expand when a pressure pulse travels through them. The distensibility at the aorta is the greatest ($\frac{\triangle \mathrm{D}}{\triangle p \times \mathrm{D}} \approx 40 \times 10^{-3}$[/kPa], D denotes the vessel diameter and p the pressure) and diminish to more distal vessels such as the brachial, carotid (both$\approx 20 \times 10^{-3}$[/kPa]) and the radial artery ($\approx 5 \times 10^{-3}$[/kPa]) [78]. Veins experience low nonpulsatile pressure and act as the blood reservoirs of the body. The structure of the blood vessels is complex and a balance between accuracy and computational cost must be found when selecting a model.

Blood vessels consist of three layers: the intima, media and adventitia (Fig. 2.2). The intima is a very thin layer of endothelial cells that does not contribute much to the mechanical properties of the vessels. The media consists of smooth muscle cells and elastin and collagen fibrils. The media of the artery is the most significant layer mechanically. In veins the media is thinner, more muscular and does not share the contractile nature of the arterial media. The adventitia is the outermost layer of the artery and its thickness varies strongly with location. Its collagen fibrils are arranged in helical structures and renders the adventitia much less stiff in low pressures than the media. At higher pressures, as the fibres reach their straightened lengths, the adventitia becomes stiffer to prevent the vessel from overstretch and rupture [51].

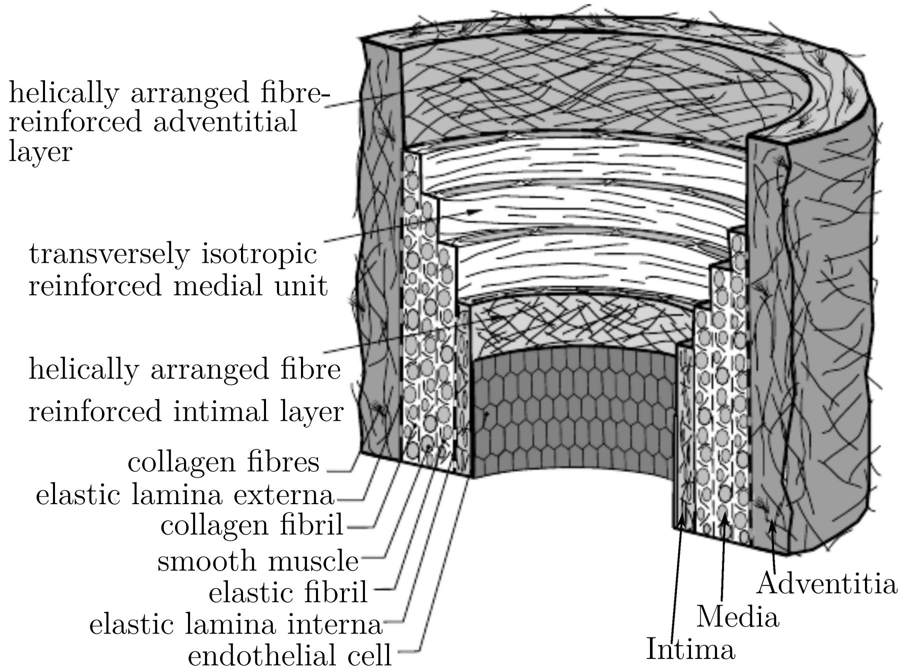

Fig. 2.2: Structure of vessel wall [41].

From an engineering point of view blood vessels can be considered as multi–layered incompressible composites reinforced by two families of symmetrically arranged fibres. It is possible to extend the strain–energy function of an isotropic hyperelastic ground substance to include directional reinforcement relatively easily. This is done by an additive split into a part associated with isotropic deformations and a part associated with deformations in the fibre direction. The model by Holzapfel et al. [51] employed an exponential function for the description of the strain energy stored in the collagen fibres, motivated by the strong stiffening effect of each layer at high pressures. This model has been widely used in literature to model arteries. This model has also been extended to other biological tissue including veins [3, 6, 83]. Some extensions have been proposed to the original model to include visco–elasticity [50], elasto–plastic behaviour that manifests when pressures outside of the physiological range are experienced [40], a dispersion parameter that describes the degree of anisotropy [41] and automatic identification of planar organisation [81]. These will not be included in the present study. The free energy function that will be used for the healthy vessels is taken from [51].

After the shunt has been created the mean pressure in the vein rises significantly. To keep the wall shear stress within a physiological range, blood vessels remodel themselves. This remodelling is necessary for the maturation of the vascular access. Remodelling will not be included in our computational model.

The geometry obtained by medical imaging does not represent a stress–free state. Thus we need to account for the pre–stress in the model.

The top row of Fig. 2.3 shows cross–sections of arteries *in vivo* at normal physiological pressure. When these vessels are excised from the body they collapse at zero transmural pressure. This is called the no–load state and is shown in the middle row of the figure. On the bottom row the vessels are shown at their zero stress state. These were obtained by making a radial cut in the arteries, causing them to spring open into sectors and reduce in circumferential length.

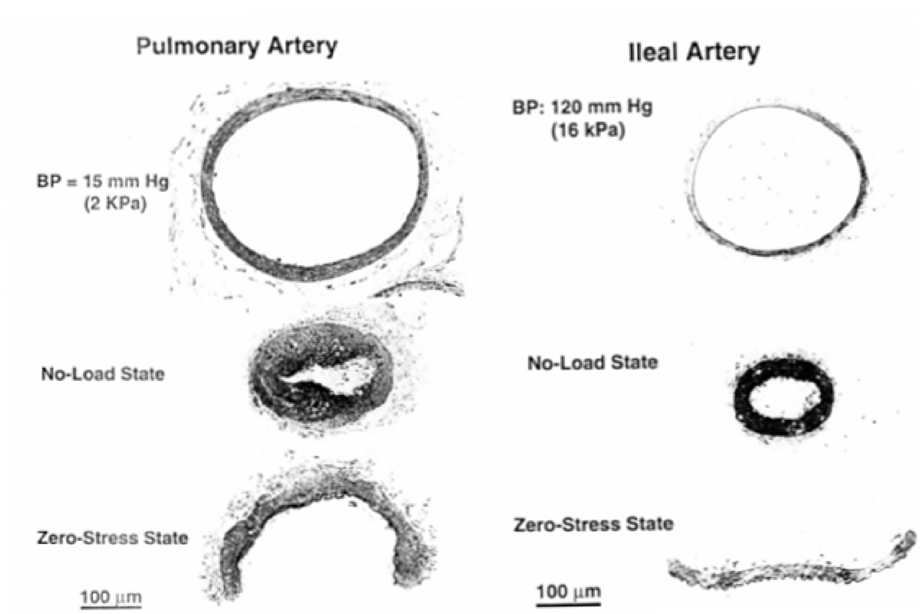

Fig. 2.3: The *in vivo*, no–load and zero–stress states of arteries [39].

The pre–stress in the no–load state can be determined analytically for very simple geometries from the no–stress state if the opening angle is known [2, 51]. The stress present in the geometry extracted from medical imaging is *in vivo* and thus not associated with the no–load state, but with a state assumed to be at equilibrium at physiological pressures.

Several strategies have been suggested to determine the prestresses that exist in the vessels *in vivo*. Some researchers have aimed at determining the unstressed configuration by inverse analysis and used that as their reference state [89]. Others attempted to determine the stress present in the *in vivo* geometry. To determine the no–load state from the *in vivo* data inverse design, iterative procedures to find a pre–stress, or a modified updated Lagrangian formulation to find a deformation gradient from the no–load state, have been used [43, 52, 68]. The approach adopted here is that presented in [52].

2.3 Fluid–structure interaction

As mentioned in Section 1.1, most of the attempts in the literature to understand intimal hyperplasia in vascular access make use of CFD without accounting for deformation of the vessel. This approach precludes pressure wave propagation and material mismatch, overestimates WSS and disregards stresses in the wall tissue. To include these effects a FSI model should be considered.

In pure structural problems the Lagrangian framework is used: the mesh deforms with the material. In pure fluid problems the Eulerian framework is used: the mesh is fixed and the material moves through it. In a fluid–structure problem the domain of the fluid changes in response to the motion of the solid and the Eulerian framework is not adequate. There are many strategies to model the interaction between a fluid and structure. The Arbitrary Langrangian Eulerian (ALE) formulation [54] is a robust framework and is widely used for many applications, including blood flow [27, 48, 62].

A staggered approach that results in a loose coupling of the equations has been used in different applications [22, 55, 66]. The advantage of such a method is that well–validated fluid and structure solvers can be used: see for example [29, 76]. For some combinations of physical parameters numerical instabilities may be encountered in loosely–coupled schemes due to the "added mass effect". When the densities of the fluid and solid are comparable or when the domain has a slender shape, as in the case of blood flow in the body, a loosely–coupled scheme may feature instabilities. Several iterations may be necessary to achieve convergence, making it computationally expensive. For these same combinations of parameters strongly–coupled implicit algorithms also experience convergence problems [21]. During the last decade researchers have worked on methods to stabilize loosely–coupled schemes [44, 57]. Other researchers have focused on ways to achieve faster convergence for the monolithic case by using pre–conditioners [10, 46].

2.4 Boundary conditions

There are several boundary conditions that need to be prescribed to approximate the effects that the rest of the body has on the section of blood and blood vessels to be modelled. In addition to the inflow and outflow conditions of both the fluid and solid, a condition that simulates the effect of the soft tissue that surrounds the artery is necessary. It is not as straightforward to impose these conditions as prescribing a displacement, velocity, pressure or traction. There are different options available in the literature for these boundary conditions, with varying levels of complexity. A choice needs to made that balances ease with accuracy.

The brachial artery and cephalic vein are surrounded by soft tissue that keeps these in position but allows them to distend and contract. To model this, the simplest choice would be to apply a constant pressure on the outer wall of the vessel. A more accurate representation would be to model the soft tissue as an elastic solid. A Robin boundary condition offers an attractive balance between simplicity and accuracy. With this type of boundary condition a linear algebraic stress–displacement constitutive relation on the external wall can be imposed [27, 75]. Linear elastic behaviour was assumed.

Values for the inflow fluid boundary have been obtained from the MRI data. For blood flow the maximum velocity in the artery is combined with a suitable velocity profile and prescribed over time. Although the vessel walls are too small to be seen with MRI, the displacement of the fluid domain may be used to prescribe the movement of the vessel wall at the inlet.

Due to the pulsatile nature of blood flow, the outflow conditions are complex. The pressure wave should be allowed to propagate through the outflow boundary without creating non-physiological reflections. The resistive and capacitive effects of distal vessels should also be taken into account when deciding on suitable boundary conditions.

The simplest approach is to prescribe pure resistive boundary conditions, whereby a constant relationship between mean pressure and flow rate is imposed. A slightly more complex option is to use an impedance boundary condition. Impedance allows for a phase shift between pressure and flow pulses. Both resistance and impedance based boundary conditions can be included in the weak form of the governing equations and are thus relatively simple to implement [96].

The next level of complexity would be to attach a Windkessel model at the outflow boundary. The Windkessel model is an electric circuit analogue that consists of a proximal resistance in series with a parallel layout of a capacitance and a distal resistance. It is also possible to include this arrangement in the weak form [97]. A more sophisticated approach to obtain accurate boundary conditions would be to include the 3D model in a multi–scale system model of the whole body. A 1D model would be used to model large arteries and would be connected to the 3D model [36]. The creation of a 1D model of the whole body is however outside the scope of this research.

Simulation divergence due to backflow may occur in vessels with complex geometries such as the presence of anastomoses or increased sectional area. The issue emanates from the use of Neumann boundary conditions at the outlet face, for which information with regard to the velocity profile is not specified. This typically happens when convective effects present in the neglected parts of the domain are not taken into account when imposing the boundary conditions. This can happen if there is negative flow over the entire outlet face, if there are localized areas of flow reversal (even for bulk outward positive flow), or in the case when a 0D or 1D model are coupled to the outlet and pass pressure information to the domain without velocity profile information.

The simplest solution would be to artificially elongate the outlets by adding straight sections to the geometry and in so doing dissipating the vortices before they reach the outlet. This might change the local hemodynamics and there is an additional computational cost that makes this approach undesirable. In [74] the authors compare three methods currently in use for solving the issue of backflow divergence in finite element solvers. A method first used in [11] was found to have the highest robustness, the least impact on the flow field, and was easiest to implement of the methods compared. This method is called outlet stabilization and is implemented by modifying the weak formulation by adding a backflow stabilization term for the Neumann boundaries. The stability of this method was increased in [74] by scaling this term. The Neumann boundary contains a pressure calculated from a lumped parameter model that can be chosen with varying degrees of complexity and accuracy.

2.5 Chapter summary

There are various components of the fistula that need to be modelled in a computational study. Blood at high shear rates will be modelled as a Newtonian fluid. The vessel wall of an artery and vein will be modelled by a fibre–reinforced hyperelastic material. To make the fluid–structure interaction possible the ALE framework will be used. The boundary conditions present several difficulties. An elastic or visco–elastic structure will be used to represent the soft tissue surrounding the vessels. The directional do–nothing outlet condition will ensure stability when back–flow is present. A 0–D Windkessel model will be used so that the waves can pass unhindered through the outlet.

In the next chapter we introduce the ALE framework and balance equations to be solved. We develop the weak form and the discretized equations and discuss the solution of the nonlinear equations.

3

The biomechanical model and its solution

This chapter deals with the theoretical foundations of modelling fluid–structure interactions. The first section introduces the key concepts of continuum mechanics that will be necessary to set up the governing equations. The second section introduces the material models used to model the arterial wall and blood. The third section shows the governing equations, the variational system in the reference configuration, and time and spatial discretization of these equations. The last section considers strategies to solve the linear equations that arise from discretization.

3.1 Continuum mechanics

As it would be too computationally intensive to model blood and blood vessels at the micro–structural level, we adopt a continuum approach. This section will introduce the concepts and the accompanying notation for the study of motion and deformation (kinematics) and the study of stress (kinetics) in a continuum.

As most of these concepts are widely established in the continuum and computational mechanics community seperate references to each equation will not be given. The exposition of kinematics and stress follows the same sequence as Holzapfel [49]. For the outline of the ALE setting we followed the description by Belytschko *et al.*[12].

3.1.1 Kinematics

The relationship between a deforming continuum and a grid superimposed on the domain (mesh) is determined by its kinematical description. The two classical descriptions of motion, Lagrangian (or referential) and Eulerian (or spatial), both have advantages and drawbacks. The Lagrangian description is mainly used in structural mechanics. It has the ability to easily track moving interfaces and free surfaces. Its disadvantage is the inability to preserve good quality meshes without remeshing when subjected to large deformations. The Eulerian description is predominantly used in fluid mechanics. It can handle large distortions of the continuum but its drawback is the inability to track moving interfaces accurately. The ALE description aims to combine the advantages of the Lagrangian and Eulerian descriptions whilst diminishing their drawbacks.

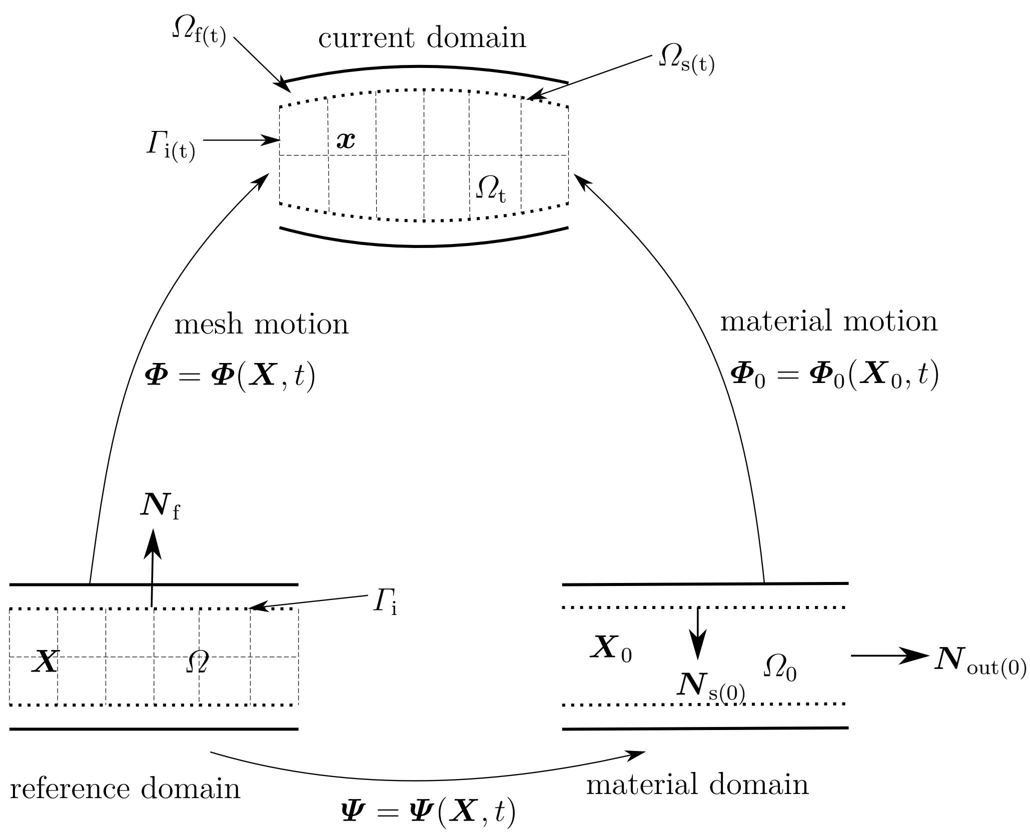

Fig. 3.1: Domains for the ALE framework.

In order to write the differential equations in the ALE framework, various domains must be defined (see Fig. 3.1). The reference domain is denoted by Ω and the material domain by Ω_0. The deformed (or current) configuration is denoted by Ω_t. At $t = 0$, the position vector $\boldsymbol{X}$ denotes the referential positions of particles in the reference domain Ω. At $t = 0$, Ω coincides with the material domain Ω_0 and the current domain Ω_t. The position vectors $\boldsymbol{X}_0$ in the material domain and $\boldsymbol{x}(0)$ in the current domain also coincides with $\boldsymbol{X}$ at $t = 0$. The boundary of the reference domain is denoted by $\partial\Omega = \Gamma = \Gamma_{\mathrm{D}} \cup \Gamma_{\mathrm{N}}$, where Γ_{D} denotes the Dirichlet part of the boundary and Γ_{N} denotes the Neumann part. Γ_D and Γ_N are nonoverlapping. Similarly the boundaries of the material and current domains are denoted respectively by Γ_0 and Γ_{t}.

We further differentiate between the subdomain associated with the fluid, denoted by subscript f, and the subdomain associated with the structure, denoted by subscript s. The interface between the two subdomains is denoted by $\Gamma_{\mathrm{i}} = \partial\Omega_{\mathrm{s}} \cap \partial\Omega_{\mathrm{f}}$ in the material domain.

To describe the *motion* of a material particle we define different maps. The material domain Ω_0 is mapped from the reference domain Ω by $\boldsymbol{X}_0 = \boldsymbol{\Psi}(\boldsymbol{X}, t)$. The mesh motion is mapped from the reference domain to the spatial domain by $\boldsymbol{x} = \boldsymbol{\Phi}(\boldsymbol{X}, t)$. The motion of the material is mapped from the material domain to the spatial domain by the material map $\boldsymbol{x} = \boldsymbol{\Phi}_0(\boldsymbol{X}_0, t)$.

For a purely Lagrangian approach, $\boldsymbol{\Psi}(\boldsymbol{X}, t) = \boldsymbol{I}$ and the mesh moves with the material ($\boldsymbol{\Phi}(\boldsymbol{X}, t) = \boldsymbol{\Phi}(\boldsymbol{X}_0, t)$). For a purely Eulerian approach the mesh does not move ($\boldsymbol{\Phi}(\boldsymbol{X}, t) = \boldsymbol{I}$). In a ALE framework the mesh motion and particle motion are independent of each other (see Fig. 3.2).

The *displacement* $\boldsymbol{u}_0$ of the material relates its position $\boldsymbol{X}_0$ in the material domain to its position $\boldsymbol{x}$ in the deformed configuration at time t, and is defined by

$$\boldsymbol{u}_0\left(\boldsymbol{X}_0, t\right) = \boldsymbol{x} - \boldsymbol{X}_0 = \boldsymbol{\Phi}_0(\boldsymbol{X}_0, t) - \boldsymbol{X}_0. \tag{3.1}$$

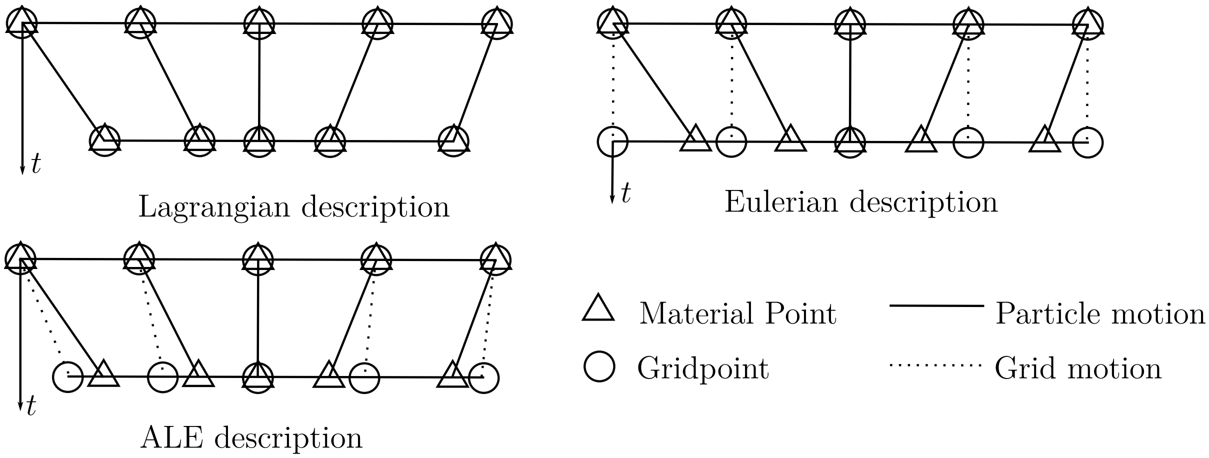

Fig. 3.2: Domains for the ALE framework (adapted from [31]).

Similarly the *mesh displacement* $\boldsymbol{u}$ relates $\boldsymbol{X}$ to $\boldsymbol{x}$ by

$$\boldsymbol{u}\left(\boldsymbol{X}, t\right) = \boldsymbol{x} - \boldsymbol{X} = \boldsymbol{\Phi}(\boldsymbol{X}, t) - \boldsymbol{X}. \tag{3.2}$$

The *velocity* and *acceleration* fields are defined as the first and second derivatives of the material motion $\boldsymbol{\Phi}_0$ with respect to time t, holding $\boldsymbol{X}_0$ fixed:

$$\boldsymbol{V}_0\left(\boldsymbol{X}_0, t\right) = \frac{\partial \boldsymbol{\Phi}_0(\boldsymbol{X}_0, t)}{\partial t}, \qquad \boldsymbol{A}_0\left(\boldsymbol{X}_0, t\right) = \frac{\partial \boldsymbol{V}_0(\boldsymbol{X}_0, t)}{\partial t} = \frac{\partial^2 \boldsymbol{\Phi}_0(\boldsymbol{X}_0, t)}{\partial t^2}. \tag{3.3}$$

Because $\boldsymbol{X}_0$ can be written in terms of $\boldsymbol{x}$ and t, the spatial description of the material velocity and acceleration fields are given by:

$$\begin{aligned} \boldsymbol{V}_0\left(\boldsymbol{X}_0, t\right) &= \boldsymbol{V}_0\left(\boldsymbol{\Phi}_{\boldsymbol{0}}^{\boldsymbol{-1}}\left(\boldsymbol{x}, t\right), t\right) = \boldsymbol{v}\left(\boldsymbol{x}, t\right), \\ \boldsymbol{A}_0\left(\boldsymbol{X}_0, t\right) &= \boldsymbol{A}_0\left(\boldsymbol{\Phi}_{\boldsymbol{0}}^{\boldsymbol{-1}}(\boldsymbol{x}, t), t\right) = \boldsymbol{A}_{\boldsymbol{t}}\left(\boldsymbol{x}, t\right). \end{aligned} \tag{3.4}$$

The *mesh velocity* and *acceleration* follow analogously to (3.3) as:

$$\boldsymbol{V}\left(\boldsymbol{X}, t\right) = \frac{\partial \boldsymbol{\Phi}(\boldsymbol{X}, t)}{\partial t}, \qquad \boldsymbol{A}\left(\boldsymbol{X}, t\right) = \frac{\partial \boldsymbol{V}(\boldsymbol{X}, t)}{\partial t} = \frac{\partial^2 \boldsymbol{\Phi}(\boldsymbol{X}, t)}{\partial t^2}. \tag{3.5}$$

The mesh velocity and acceleration have no physical meaning in an ALE mesh that is not Lagrangian. For a Lagrangian mesh, the mesh velocity and acceleration correspond to the material velocity and acceleration. For a Eulerian mesh, the mesh velocity and acceleration are equal to zero.

The *material time derivative* of a material field $F(\boldsymbol{X}, t)$ describes the rate of change of the material field as seen by an observer following the path line of a particle. It is denoted by

$$\dot{F}(\boldsymbol{X}_0, t) = \frac{DF(\boldsymbol{X}_0, t)}{Dt} = \frac{\partial F(\boldsymbol{X}_0, t)}{\partial t}. \tag{3.6}$$

The *spatial time derivative* represents the rate of change of a spatial field $f(\boldsymbol{x}, t)$ as seen by an observer that is stationed at $\boldsymbol{x}$. It is denoted by $\frac{\partial f(\boldsymbol{x},t)}{\partial t}$.

The total time derivative (material time derivative) of a spatial scalar field can be found by using the chain rule:

$$\begin{aligned}\dot{f}(\boldsymbol{x}, t) &= \dot{f}(\boldsymbol{\Phi}_0(\boldsymbol{X}_0, t))\,|_{\boldsymbol{X}_0=\boldsymbol{\Phi}_0^{-1}(\boldsymbol{x},t)},\\ &= \frac{\partial f(\boldsymbol{x}, t)}{\partial t} + \frac{\partial f(\boldsymbol{x}, t)}{\partial \boldsymbol{x}} \cdot \left.\frac{\partial \boldsymbol{\Phi}_0(\boldsymbol{X}_0, t)}{\partial t}\right|_{\boldsymbol{X}_0=\boldsymbol{\Phi}_0^{-1}(\boldsymbol{x},t)}\\ &= \frac{\partial f(\boldsymbol{x}, t)}{\partial t} + \nabla f(\boldsymbol{x}, t) \cdot \boldsymbol{v}(\boldsymbol{x}, t),\end{aligned} \tag{3.7}$$

where $\nabla f = \frac{\partial f(\boldsymbol{x},t)}{\partial \boldsymbol{x}}$.

In an ALE framework, fields are usually expressed as functions of the reference coordinates $\boldsymbol{X}$ and time t. The material time derivative for these fields can be found using an approach similar to that used to obtain (3.7), to obtain

$$\dot{f}(\boldsymbol{X}, t) = \frac{\partial f(\boldsymbol{X}, t)}{\partial t} + \frac{\partial f(\boldsymbol{X}, t)}{\partial \boldsymbol{X}} \cdot \left.\frac{\partial \boldsymbol{\Psi}^{-1}(\boldsymbol{X}_0, t)}{\partial t}\right|_{\boldsymbol{X}_0=\boldsymbol{\Psi}^{-1}(\boldsymbol{X},t)}. \tag{3.8}$$

In order to develop a relationship between the material velocity and the mesh velocity, we note that the expression for material motion $\boldsymbol{x} = \boldsymbol{\Phi}_0(\boldsymbol{X}_0, t)$ can be rewritten as a composition of functions as $\boldsymbol{x} = \boldsymbol{\Phi}_0(\boldsymbol{X}_0, t) = \boldsymbol{\Phi}(\boldsymbol{\Psi}^{-1}(\boldsymbol{X}_0, t), t)$. Using this composition of $\boldsymbol{x}$ and the chain rule, one can develop an expression for the material velocity that relates it to the mesh velocity and is given in index notation by

$$\begin{aligned} v_j &= V_{j(0)} = \dot{\Phi}_{j(0)}(\boldsymbol{X}_0, t) = \dot{\Phi}_j\left(\boldsymbol{\Psi}^{-1}(\boldsymbol{X}_0, t), t\right) \\ &= \frac{\partial \Phi_j(\boldsymbol{X}, t)}{\partial t} + \frac{\partial \Phi_j(\boldsymbol{X}, t)}{\partial X_i} \frac{\partial \Psi_i^{-1}(\boldsymbol{X}_0, t)}{\partial t}\bigg|_{\boldsymbol{X}_0 = \boldsymbol{\Psi}^{-1}(\boldsymbol{X}, t)} \\ &= V_j + \frac{\partial x_j}{\partial X_i} \frac{\partial X_i}{\partial t}. \end{aligned} \tag{3.9}$$

In index–free form, $\boldsymbol{v} = \boldsymbol{V} + \mathrm{Grad}\Phi$.

The convective velocity $\boldsymbol{c}$ is defined as the difference between the material and mesh velocities:

$$\begin{aligned} c_j = v_j - V_j &= \frac{\partial x_j}{\partial X_i} \frac{\partial X_i}{\partial t}, \\ \boldsymbol{c} = \boldsymbol{v} - \boldsymbol{V} &= \mathrm{Grad}\, \boldsymbol{x} \cdot \frac{\partial \boldsymbol{X}}{\partial \mathrm{t}}. \end{aligned} \tag{3.10}$$

It is useful to write (3.8) in terms of the spatial gradient and noting that because $\boldsymbol{x} = \boldsymbol{\Phi}(\boldsymbol{X}, t)$, we can obtain

$$\begin{aligned} \frac{\partial f}{\partial X_i} &= \frac{\partial f}{\partial x_j} \frac{\partial x_j}{\partial X_i}, \\ \mathrm{Grad}\, f &= \nabla f \cdot \mathrm{Grad}\boldsymbol{x}. \end{aligned} \tag{3.11}$$

Using this relation, the material time derivative can be rewritten as:

$$\begin{aligned} \dot{f}(\boldsymbol{X}, t) &= \frac{\partial f(\boldsymbol{X}, t)}{\partial t} + \frac{\partial f}{\partial x_j} \frac{\partial x_j}{\partial X_i} \frac{\partial X_i}{\partial t} \\ &= \frac{\partial f}{\partial t} + \boldsymbol{c} \cdot \nabla f. \end{aligned} \tag{3.12}$$

An important measure to describe the deformation of the material is the deformation gradient $\boldsymbol{F}_0$, defined by

$$\boldsymbol{F}_0\left(\boldsymbol{X}_0, t\right) = \frac{\partial \boldsymbol{\Phi}_0\left(\boldsymbol{X}_0, t\right)}{\partial \boldsymbol{X}_0}. \tag{3.13}$$

It characterizes the behaviour of motion in the neighbourhood of a material point. It can also be described as a map to transform material tangent vectors into spatial tangent vectors.

Similarly, we can define the deformation gradient $\boldsymbol{F}$ that characterizes the mesh motion in the neighbourhood of a referential point by

$$\boldsymbol{F}\left(\boldsymbol{X}, t\right) = \frac{\partial \boldsymbol{\Phi}\left(\boldsymbol{X}, t\right)}{\partial \boldsymbol{X}}. \tag{3.14}$$

The volume ratio between infinitesimal volume elements in the material and current configurations are denoted by $J_0 = \det\boldsymbol{F}_0$. Note that since $\boldsymbol{F}_0$ is invertible, and volume elements cannot have negative volumes, $J_0 > 0$. Similarly J is defined by the volume ratio between the infinitesimal volume elements in the reference and current configurations: $J = \det\boldsymbol{F}$. Note that when modelling the material motion of a Lagrangian solid $\boldsymbol{\Psi}(\boldsymbol{X}, t) = \boldsymbol{I}$ and the mesh motion and material motion is the same. Therefore $\boldsymbol{F} = \boldsymbol{F}_0$ and $J = J_0$.

Lastly we introduce the right Cauchy–Green tensor $\boldsymbol{C}$:

$$\boldsymbol{C} = \boldsymbol{F}^T\boldsymbol{F}. \tag{3.15}$$

The deformation gradient $\boldsymbol{F}$ can be decomposed in into a pure stretch $\boldsymbol{U}$ and a proper rotation $\boldsymbol{R}$:

$$\boldsymbol{F} = \boldsymbol{R}\boldsymbol{U}, \qquad \boldsymbol{R}^T\boldsymbol{R} = \boldsymbol{I}, \qquad \boldsymbol{U} = \boldsymbol{U}^T. \tag{3.16}$$

The positive–definite and symmetric tensor $\boldsymbol{U}$ is defined with respect to the material configuration and follows from (3.15) and $(3.16)_1$:

$$U^2 = UU = C. \tag{3.17}$$

3.1.2 Stress

In figure 3.3 a body is shown in the material and current configurations. $\boldsymbol{T}$ represents the first Piola–Kirchhoff surface traction vector that measures the force per unit surface area in the material configuration, while $\boldsymbol{t}$ represents the Cauchy surface traction vector that measures the force per unit surface area in the current configuration. The vectors $\boldsymbol{T}$ and $\boldsymbol{t}$ act across surface elements dS and ds with normals $\boldsymbol{N}$ and $\boldsymbol{n}$ respectively.

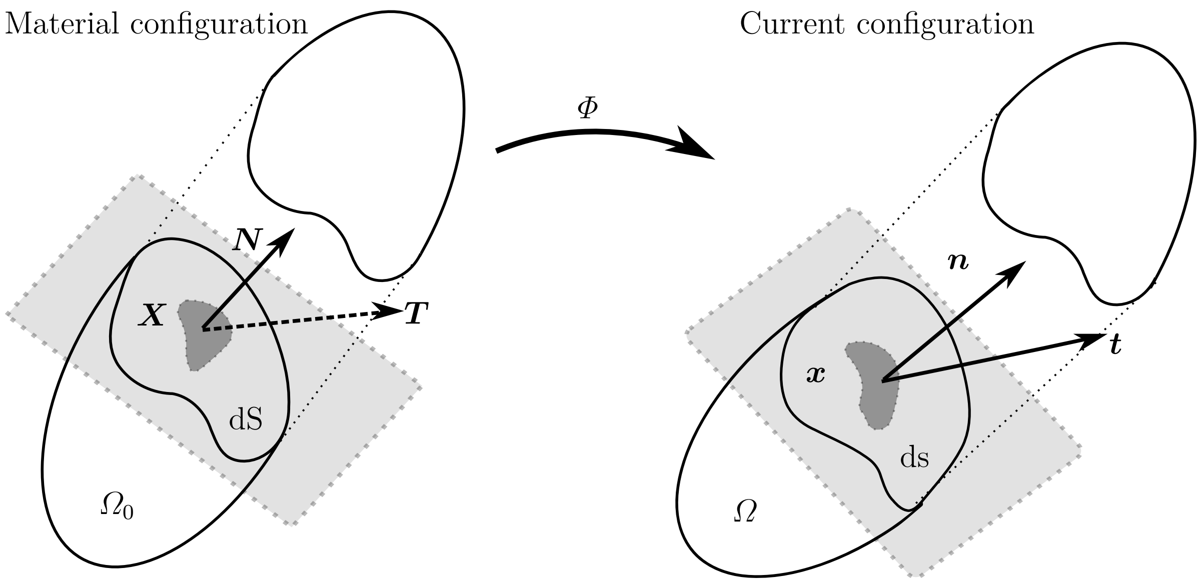

Fig. 3.3: Material and current configuration with surface traction vectors acting on infinitesimal surface elements.

Cauchy's stress theorem states that the surface traction vectors $\boldsymbol{T}$ and $\boldsymbol{t}$ depend linearly on outward unit normals $\boldsymbol{N}$ and $\boldsymbol{n}$ respectively. Thus, there exist unique second–order tensors $\boldsymbol{\sigma}$ and $\boldsymbol{P}$ such that

$$\begin{aligned} \boldsymbol{t}\left(\boldsymbol{x}, t, \boldsymbol{n}\right) &= \boldsymbol{\sigma}\left(\boldsymbol{x}, t\right)\boldsymbol{n}, \\ \boldsymbol{T}\left(\boldsymbol{X}, t, \boldsymbol{N}\right) &= \boldsymbol{P}\left(\boldsymbol{X}, t\right)\boldsymbol{N}. \end{aligned} \tag{3.18}$$

Here $\boldsymbol{\sigma}$ denotes the Cauchy stress tensor (that is symmetric from the balance of angular momentum) and $\boldsymbol{P}$ denotes the first Piola–Kirchhoff stress tensor. They are related as follows:

$$\boldsymbol{P} = J\boldsymbol{\sigma}\boldsymbol{F}^{-T}. \tag{3.19}$$

From the above, it can be seen that $\boldsymbol{P}$ is not symmetric.

Lastly the second Piola–Kirchhoff stress tensor $\boldsymbol{S}$ is introduced. $\boldsymbol{S}$ will be useful when working with hyperelastic materials. $\boldsymbol{S}$ is related to $\boldsymbol{P}$ and $\boldsymbol{\sigma}$ as follows:

$$\boldsymbol{S} = \boldsymbol{F}^{-1}\boldsymbol{P} = J\boldsymbol{F}^{-1}\boldsymbol{\sigma}\boldsymbol{F}^{-T}. \tag{3.20}$$

Thus the symmetry of $\boldsymbol{S}$ follows from the symmetry of $\boldsymbol{\sigma}$.

3.2 Governing equations

In this section the equations governing the fluid–structure interaction are presented. These equations result from conservation of mass and momentum. The equations governing the flow are written using the ALE framework and the equations governing the structure's deformation are written in the Lagrangian configuration. The interaction between the fluid and structure is prescribed by coupling conditions. An additional equation is necessary to describe the motion of the mesh in the fluid domain. This equation is arbitrary and a harmonic mesh motion is chosen.

3.2.1 Navier–Stokes in ALE framework

The viscosity of blood at high shear rates can be assumed to be constant. In fistulas flow and therefore shear rates are quite high and the blood is assumed to be Newtonian. These equations are usually written in the Eulerian framework and the total time derivative of the velocity is written as the material time derivative. In the ALE–framework the total time derivative (3.12) is used to write the the time derivative of the velocity as

$$\dot{\boldsymbol{v}}\left(\boldsymbol{X}, t\right) = \frac{\partial \boldsymbol{v}}{\partial t} + \boldsymbol{c} \cdot \nabla \boldsymbol{v}. \tag{3.21}$$

The Navier–Stokes equations in the current configuration, Ω_f, are given by

$$\begin{aligned} \rho_\mathrm{f}\left(\frac{\partial \boldsymbol{v}}{\partial t} + \boldsymbol{c} \cdot \nabla \boldsymbol{v}\right) - \operatorname{div} \boldsymbol{\sigma}_\mathrm{f} &= \boldsymbol{0} && \text{in } \Omega_\mathrm{f}, \\ \operatorname{div} \boldsymbol{v} &= \boldsymbol{0} && \text{in } \Omega_\mathrm{f}, \\ \boldsymbol{v} = \boldsymbol{v}^\mathrm{D} \text{ on } \Gamma_\mathrm{f,D}, \qquad \boldsymbol{\sigma n} &= \boldsymbol{g}_\mathrm{f} && \text{on } \Gamma_\mathrm{f,N} \end{aligned} \tag{3.22}$$

where $\boldsymbol{g}_\mathrm{f}$ is the traction prescribed on the boundary and the Cauchy stress tensor is defined by

$$\boldsymbol{\sigma}_\mathrm{f} = -p_\mathrm{f}\boldsymbol{I} + \rho_\mathrm{f}\nu_\mathrm{f}(\nabla \boldsymbol{v} + \nabla \boldsymbol{v}^T), \tag{3.23}$$

where $\boldsymbol{v}$, ρ, $\boldsymbol{\sigma}_\mathrm{f}$ and p denote the fluid velocity, the fluid density, the Cauchy stress tensor and pressure, respectively. For a Newtonian fluid the kinematic viscosity ν_f is constant. For a shear thinning or thickening fluid, ν_f is a function of the shear rate.

3.2.2 Structure equation in the material configuration

For the Lagrangian description $\boldsymbol{\Psi}(\boldsymbol{X}, t) = \boldsymbol{I}$ and thus $\boldsymbol{u} = \boldsymbol{u}_0,\ \ \boldsymbol{V} = \boldsymbol{V}_0 = \boldsymbol{v}$. Therefore the equations in the reference and material domain are identical. The balance equation in the material configuration is given by

$$\begin{aligned} \rho_\mathrm{s}\frac{\partial \boldsymbol{v}}{\partial t} - \operatorname{Div} \boldsymbol{P} &= \boldsymbol{0} && \text{in } \Omega_\mathrm{0,s}, \\ \boldsymbol{u} = \boldsymbol{u}^D \text{ on } \Gamma_{s,D}, \qquad \boldsymbol{PN} &= \boldsymbol{g}_\mathrm{s} && \text{on } \Gamma_\mathrm{s,N}, \end{aligned} \tag{3.24}$$

with $\boldsymbol{P}$ the first Piola–Kirchhoff stress tensor defined in Section 3.3.1 and $\boldsymbol{g}_\mathrm{s}$ is the traction prescribed at the boundary.

3.2.3 Harmonic mesh motion

For moderate deformation (that are found in the vessel walls) the mesh motion can be described by an auxillary Laplace equation. This is known as harmonic mesh motion. The harmonic equation in the reference configuration reads as follows:

$$\begin{aligned} -\mathrm{Div}\, \boldsymbol{P}_{\mathrm{m}} &= \mathbf{0} && \text{in} \ \ \mathit{\Omega}_{\mathrm{f}}, \\ \boldsymbol{u}_{\mathrm{f}} = \boldsymbol{u}_{\mathrm{s}} \quad \text{on} \quad \mathit{\Gamma}_{\mathrm{i}}, \quad \boldsymbol{u}_{\mathrm{f}} &= \mathbf{0} && \text{on} \quad \partial\mathit{\Omega} \cap \mathit{\Gamma}_{\mathrm{i}}, \end{aligned} \tag{3.25}$$

where

$$\boldsymbol{P}_{\mathrm{m}} = \alpha \, \mathrm{Grad}\, \boldsymbol{u}. \tag{3.26}$$

The diffusion parameter α is chosen in a way that ensures good fluid mesh quality. We follow Stein et al. [87] and scale the mesh motion equation as a function of the volume change: $\alpha(\boldsymbol{x}) = (J-1)^{\chi}$ with $\chi = 1, 2$ or 3. This means that as an element distorts it becomes more stiff and the mesh movement of the particular cell is decreased.

3.2.4 Coupling conditions

The interface between the fluid domain, $\mathit{\Omega}_{\mathrm{f}}$, and the solid domain $\mathit{\Omega}_{\mathrm{s}}$ is $\mathit{\Gamma}_{\mathrm{i}}$. The conditions on the coupling interface are given by

$$\boldsymbol{v}_{\mathrm{f}} = \frac{\partial \boldsymbol{u}_{\mathrm{f}}}{\partial t} = \boldsymbol{v}_{\mathrm{s}} \quad \text{on} \quad \mathit{\Gamma}_{\mathrm{i}}, \qquad \boldsymbol{P}_{\mathrm{s}} \boldsymbol{N}_{\mathrm{s}} + J \boldsymbol{\sigma} \boldsymbol{F}^{-T} \boldsymbol{n}_{\mathrm{f}} = \mathbf{0} \quad \text{on} \quad \mathit{\Gamma}_{\mathrm{i}}. \tag{3.27}$$

3.3 Constitutive models

The balance equations discussed in the previous section are valid for any material. To describe the flow of blood and the motion of the vessel, the response of the particular material should be described. The response of the material is characterized by a constitutive equation.

Hyperelastic constitutive equations are useful for structural problems that contain geometrical (large displacements) and material (non–linear relationship between stress and strain) non–linearities that exhibit reversible behaviour. We will employ a hyperelastic transverse isotropic constitutive equation to capture the response of the blood vessel.

As mentioned in Section 2.1, for high flow rates the viscosity of blood approaches a constant value. It will therefore be assumed that the fluid is Newtonian. Blood is thus characterized by using the Navier–Stokes equations and prescribing the density, ρ_{f}, and the viscosity, ν_{f}.

3.3.1 Hyperelasticity

A hyperelastic material presupposes the existence of a Helmholtz free–energy function Ψ. The function is defined per unit reference volume and not per unit mass. The free–energy function of a hyperelastic material is a function of $\boldsymbol{F}$ and is referred to as the strain–energy function. The total internal potential energy, $\Pi_{\mathrm{int}}(t)$, can be expressed in terms of the strain–energy function as $\Pi_{\mathrm{int}}(t) = \int_{\Omega_0} \Psi \mathrm{dV}$.

A hyperelastic material can be defined as a subclass of elastic materials, where the stress response can be written as:

$$\boldsymbol{P} = \frac{\partial \Psi(\boldsymbol{F})}{\partial \boldsymbol{F}} \quad \text{or} \quad \boldsymbol{\sigma} = J^{-1} \frac{\partial \Psi(\boldsymbol{F})}{\partial \boldsymbol{F}} \boldsymbol{F}^T = \boldsymbol{\sigma}^T. \tag{3.28}$$

Hyperelasticity has a conservative structure, which can be deduced from the fact that the stress response is derived from a scalar–valued potential function.

The amount of energy stored in a object remains unchanged when the object is subjected to a rigid body motion, thus Ψ must obey the restriction

$$\Psi(\boldsymbol{F}) = \Psi(\boldsymbol{Q}\boldsymbol{F}).$$

for all tensors $\boldsymbol{F}$, with $\det \boldsymbol{F} > 0$, and for all orthogonal tensors $\boldsymbol{Q}$. In order to obtain this equivalent formulations, $\boldsymbol{Q}$ is set to the transpose of the orthogonal rotation tensor $\boldsymbol{R}^T$. Using (3.16),

$$\Psi(\boldsymbol{F}) = \Psi(\boldsymbol{R}^T\boldsymbol{F}) = \Psi(\boldsymbol{R}^T\boldsymbol{R}\boldsymbol{U}) = \Psi(\boldsymbol{U}). \tag{3.29}$$

It is clear that Ψ is independent of the rotational part of $\boldsymbol{F}$ and depends on $\boldsymbol{F}$ via $\boldsymbol{U}$. The relation $\Psi(\boldsymbol{F}) = \Psi(\boldsymbol{U})$ is a necessary and sufficient condition for the strain energy to be objective during superimposed rigid body motions. Bearing this in mind and also (3.17) , an equivalent form of the strain–energy function is given by

$$\Psi(\boldsymbol{F}) = \Psi(\boldsymbol{C}). \tag{3.30}$$

Alternative expressions for the first and second Piola–Kirchhoff stresses may then be obtained as

$$\boldsymbol{P} = 2\boldsymbol{F}\frac{\partial\Psi(\boldsymbol{C})}{\partial\boldsymbol{C}} \quad \text{and} \quad \boldsymbol{S} = 2\frac{\partial\Psi(\boldsymbol{C})}{\partial\boldsymbol{C}}. \tag{3.31}$$

If the strain–energy function is invariant under a rotation of any orthogonal tensor $\boldsymbol{Q}$, such that $\Psi(*) = \Psi(\boldsymbol{Q} * \boldsymbol{Q}^T)$, it may be expressed in terms of the principal invariants of its argument. For an isotropic material $\Psi(\boldsymbol{C}) = \Psi(\boldsymbol{Q}\boldsymbol{C}\boldsymbol{Q}^T)$ holds, and the strain energy $\Psi(\boldsymbol{C})$ may be expressed through $I_a = I_a(\boldsymbol{C})$, $a = 1, 2, 3$. The second Piola–Kirchhoff stress tensor can be written by employing the chain rule of differentiation as:

$$\boldsymbol{S} = 2\frac{\partial\Psi(\boldsymbol{C})}{\partial\boldsymbol{C}} = 2\frac{\partial\Psi(I_1, I_2, I_3)}{\partial\boldsymbol{C}} = 2\left[\frac{\partial\Psi}{\partial I_1}\frac{\partial I_1}{\partial\boldsymbol{C}} + \frac{\partial\Psi}{\partial I_2}\frac{\partial I_2}{\partial\boldsymbol{C}} + \frac{\partial\Psi}{\partial I_3}\frac{\partial I_3}{\partial\boldsymbol{C}}\right], \tag{3.32}$$

where

$$\begin{aligned}
\frac{\partial I_1}{\partial\boldsymbol{C}} &= \frac{\partial \mathrm{tr}\boldsymbol{C}}{\partial\boldsymbol{C}} = \boldsymbol{I}, \\
\frac{\partial I_2}{\partial\boldsymbol{C}} &= \frac{1}{2}\left(2(\mathrm{tr}\boldsymbol{C})\boldsymbol{I} - \frac{\partial \mathrm{tr}(\boldsymbol{C}^2)}{\partial\boldsymbol{C}}\right) = I_1\boldsymbol{I} - \boldsymbol{C}, \\
\frac{\partial I_3}{\partial\boldsymbol{C}} &= I_3\boldsymbol{C}^{-1}.
\end{aligned} \tag{3.33}$$

Fibre–reinforced hyperelastic material

The vessel wall consists of an isotropic ground matrix and helical fibres (see Section 2.2). The softer ground matrix allows deformation until the fibres reaches their straightened lengths. As the fibres unravel they become stiffer and thereby prevent further deformation.

We employ a model widely used in the literature for blood vessels, developed by Holzapfel et al [51] and extended in [41] to include dispersion of the fibres. This model represents the vessel composed of a matrix material and two families of fibres.

The stress at a material point depends not only on the deformation gradient $\boldsymbol{F}$, but also on the preferred directions of the two families of fibres. Unit vectors $\boldsymbol{a}_{0,i}(\boldsymbol{X}), |\boldsymbol{a}_{0,i}| = 1,\ \ i = 1, 2$ define the direction of the fibres at point $\boldsymbol{X} \in \Omega_0$. In the deformed configuration Ω, the fibre directions at the associated point $\boldsymbol{x} \in \Omega$ are defined by $\boldsymbol{a}_i(\boldsymbol{x}), |\boldsymbol{a}_i| = 1$. The fibre directions in the material and current configurations are related by:

$$\lambda_i \boldsymbol{a}_i(\boldsymbol{x}, t) = \boldsymbol{F}(\boldsymbol{X}, t)\boldsymbol{a}_{0,i}(\boldsymbol{X}), \tag{3.34}$$

where λ is the stretch of the fibre. As $|\boldsymbol{a}_i| = 1$, the stretch can be related to $\boldsymbol{C}$ by

$$\lambda_i^2 = \boldsymbol{a}_{0,i} \cdot \boldsymbol{F}\boldsymbol{F}^T \boldsymbol{a}_{0,i} = \boldsymbol{a}_{0,i} \cdot \boldsymbol{C}\boldsymbol{a}_{0,i} = \boldsymbol{C} : \boldsymbol{A}_i, \tag{3.35}$$

where $\boldsymbol{A}_i = \boldsymbol{a}_{0,i} \otimes \boldsymbol{a}_{0,i}$ is the structural tensors. We require that the free–energy function depends on $\boldsymbol{C}$ and $\boldsymbol{A}_i$ such that $\Psi = \Psi(\boldsymbol{C}, \boldsymbol{A}_1, \boldsymbol{A}_2)$. Ψ is an isotropic tensor function of the three tensor variables $\boldsymbol{C}$, $\boldsymbol{A}_1$ and $\boldsymbol{A}_2$ if it meets the requirement

$$\Psi(\boldsymbol{C}, \boldsymbol{A}_1, \boldsymbol{A}_2) = \Psi\left(\boldsymbol{Q}\boldsymbol{C}\boldsymbol{Q}^T, \boldsymbol{Q}\boldsymbol{A}_1\boldsymbol{Q}^T, \boldsymbol{Q}\boldsymbol{A}_2\boldsymbol{Q}^T\right). \tag{3.36}$$

This requirement is satisfied if Ψ is a function of the set of invariants

$$
\begin{aligned}
&I_1(\boldsymbol{C}), \quad I_2(\boldsymbol{C}), \quad I_3(\boldsymbol{C}),\\
&I_4(\boldsymbol{C}, \boldsymbol{A_1}) = \boldsymbol{C} : \boldsymbol{A_1}, \quad I_5(\boldsymbol{C}, \boldsymbol{A_1}) = \boldsymbol{C}^2 : \boldsymbol{A_1},\\
&I_6(\boldsymbol{C}, \boldsymbol{A_2}) = \boldsymbol{C} : \boldsymbol{A_2}, \quad I_7(\boldsymbol{C}, \boldsymbol{A_2}) = \boldsymbol{C}^2 : \boldsymbol{A_2},\\
&I_8(\boldsymbol{C}, \boldsymbol{A_1}, \boldsymbol{A_2}) = (\boldsymbol{a}_{0,1} \cdot \boldsymbol{a}_{0,2})\boldsymbol{a}_{0,1} \cdot \boldsymbol{C}\boldsymbol{a}_{0,2}, \quad I_9(\boldsymbol{A_1}, \boldsymbol{A_2}) = (\boldsymbol{a}_{0,1} \cdot \boldsymbol{a}_{0,2})^2.
\end{aligned} \tag{3.37}
$$

The free–energy can be split additively into an isotropic part associated with the ground matrix and a part associated with the anisotropic deformations,

$$
\Psi_{\text{iso}} = \Psi_{\text{g}}(I_1, I_2, I_3) + \Psi_{\text{fib}}(I_4, I_5, I_6, I_7, I_8, I_9). \tag{3.38}
$$

Note that I_9 is a constant and that for an incompressible material $I_3 = 1$ and both can be left out. The way that we will deal with the incompressibility is discussed in Section (3.4.2). The model in [51] uses a reduced form in order to minimize the number of material parameters, and Ψ is given by

$$
\Psi(\boldsymbol{C}, \boldsymbol{A}_1, \boldsymbol{A}_2) = \Psi_{\text{g}}(I_1) + \Psi_{\text{fib}}(I_4, I_6). \tag{3.39}
$$

The non–collagenous groundmatrix is modelled with an incompressible isotropic Neo–Hookean model as $\Psi_{\text{g}} = \boldsymbol{c}(I_1 - 3)$. The transversely isotropic free–energy function is given by

$$
\Psi_{\text{fib}} = \frac{k_1}{2k_2} \sum_{i=4,6} \left(\exp\left(k_2 \left(\kappa I_1 + (1 - 3\kappa) I_i - 1 \right)^2 \right) - 1 \right), \tag{3.40}
$$

where k_1 is a stress–like parameter, k_2 is a non–dimensional number and κ is a parameter associated with the dispersion of the fibres. The dispersion is a measure of the degree of anisotropy or in other words the diversity of the collagen arrangement ($\kappa = 0$ implies no dispersion and $\kappa = 1/3$ implies an isotropic distribution).

3.4 The weak form of the equations

A key step in the construction of the finite element formulation, is the derivation of the weak form of the governing equations. As the system of equations will be solved monolithically, all the equations are written in the reference domain.

As biological tissue is incompressible, the usual one field variational principle is insufficient to prevent locking when lower–order finite elements are used. We introduce a two–field formulation for the hyperelastic material to circumvent volumetric locking. Both the Piola–Kirchoff stress tensors that follow from this incompressible formulation of the blood vessels are also shown in this section.

We use standard notation for Lebesgue and Sobolev spaces. We define $L_0^2(\boldsymbol{X}) = \left\{\boldsymbol{u} \in [L^2(\boldsymbol{X})]^n : \boldsymbol{u} = 0 \text{ on } \mathit{\Gamma}_D\right\}$ to be the space of square-integrable functions which satisfy the homogeneous Dirichlet boundary conditions. We also need $H_0^1(X) = \left\{\boldsymbol{u} \in [L^2(\boldsymbol{X})]^n \text{ and } \frac{\partial \boldsymbol{u}_\mathrm{i}}{\partial \boldsymbol{X}_\mathrm{j}} \in [L^2(\boldsymbol{X})] : \boldsymbol{u} = \boldsymbol{0} \text{ on } \mathit{\Gamma}_D\right\}$ namely the space of functions which together with their first derivatives are square-integrable, and which satisfy the homogeneous Dirichlet boundary conditions. Note that the weak formulations given by 3.41,3.58, 3.59 and 3.60 does not take account of the boundary conditions, which will be discussed in detail in Chapter 4.

3.4.1 Weak form of Navier–Stokes equations in reference configuration

Multiplication by a test function, integration over the domain, integration by parts and a pull back of equations (3.22) to the reference configuration gives

$$\begin{aligned}
\int_{\Omega_\mathrm{f}} \left(\boldsymbol{\phi}^{\boldsymbol{v}} \cdot J\rho_\mathrm{f} \frac{\partial \boldsymbol{v}}{\partial t}\right) \mathrm{dV} + \int_{\Omega_\mathrm{f}} \left(\boldsymbol{\phi}^{\boldsymbol{v}} \cdot J\rho_\mathrm{f} \,\mathrm{Grad}\, \boldsymbol{v}\boldsymbol{F}^{-1} \left(\boldsymbol{v} - \frac{\partial \boldsymbol{u}}{\partial \mathrm{t}}\right)\right) \mathrm{dV} & \\
+ \int_{\Omega_\mathrm{f}} \left(\nabla \boldsymbol{\phi}^{\boldsymbol{v}} : J\boldsymbol{\sigma}_\mathrm{f} \boldsymbol{F}^{-T}\right) \mathrm{dV} - \int_{\Gamma_\mathrm{f}} (\boldsymbol{\phi}^{\boldsymbol{v}} \cdot \boldsymbol{g})\, \mathrm{dS} = 0 & \qquad \forall \boldsymbol{\phi}^{\boldsymbol{v}} \in H_0^1, \\
\int_{\Omega_\mathrm{f}} \left(\phi^p \cdot \mathrm{Div}\left(J\boldsymbol{F}^{-1}\boldsymbol{v}\right)\right) \mathrm{dV} = 0 & \qquad \forall \phi^p \in L_0^2.
\end{aligned} \tag{3.41}$$

and the pull back of the stress tensor to the reference configuration is given by

$$\boldsymbol{\sigma}_\mathrm{f} = -p_\mathrm{f}\boldsymbol{I} + \rho_\mathrm{f}\nu_\mathrm{f} \left(\mathrm{Grad}\, \boldsymbol{v}\boldsymbol{F}^{-1} + \boldsymbol{F}^{-\mathrm{T}} \left(\mathrm{Grad}\, \boldsymbol{v}\right)^\mathrm{T}\right). \tag{3.42}$$

3.4.2 Precursors and weak form of fibre–reinforced solid equations

Incompressible materials

Materials that exhibits isochoric behaviour only, i.e. the volume remains constant throughout all motions, are called incompressible. Incompressible materials are characterized by the incompressibility constraint:

$$J = 1 \text{ or } \operatorname{div} \boldsymbol{v} = 0. \tag{3.43}$$

When using a standard Galerkin method (i.e. displacement–based method) and lower–order finite elements with problems that are associated with constraint conditions, significant numerical difficulties must be expected. These numerical difficulties are known as locking phenomena. They are associated with a significant loss of accuracy due to the over–stiffening of the system. Standard methods exhibits ill–conditioning of the stiffness matrix. One way to eliminate these difficulties is to use mixed finite element methods. A mixed method incorporates an additional field such as pressure that is treated as an independent variable.

The Lagrange–multiplier method is suitable to prevent volumetric locking in nearly incompressible and incompressible hyperelastic materials. A Lagrange–multiplier is used to enforce the incompressibility constraint (3.43). For this method it is standard to employ the decoupled representation of the strain–energy function:

$$\Psi(\boldsymbol{C}) = \Psi_{\text{vol}}(J) + \Psi_{\text{iso}}(\bar{\boldsymbol{C}}). \tag{3.44}$$

The isochoric part of of the strain–energy function Ψ_{iso} is a function of the modified right Cauchy–Green tensor $\bar{\boldsymbol{C}}(\boldsymbol{u}) = J^{-2/3}\boldsymbol{C}$. The internal potential energy functional is also formulated in the decoupled representation:

$$\Pi_{\text{int}}(\boldsymbol{u}, p) = \int_{\Omega_0} \left[p\left(J\left(\boldsymbol{u}\right) - 1\right) + \Psi_{\text{iso}}(\bar{\boldsymbol{C}}(\boldsymbol{u}))\right] \text{dV}. \tag{3.45}$$

The term p is the Lagrange–multiplier.

To derive a two–field variational principle, the next step is to find the stationary point of the functional $\mathit{\Pi}_{\text{int}}(\boldsymbol{u}, p)$. In order to find the stationary point the directional derivatives of $\mathit{\Pi}_{\text{int}}(\boldsymbol{u}, p)$ with respect to both the displacement field $\boldsymbol{u}$ and pressure field p need to be found and set to zero.

The directional derivative, or Gâteaux derivative of a function $\mathit{\Upsilon}(\boldsymbol{x})$ in the direction of $\boldsymbol{u}$ is defined by

$$D_{\boldsymbol{u}}\mathit{\Upsilon}(\boldsymbol{x}) = \frac{d}{d\varepsilon}\mathit{\Upsilon}(\boldsymbol{x} + \varepsilon\boldsymbol{u})|_{\varepsilon=0}. \tag{3.46}$$

The stationary conditions are given by

$$D_{\delta\mathbf{u}}\mathit{\Pi}(\mathbf{u}, p) = \int_{\mathit{\Omega}_0} \left(Jp\boldsymbol{F}^{-T} : \text{Grad}\,\delta\mathbf{u} + \boldsymbol{P} : \text{Grad}\,\delta\mathbf{u}\right) \text{dV} = \mathit{0}, \tag{3.47}$$

$$D_{\delta p}\mathit{\Pi}(\mathbf{u}, p) = \int_{\mathit{\Omega}_0} (J(\mathbf{u}) - \mathbf{1})\delta p \text{dV} = 0, \tag{3.48}$$

where δp and $\delta\boldsymbol{u}$ are the virtual pressure fields and virtual displacement fields respectively.

Constitutive model for the incompressible fibre–reinforced material

Next, $\boldsymbol{P}$ will be derived for for the incompressible fibre–reinforced material. The isochoric part of $\mathit{\Psi}(\boldsymbol{C})$ (from (3.44)) can be split into a part associated with the ground matrix and a part associated with the anisotropic deformation (3.39) :

$$\begin{aligned}\mathit{\Psi}_{\text{iso}} =& \mathit{\Psi}_{\text{g}} + \mathit{\Psi}_{\text{fib}} \\ =& \frac{\mu}{2}(\bar{I}_1 - 3) + \frac{k_1}{2k_2}\sum_{i=4,6}\left(\exp\left\{k_2\left[\kappa\bar{I}_1 + (1-3\kappa)\bar{I}_i - 1\right]^2\right\} - 1\right).\end{aligned} \tag{3.49}$$

The invariants for the isochoric part can be calculated as

$$\begin{aligned} & \bar{I}_1 = \bar{\boldsymbol{C}} : \boldsymbol{I} = J^{-\frac{2}{3}}\boldsymbol{C} : \boldsymbol{I} = J^{-\frac{2}{3}}I_1, \\ & \bar{I}_4 = \bar{\boldsymbol{C}} : \boldsymbol{A}_1 = J^{-\frac{2}{3}}\boldsymbol{C} : \boldsymbol{A}_1 = J^{-\frac{2}{3}}I_4, \\ \text{and} \quad & \bar{I}_6 = \bar{\boldsymbol{C}} : \boldsymbol{A}_1 = J^{-\frac{2}{3}}\boldsymbol{C} : \boldsymbol{A}_2 = J^{-\frac{2}{3}}I_6. \end{aligned} \tag{3.50}$$

As Ψ is a function of $\bar{\boldsymbol{C}}$, $\boldsymbol{S}$ needs to be calculated before $\boldsymbol{P} = \boldsymbol{F}\boldsymbol{S}$ can be found. Using (3.31) $\boldsymbol{S}$ is written in the decoupled representation as

$$\boldsymbol{S} = \boldsymbol{S}_{\mathrm{g}} + \boldsymbol{S}_{\mathrm{fib}} = 2\left(\frac{\partial \Psi_{\mathrm{g}}(\bar{\boldsymbol{C}})}{\partial \boldsymbol{C}} + \frac{\partial \Psi_{\mathrm{fib}}(\bar{\boldsymbol{C}})}{\partial \boldsymbol{C}}\right). \tag{3.51}$$

The isotropic hyperelastic response is

$$\begin{aligned}\boldsymbol{S}_{\mathrm{g}} &= 2\frac{\partial \Psi_{\mathrm{g}}(\bar{\boldsymbol{C}})}{\partial \boldsymbol{C}} = 2\frac{\partial \Psi_{\mathrm{g}}(\bar{\boldsymbol{C}})}{\partial \bar{\boldsymbol{C}}}\frac{(\partial \bar{\boldsymbol{C}})}{\partial \boldsymbol{C}} \\ &= \mu J^{-\frac{2}{3}}\boldsymbol{I} - \left(\frac{\mu J^{-\frac{2}{3}} I_1}{3}\right)\boldsymbol{C}^{-1}, \end{aligned}\tag{3.52}$$

$$\boldsymbol{P}_{\mathrm{g}} = \boldsymbol{F}\boldsymbol{S}_{\mathrm{g}} = \mu J^{-\frac{2}{3}}\boldsymbol{F} - \left(\frac{\mu J^{-\frac{2}{3}} I_1}{3}\right)\boldsymbol{F}^{-T}. \tag{3.53}$$

To declutter the equations to follow, the scalars $G_i = \kappa J^{-\frac{2}{3}} I_1 + (1-3\kappa)\, J^{-\frac{2}{3}} I_i - 1$ with $i = 4, 6$, are introduced. Employing G_i and (3.50) the free energy associated with the fibres becomes

$$\Psi_{\mathrm{fib}}(\bar{\boldsymbol{C}}) = \Psi_{\mathrm{fib,4}}(\boldsymbol{C}) + \Psi_{\mathrm{fib,6}}(\boldsymbol{C}), \quad \Psi_{\mathrm{fib,i}}(\boldsymbol{C}) = \frac{k_1}{2k_2}\left(\exp\left(k_2 G_i^2\right) - 1\right). \tag{3.54}$$

The partial derivative of G_i with respect to $\boldsymbol{C}$ is

$$\begin{aligned}\frac{\partial G_i}{\partial \boldsymbol{C}} &= \kappa\left(\frac{\partial J^{-\frac{2}{3}}}{\partial \boldsymbol{C}} I_1 + J^{-\frac{2}{3}}\frac{\partial I_1}{\partial \boldsymbol{C}}\right) + (1-3\kappa)\left(\frac{\partial J^{-\frac{2}{3}}}{\partial \boldsymbol{C}} I_i + J^{-\frac{2}{3}}\frac{\partial I_i}{\partial \boldsymbol{C}}\right) \\ &= (\kappa I_1 + (1-3\kappa)\, I_i)\left(-\frac{1}{3}J^{-\frac{2}{3}}\boldsymbol{C}^{-1}\right) + \left(\kappa J^{-\frac{2}{3}}\right)\boldsymbol{I} + (1-3\kappa)\, J^{-\frac{2}{3}}\boldsymbol{A}_i. \end{aligned}\tag{3.55}$$

Using (3.55) the stress response associated with the fibres can be found as

$$\boldsymbol{S}_{\mathrm{fib,i}} = 2\frac{\partial \Psi_{\mathrm{fib,i}}}{\partial \boldsymbol{C}} = \frac{k_1}{k_2}\left[(2k_2 G_i)\exp\left\{k_2 G_i^2\right\}\frac{\partial G_i}{\partial \boldsymbol{C}}\right], \tag{3.56}$$

$$\begin{aligned}\boldsymbol{P}_{\mathrm{fib,i}} = \boldsymbol{F}\boldsymbol{S}_{\mathrm{fib,i}} = 2k_1 G_i \exp\left\{k_2 G_i^2\right\}\Big[&(\kappa I_1 + (1-3\kappa)\, I_i)\left(-\frac{1}{3}J^{-\frac{2}{3}}\boldsymbol{F}^{-T}\right) \\ &+ \left(\kappa J^{-\frac{2}{3}}\right)\boldsymbol{F} + (1-3\kappa)\, J^{-\frac{2}{3}}\boldsymbol{F}\boldsymbol{A}_i\Big]. \end{aligned}\tag{3.57}$$

Weak form of solid equations

Taking the incompressibility into account the weak form of the solid equations can be written in the reference domain as

$$\int_{\Omega_{\mathrm{s}}} \left(\boldsymbol{\phi}^{\boldsymbol{v}} \cdot \rho_{\mathrm{s}} \frac{\partial \boldsymbol{v}}{\partial t} \right) \mathrm{dV} + \int_{\Omega_{\mathrm{s}}} \left(\nabla \boldsymbol{\phi}^{\boldsymbol{v}} : Jp\boldsymbol{F}^{-\mathrm{T}} \right) \mathrm{dV}$$

$$+ \int_{\Omega_{\mathrm{s}}} \left(\nabla \boldsymbol{\phi}^{\boldsymbol{v}} : \boldsymbol{P} \right) \mathrm{dV} - \int_{\Gamma_{\mathrm{s}}} \left(\boldsymbol{\phi}^{\boldsymbol{v}} \cdot \boldsymbol{g} \right) \mathrm{dS} = 0 \qquad \forall \boldsymbol{\phi}^{\boldsymbol{v}} \in H_0^1, \tag{3.58}$$

$$\int_{\Omega_{\mathrm{s}}} \left(\boldsymbol{\phi}^{\boldsymbol{u}} \cdot \frac{\partial \boldsymbol{u}}{\partial t} \right) \mathrm{dV} - \int_{\Omega_{\mathrm{s}}} \left(\boldsymbol{\phi}^{\boldsymbol{u}} \cdot \boldsymbol{v} \right) \mathrm{dV} = 0 \qquad \forall \boldsymbol{\phi}^{\boldsymbol{u}} \in H_0^1, \tag{3.59}$$

$$\int_{\Omega_{\mathrm{s}}} \phi^p \left(J - 1 \right) \mathrm{dV} = 0 \qquad \forall \phi^p \in L_0^2. \tag{3.60}$$

3.4.3 Mesh motion

The mesh motion is an abstract variable. On the interface the Dirichlet boundary conditions for the mesh motion are given by (3.25_b-3.25_c). It would be undesirable if the mesh offers any resistance to the vessel. To prevent this a Dirichlet condition is implemented on the interface ($\boldsymbol{u}_f = \boldsymbol{u}_s$) by requiring that $\nabla \boldsymbol{\phi}^{\boldsymbol{u}}$ vanish on the interface. To emphasize this, the Hilbert space $\mathcal{V}_{\Gamma_i}^0 = H_{0,\mathrm{i}}^1(\boldsymbol{X}) = \{\boldsymbol{u} \in H^1(\boldsymbol{X}) : \boldsymbol{u} = \boldsymbol{0} \text{ on } \Gamma_{\mathrm{i}}\}$ is used. The weak form of the mesh motion is then

$$\int_{\Omega_{\mathrm{f}}} \left(\nabla \boldsymbol{\phi}^{\boldsymbol{u}} : \alpha \, \mathrm{Grad} \, \boldsymbol{u} \right) \mathrm{dV} - \int_{\Gamma_{\mathrm{f}}} \left(\boldsymbol{\phi}^{\boldsymbol{v}} \cdot \boldsymbol{g} \right) \mathrm{dS} = 0 \qquad \forall \boldsymbol{\phi}^{\boldsymbol{v}} \in \mathcal{V}_{\Gamma_{\mathrm{i}}}^0. \tag{3.61}$$

3.4.4 Coupling conditions

The coupling conditions are enforced in the following manner. Continuity of $\boldsymbol{v}$ across Γ_{i} is strongly enforced by using a continuous velocity field across the whole domain Ω. The continuity of normal stresses becomes an implicit condition by omitting the boundary integral jump,

$$\int_{\Gamma_{\mathrm{i}}} (\boldsymbol{\phi}^v \cdot J\boldsymbol{\sigma}_s \boldsymbol{F}^{-T} \boldsymbol{N}_s) \mathrm{dV} = \int_{\Gamma_{\mathrm{i}}} (\boldsymbol{\phi}^v \cdot J\boldsymbol{\sigma}_f \boldsymbol{F}^{-T} \boldsymbol{N}_f) \mathrm{dV}.$$

3.5 Discretization and Stabilization

To find the numerical solution for the continuous fields $\boldsymbol{u}, \boldsymbol{v}, p$ the equations discussed in the previous section need to be discretized in both time and space. We use Rothe's method and discretize first in time, and solve the resulting stationary PDE with finite element techniques. In the following sections the time discretization and then the spatial finite element discretization for the weak form of the equations will be discussed. The residual of the equations developed in the previous section are written in the reference domain as follows:

$$
\begin{aligned}
R(\boldsymbol{U})(\boldsymbol{\phi}^{\boldsymbol{v}}, \boldsymbol{\phi}^{\boldsymbol{u}}, \phi^{p}) = & \int_{\Omega_\mathrm{f}} \boldsymbol{\phi}^{\boldsymbol{v}} \cdot J\rho_\mathrm{f} \frac{\partial \boldsymbol{v}}{\partial t}\,\mathrm{dV} + \int_{\Omega_\mathrm{f}} \boldsymbol{\phi}^{\boldsymbol{v}} \cdot J\rho_\mathrm{f}\ (\mathrm{Grad}\,\boldsymbol{v})\,\boldsymbol{F}^{-1}(\boldsymbol{v} - \frac{\partial \boldsymbol{u}}{\partial \mathrm{t}})\,\mathrm{dV} \\
& + \int_{\Omega_\mathrm{f}} \nabla\boldsymbol{\phi}^{\boldsymbol{v}} : J\boldsymbol{\sigma}_\mathrm{f}\boldsymbol{F}^{-T}\mathrm{dV} - \int_{\Gamma_\mathrm{f}} \boldsymbol{\phi}^{\boldsymbol{v}} \cdot \boldsymbol{g}\,\mathrm{dS} \\
& + \int_{\Omega_\mathrm{f}} \phi^{p} \cdot \mathrm{Div}\left(J\boldsymbol{F}^{-1}\boldsymbol{v}\right)\mathrm{dV} + \int_{\Omega_\mathrm{s}} \boldsymbol{\phi}^{\boldsymbol{v}} \cdot \rho_\mathrm{s}\frac{\partial \boldsymbol{v}}{\partial \mathrm{t}}\mathrm{dV} \\
& + \int_{\Omega_\mathrm{s}} \left(\nabla\boldsymbol{\phi}^{\boldsymbol{v}} : Jp\boldsymbol{F}^{-T}\right)\mathrm{dV} + \int_{\Omega_\mathrm{s}} \nabla\boldsymbol{\phi}^{\boldsymbol{v}} : \boldsymbol{P}\,\mathrm{dV} + \int_{\Omega_\mathrm{s}} \boldsymbol{\phi}^{\boldsymbol{u}} \cdot \frac{\partial \boldsymbol{u}}{\partial \mathrm{t}}\mathrm{dV} \\
& - \int_{\Omega_\mathrm{s}} \boldsymbol{\phi}^{\boldsymbol{u}} \cdot \boldsymbol{v}\,\mathrm{dV} + \int_{\Omega_\mathrm{s}} \phi^{\mathrm{p}}\,(\mathrm{J}-1)\,\mathrm{dV} + \int_{\Omega_\mathrm{f}} \nabla\boldsymbol{\phi}^{\boldsymbol{u}} : (\alpha\,\mathrm{Grad}\boldsymbol{u})\,\mathrm{dV} \\
& = 0 \qquad \forall\boldsymbol{\phi} \in \mathcal{X}^0,
\end{aligned}
\tag{3.62}
$$

where $\boldsymbol{U} = \{\boldsymbol{v}, \boldsymbol{u}, p\}$ and $\mathcal{X}^0 = H^1_{0,\mathrm{f},\boldsymbol{v}} \times H^1_{0,\Gamma_\mathrm{i},\mathrm{f},\boldsymbol{u}} \times L^2_{0,\mathrm{f},p}$.

3.5.1 Stabilization of convected-dominated flows

To prevent spatial instability that may result for convected dominated flows, streamline upwinding by the Petrov-Galerkin method (SUPG) is implemented [19]. To eliminate possible oscillations in the solution an artificial viscosity is added in the direction of the streamlines:

$$\tilde{R}(\boldsymbol{U})(\boldsymbol{\phi}^{\boldsymbol{v}}, \boldsymbol{\phi}^{\boldsymbol{u}}, \phi^p) = R(\boldsymbol{U})(\boldsymbol{\phi}^{\boldsymbol{v}}, \boldsymbol{\phi}^{\boldsymbol{u}}, \phi^p) + S_{stab}(\boldsymbol{U})(\boldsymbol{\phi}^{\boldsymbol{v}}), \tag{3.63}$$

$$S_{stab} = \sum_{K=1}^{n_{el}} \Big[(J\rho_{\mathrm{f}} \frac{\partial \boldsymbol{v}}{\partial t} + J\rho_f \ (\mathrm{Grad}\, \boldsymbol{v})\, \boldsymbol{F}^{-1}(\boldsymbol{v} - \frac{\partial \boldsymbol{u}}{\partial t}) + J\boldsymbol{\sigma}_{\mathrm{f}}\boldsymbol{F}^{-T}) \cdot \delta_K(\boldsymbol{v} \cdot \nabla)\boldsymbol{\phi}^{\boldsymbol{v}} \Big], \tag{3.64}$$

$$\delta_K = 0.1 \frac{h_K^2}{6\nu + h_K \parallel \boldsymbol{v} \parallel_K} \tag{3.65}$$

with h_K the length of the element. More information on the choice of these parameters is given in [18]. This consistent formulation has a major drawback that comes from the necessity to computing second derivatives that results from linearization of $J\boldsymbol{\sigma}_{\mathrm{f}}\boldsymbol{F}^{-T}$. For this reason we follow [100] and use a nonconsistent simplified version and apply the stabilization only to the convective term, thus

$$S_{stab} = \sum_{K=1}^{n_{el}} \Big[J\rho_f \ (\mathrm{Grad}\, \boldsymbol{v})\, \boldsymbol{F}^{-1}\boldsymbol{v} \cdot \delta_K(\boldsymbol{v} \cdot \nabla)\boldsymbol{\phi}^{\boldsymbol{v}} \Big]. \tag{3.66}$$

3.5.2 Temporal discretization

Newmark's method is the most general method for temporal discretization. It is unconditionally stable in linear systems, but there is no general stability result for non–linear systems. The Generalized–α method allows damping while maintaining second–order accuracy. Therefore time discretization is done by using the Generalized–α method [23] as implemented for FSI in [60].

The Generalized–α method evaluates the time derivatives of the unknowns at the generalized midpoint α_{m} and the unknowns themselves at the generalized midpoint α_{f}. To illustrate this the evaluation of the acceleration and the convective term are shown:

$$\left(\frac{\partial \boldsymbol{v}}{\partial t}\right)^{n+1-\alpha_\mathrm{m}} =(1-\alpha_\mathrm{m})\left(\frac{\partial \boldsymbol{v}}{\partial t}\right)^{n+1} + \alpha_\mathrm{m}\left(\frac{\partial \boldsymbol{v}}{\partial t}\right)^{n}, \tag{3.67}$$

$$\begin{aligned}\left(J\rho_f\ (\mathrm{Grad}\,\boldsymbol{v})\,\boldsymbol{F}^{-1}(\boldsymbol{v}-\frac{\partial \boldsymbol{u}}{\partial t})\right)^{n+1-\alpha_\mathrm{f}} =&(1-\alpha_\mathrm{f})\left(J\rho_f\ (\mathrm{Grad}\,\boldsymbol{v})\,\boldsymbol{F}^{-1}(\boldsymbol{v}-\frac{\partial \boldsymbol{u}}{\partial t})\right)^{n+1}\\ &+\alpha_\mathrm{f}\left(J\rho_f\ (\mathrm{Grad}\,\boldsymbol{v})\,\boldsymbol{F}^{-1}(\boldsymbol{v}-\frac{\partial \boldsymbol{u}}{\partial t})\right)^{n}.\end{aligned} \tag{3.68}$$

Newmark approximations are used to evaluate the accelerations and displacements at $t = t_{n+1}$ as follows:

$$\left(\frac{\partial \boldsymbol{v}}{\partial t}\right)^{n+1} = \frac{1}{\gamma\triangle t}(\boldsymbol{v}^{n+1}+\boldsymbol{v}^{n}) - \frac{1-\gamma}{\gamma}\left(\frac{\partial \boldsymbol{v}}{\partial t}\right)^{n}, \tag{3.69}$$

$$\boldsymbol{u}^{n+1} = \boldsymbol{u}^{n} + \frac{\triangle t}{\gamma}\left[\beta\boldsymbol{v}^{n+1}+(\gamma-\beta)\boldsymbol{v}^{n}\right] + \frac{\triangle t^2}{2\gamma}(\gamma-2\beta)\left(\frac{\partial \boldsymbol{v}}{\partial t}\right)^{n}. \tag{3.70}$$

The choice of the parameters for the fluid equations was optimized in [56] to the following:

$$\begin{aligned}\alpha_\mathrm{m} &= \frac{3\rho_\infty - 1}{2(1+\rho_\infty)},\\ \alpha_\mathrm{f} &= \frac{\rho_\infty}{1+\rho_\infty},\\ \gamma &= \frac{1}{2} - \alpha_\mathrm{m} + \alpha_\mathrm{f}.\end{aligned} \tag{3.71}$$

The choice of the parameters for the structural equations was optimized in [23] to the following:

$$\begin{aligned}\alpha_\mathrm{m} &= \frac{2\rho_\infty - 1}{1+\rho_\infty},\\ \alpha_\mathrm{f} &= \frac{\rho_\infty}{1+\rho_\infty},\\ \gamma &= \frac{1}{2} - \alpha_\mathrm{m} + \alpha_\mathrm{f},\\ \beta &= \frac{1}{4}(1-\alpha_\mathrm{m}+\alpha_\mathrm{f})^2.\end{aligned} \tag{3.72}$$

Here $\rho_\infty (0 \le \rho_\infty \le 1)$ is the spectral radius for an infinite time step. For $\rho_\infty = 1$ no damping will occur and for $\rho_\infty = 0$ the maximum level of damping will occur.
The discrete form of the equations at $t = t_{n+1}$ is as follows:

$$
\begin{aligned}
\tilde{R}(\boldsymbol{U}^{n+1})(\boldsymbol{\phi}^{\boldsymbol{v}}, \boldsymbol{\phi}^{\boldsymbol{u}}, \phi^p) = & \int_{\Omega_\mathrm{f}} \boldsymbol{\phi}^{\boldsymbol{v}} \cdot \left(J^{n+\frac{1}{2}} \rho_\mathrm{f} \frac{(1-\alpha_\mathrm{m})/\gamma(\boldsymbol{v}^{n+1-\alpha_\mathrm{f}} - \boldsymbol{v}^n) + [((1-\alpha_\mathrm{m})(1-\gamma)/\gamma) - \alpha_\mathrm{m}]\,(\boldsymbol{v}^n - \boldsymbol{v}^{n-1})}{\triangle t} \right) \mathrm{dV} \\
& - \int_{\Omega_\mathrm{f}} \boldsymbol{\phi}^{\boldsymbol{v}} \cdot J\rho_\mathrm{f}\,\mathrm{Grad}\,\boldsymbol{v}\boldsymbol{F}^{-1}(\frac{\boldsymbol{u}^{\mathrm{n}+1-\alpha_\mathrm{f}} - \boldsymbol{u}^\mathrm{n}}{\triangle \mathrm{t}})\,\mathrm{dV} \\
& + \int_{\Omega_\mathrm{s}} \boldsymbol{\phi}^{\boldsymbol{v}} \cdot \left(\rho_\mathrm{s} \frac{(1-\alpha_\mathrm{m})/\gamma(\boldsymbol{v}^{n+1-\alpha_\mathrm{f}} - \boldsymbol{v}^n) + [((1-\alpha_\mathrm{m})(1-\gamma)/\gamma) - \alpha_\mathrm{m}]\,(\boldsymbol{v}^n - \boldsymbol{v}^{n-1})}{\triangle t} \right) \mathrm{dV} \\
& + \int_{\Omega_\mathrm{s}} \boldsymbol{\phi}^{\boldsymbol{u}} \cdot \left(\frac{\boldsymbol{u}^{n+1-\alpha_\mathrm{f}} - \boldsymbol{u}^n}{\triangle t} \right) \mathrm{dV} \\
& + \int_{\Omega_\mathrm{f}} \nabla \boldsymbol{\phi}^{\boldsymbol{u}} : \alpha\,\mathrm{Grad}\,\boldsymbol{u}^\mathrm{n}\,\mathrm{dV} + \int_{\Omega_\mathrm{s}} \phi^p\,(J^\mathrm{n} - 1)\,\mathrm{dV} \\
& + \int_{\Omega_\mathrm{f}} \nabla \boldsymbol{\phi}^{\boldsymbol{v}} : J^n p(\boldsymbol{F}^{-T})^n\,\mathrm{dV} - \int_{\Gamma_\mathrm{f}} \boldsymbol{\phi}^{\boldsymbol{v}} \cdot \boldsymbol{g}\,\mathrm{dS} \\
& + \int_{\Omega_\mathrm{f}} \phi^p \left(\mathrm{Div}\,\left(J^n (\boldsymbol{F}^{-1})^n \boldsymbol{v}^n \right)\right) \mathrm{dV} \\
& + (1-\alpha_\mathrm{f}) \int_{\Omega_\mathrm{f}} \boldsymbol{\phi}^{\boldsymbol{v}} \cdot J^{n+1-\alpha_\mathrm{f}} \rho_\mathrm{f}\,\mathrm{Grad}\,\boldsymbol{v}^{n+1-\alpha_\mathrm{f}} (\boldsymbol{F}^{-1})^{n+1-\alpha_\mathrm{f}} \boldsymbol{v}^{n+1-\alpha_\mathrm{f}}\,\mathrm{dV} \\
& + (\alpha_\mathrm{f}) \int_{\Omega_\mathrm{f}} \boldsymbol{\phi}^{\boldsymbol{v}} \cdot J^n \rho_\mathrm{f}\,\mathrm{Grad}\,\boldsymbol{v}^n (\boldsymbol{F}^{-1})^n \boldsymbol{v}^n\ ,\mathrm{dV} \\
& + (1-\alpha_\mathrm{f}) \int_{\Omega_\mathrm{f}} \nabla \boldsymbol{\phi}^{\boldsymbol{v}} : J^{n+1-\alpha_\mathrm{f}} \rho_\mathrm{f} \nu_\mathrm{f}\,(\mathrm{Grad}\,\boldsymbol{v}^{\mathrm{n}+1-\alpha_\mathrm{f}} (\boldsymbol{F}^{-1})^{\mathrm{n}+1-\alpha_\mathrm{f}} \\
& \qquad + (\boldsymbol{F}^{-T})^{n+1-\alpha_\mathrm{f}}\,\mathrm{Grad}\,(\boldsymbol{v}^\mathrm{T})^{\mathrm{n}+1-\alpha_\mathrm{f}})(\boldsymbol{F}^{-\mathrm{T}})^{\mathrm{n}+1-\alpha_\mathrm{f}}\,\mathrm{dV} \\
& + (\alpha_\mathrm{f}) \int_{\Omega_\mathrm{f}} \nabla \boldsymbol{\phi}^{\boldsymbol{v}} : J^n \rho_\mathrm{f} \nu_\mathrm{f} (\,\mathrm{Grad}\,\boldsymbol{v}^\mathrm{n} (\boldsymbol{F}^{-1})^\mathrm{n} + (\boldsymbol{F}^{-\mathrm{T}})^\mathrm{n}\,\mathrm{Grad}\,(\boldsymbol{v}^\mathrm{T})^\mathrm{n}) \boldsymbol{F}^{-\mathrm{T}}\,\mathrm{dV} \\
& + (1-\alpha_\mathrm{f}) \int_{\Omega_\mathrm{s}} \nabla \boldsymbol{\phi}^{\boldsymbol{v}} : \boldsymbol{P}^{n+1-\alpha_\mathrm{f}}\,\mathrm{dV} + (\alpha_\mathrm{f}) \int_{\Omega_\mathrm{s}} \nabla \boldsymbol{\phi}^{\boldsymbol{v}} : \boldsymbol{P}^\mathrm{n}\,\mathrm{dV} \\
& - \int_{\Omega_\mathrm{s}} \boldsymbol{\phi}^{\boldsymbol{u}} \cdot (1/\gamma(\beta \boldsymbol{v}^{n+1-\alpha_\mathrm{f}} + (\gamma - \beta)\boldsymbol{v}^n) - \triangle t/(2\gamma)(\gamma - 2\beta)(\boldsymbol{v}^n - \boldsymbol{v}^{n-1}))\,\mathrm{dV} \\
& = 0 \qquad\qquad\qquad\qquad\qquad\qquad\qquad\qquad \forall \boldsymbol{\phi} \in \mathcal{X}^0,
\end{aligned}
$$

where $\triangle t = t^{n+1} - t^n$ and $J^{n+\frac{1}{2}} = \frac{J^n + J^{n+1}}{2}$.

3.5.3 Spatial discretization

This section will describe the discretization in space of the time discretized equations. To find the approximate solutions to the continuous problem, finite dimensional subspaces $\mathcal{X}_h^0 \subset \mathcal{X}^0$ need to be constructed. The domain is divided into n_e cells with N nodes. At each node there are 7 degrees of freedom. The total amount of degrees of freedom is denoted as N_{dof}. A Galerkin approach is followed to find the following approximations for the continuous unknowns:

$$\boldsymbol{v} \approx \boldsymbol{v}_h = \sum_{j=1}^{N_{\text{dof}}} v_j(t)\boldsymbol{\varphi}_j(\boldsymbol{x}), \quad \boldsymbol{u} \approx \boldsymbol{u}_h = \sum_{j=1}^{N_{\text{dof}}} u_j(t)\boldsymbol{\varphi}_j(\boldsymbol{x}),$$
$$\text{and} \quad p \approx p_h = \sum_{j=1}^{N_{\text{dof}}} p_j(t)\varphi_j(\boldsymbol{x}). \tag{3.73}$$

Here $v_h(t)$, $u_h(t)$ and $p_h(t)$ are the different degrees of freedom. In deal.II the shape functions have the form:

$$\boldsymbol{\varphi}_j(\boldsymbol{x}) = \varphi_j \boldsymbol{e}_{\text{comp}(j)}. \tag{3.74}$$

The test functions are approximated by

$$\boldsymbol{\phi}^{\boldsymbol{v}} \approx \boldsymbol{\phi}_h^{\boldsymbol{v}} = \sum_{j=1}^{N_{\text{dof}}} \phi_{v_j}\boldsymbol{\varphi}_{\boldsymbol{j}}(\boldsymbol{x}), \quad \boldsymbol{\phi}^{\boldsymbol{u}} \approx \boldsymbol{\phi}_h^{\boldsymbol{u}} = \sum_{j=1}^{N_{\text{dof}}} \phi_{u_j}\boldsymbol{\varphi}_j(\boldsymbol{x}),$$
$$\text{and} \quad \phi^p \approx \phi_h^p = \sum_{j=1}^{N_{\text{dof}}} \phi_{p_j}\varphi_j(\boldsymbol{x}), \tag{3.75}$$

where $\boldsymbol{\phi}_h^{\boldsymbol{v}}$, $\boldsymbol{\phi}_h^{\boldsymbol{u}}$ and ϕ_h^p are the nodal values of the test functions. They are not functions of time.

The discretized equations to find the approximated solutions for all $n = 1, 2....N$ are given by:

$$\tilde{R}(\boldsymbol{U}_h^n)(\boldsymbol{\phi}_h^{\boldsymbol{v}}, \boldsymbol{\phi}_h^{\boldsymbol{u}}, \phi_h^p) = 0 \qquad \forall \boldsymbol{\phi}_h \in \mathcal{X}_h^0. \tag{3.76}$$

3.6 Linearization

The discretized equations contains several non-linearities. The structure contains geometrical as well as material non–linearities, the convection term in the the fluid is non–linear and the ALE map induces non–linear transformation rules.

We employ Newton's method to solve the equations for each time step. Given an initial guess $\boldsymbol{U}_h^{n,0}$, find the update $\delta\boldsymbol{U}_h^{n,j}$ for $j = 0, 1, 2, ...$:

$$A(\boldsymbol{U}_h^{n,j})(\boldsymbol{\phi}_h)\delta\boldsymbol{U}_h^{n,j} = -R(\boldsymbol{U}_h^{n,j})(\boldsymbol{\phi}_h), \qquad \forall\boldsymbol{\phi}_h \in \mathcal{X}_h^0.$$
$$\boldsymbol{U}_h^{n,j+1} = \boldsymbol{U}_h^{n,j} + \varrho\delta\boldsymbol{U}_h^{n,j}. \tag{3.77}$$

In this equation ϱ is a damping parameter used for line search iterations. We follow the strategy in [99] to determine ϱ. The tangent, $R_{D_{\Delta \boldsymbol{U}}}(\boldsymbol{U}_h^{n,j})(\boldsymbol{\phi}_h)$ are calculated using directional derivatives (3.46).

The next sections show the computations for the exact Jacobian matrix that was used to solve the equations.

3.6.1 Linearized Navier–Stokes equations

Three directional derivatives of the momentum balance equation of the fluid in the reference configuration should be calculated. Firstly the calculation of the directional derivative with respect to a incremental velocity field $\Delta\boldsymbol{v}$ is shown:

$$\begin{aligned} D_{\Delta\boldsymbol{v}}(R_\mathrm{f}, \boldsymbol{\phi}^{\boldsymbol{v}}) = &\int_{\Omega_\mathrm{f}} \boldsymbol{\phi}^{\boldsymbol{v}} \cdot J\rho_\mathrm{f}\frac{\partial\Delta\boldsymbol{v}}{\partial t}\mathrm{dV} + \int_{\Omega_\mathrm{f}} \boldsymbol{\phi}^{\boldsymbol{v}} \cdot \mathrm{J}\rho_\mathrm{f}\,\mathrm{Grad}\,(\Delta\boldsymbol{v})\boldsymbol{F}^{-1}(\boldsymbol{v} - \frac{\partial\boldsymbol{u}}{\partial \mathrm{t}})\,\mathrm{dV} \\ &+ \int_{\Omega_\mathrm{f}} \boldsymbol{\phi}^{\boldsymbol{v}} \cdot J\rho_\mathrm{f}\mathrm{Grad}\,\boldsymbol{v}\boldsymbol{F}^{-1}\Delta\boldsymbol{v}\,\mathrm{dV} \\ &+ \int_{\Omega_\mathrm{f}} \nabla\boldsymbol{\phi}^{\boldsymbol{v}} : J\rho_\mathrm{f}\nu_\mathrm{f}\,(\mathrm{Grad}\,(\Delta\boldsymbol{v})\boldsymbol{F}^{-1} + \boldsymbol{F}^{-\mathrm{T}}(\mathrm{Grad})(\Delta\boldsymbol{v}))\boldsymbol{F}^{-\mathrm{T}}\,\mathrm{dV}. \end{aligned} \tag{3.78}$$

Next the directional derivative resulting from a incremental displacement field in the mesh motion $\Delta\boldsymbol{u}$ is shown:

$$\begin{aligned} D_{\Delta\boldsymbol{u}}(R_\mathrm{f}, \boldsymbol{\phi}^{\boldsymbol{v}}) = &\int_{\Omega_\mathrm{f}} \boldsymbol{\phi}^{\boldsymbol{v}} \cdot D_{\Delta\boldsymbol{u}}(J)\rho_\mathrm{f}\Delta\boldsymbol{v}\,\mathrm{dV} - \int_{\Omega_\mathrm{f}} \boldsymbol{\phi}^{\boldsymbol{v}} \cdot D_{\Delta\boldsymbol{u}}(J)\rho_\mathrm{f}\,\mathrm{Grad}\,\boldsymbol{v}\boldsymbol{F}^{-1}\frac{\partial\boldsymbol{u}_\mathrm{f}}{\partial\mathrm{t}}\,\mathrm{dV} \\ &- \int_{\Omega_\mathrm{f}} \boldsymbol{\phi}^{\boldsymbol{v}} \cdot J\rho_\mathrm{f}\,\mathrm{Grad}\,\boldsymbol{v}D_{\Delta\boldsymbol{u}}(\boldsymbol{F}^{-1})\boldsymbol{u}_\mathrm{f}\,\mathrm{dV} \\ &- \int_{\Omega_\mathrm{f}} \boldsymbol{\phi}^{\boldsymbol{v}} \cdot J\rho_\mathrm{f}\,\mathrm{Grad}\,\boldsymbol{v}\boldsymbol{F}^{-1}\frac{\partial\Delta\boldsymbol{u}_\mathrm{f}}{\partial\mathrm{t}}\,\mathrm{dV} \\ &+ \int_{\Omega_\mathrm{f}} \nabla\boldsymbol{\phi}^{\boldsymbol{v}} : D_{\Delta\boldsymbol{u}}(J)\boldsymbol{\sigma}_\mathrm{f}\boldsymbol{F}^{-T}\,\mathrm{dV} + \int_{\Omega_\mathrm{f}} \nabla\boldsymbol{\phi}^{\boldsymbol{v}} : J\boldsymbol{\sigma}_\mathrm{f}D_{\Delta\boldsymbol{u}}(\boldsymbol{F}^{-T})\,\mathrm{dV} \\ &+ \int_{\Omega_\mathrm{f}} \nabla\boldsymbol{\phi}^{\boldsymbol{v}} : J\rho_\mathrm{f}\nu_\mathrm{f}\,(\mathrm{Grad}\,\boldsymbol{v}D_{\Delta\boldsymbol{u}}(\boldsymbol{F}^{-1}) + D_{\Delta\boldsymbol{u}}(\boldsymbol{F}^{-T})\,\mathrm{Grad}\,\boldsymbol{v}^\mathrm{T})\boldsymbol{F}^{-\mathrm{T}}\,\mathrm{dV}, \end{aligned} \tag{3.79}$$

with

$$
\begin{aligned}
D_{\Delta \boldsymbol{u}}(J) &= \frac{\partial J}{\partial \boldsymbol{F}} : \nabla(\Delta \boldsymbol{u}) \\
&= J\boldsymbol{F}^{-T} : \nabla(\Delta \boldsymbol{u}) \\
&= J\boldsymbol{I} : \boldsymbol{F}^{-1}\nabla(\Delta \boldsymbol{u}),
\end{aligned} \tag{3.80}
$$

and

$$
\begin{aligned}
D_{\Delta \boldsymbol{u}}(\boldsymbol{F}^{-1}) &= \frac{\partial(\boldsymbol{F}^{-1})}{\partial \boldsymbol{F}} : \nabla(\Delta \boldsymbol{u}) \\
&= -\boldsymbol{F}^{-1}\nabla(\Delta \boldsymbol{u})\boldsymbol{F}^{-1},
\end{aligned} \tag{3.81}
$$

and

$$
\begin{aligned}
D_{\Delta \boldsymbol{u}}(\boldsymbol{F}^{-T}) &= \frac{\partial(\boldsymbol{F}^{-T})}{\partial \boldsymbol{F}} : \nabla(\Delta \boldsymbol{u}) \\
&= -\boldsymbol{F}^{-T}\nabla(\Delta \boldsymbol{u})^T\boldsymbol{F}^{-T}.
\end{aligned} \tag{3.82}
$$

Lastly the momentum equation's directional derivative with respect to an incremental change in the pressure field Δp is shown:

$$
D_{\Delta p}(R_{\mathrm{f}}, \boldsymbol{\phi}^{\boldsymbol{v}}) = \int_{\Omega_{\mathrm{f}}} \nabla\boldsymbol{\phi}^{\boldsymbol{v}} : J\rho_{\mathrm{f}}\nu_{\mathrm{f}}\Delta p\boldsymbol{F}^{-T} \,\mathrm{dV}. \tag{3.83}
$$

Directional derivatives for the incompressibility constraint can be found with respect to the incremental changes in the velocity and displacement fields. Note that the directional derivative with respect to pressure is zero in the fluid domain. This results in zeroes on the diagonal of the Jacobian matrix on the fluid domain. The directional derivative for the incompressibility constraint with respect to Δv is given by

$$
D_{\Delta \boldsymbol{v}}(R_{\mathrm{f}}, \phi^p) = \int_{\Omega_{\mathrm{f}}} \phi^p \left(\mathrm{Div}\left(J\boldsymbol{F}^{-1}\Delta\boldsymbol{v}\right), \phi^p\right) \mathrm{dV}, \tag{3.84}
$$

and with respect to Δu by

$$
D_{\Delta \boldsymbol{u}}(R_{\mathrm{f}}, \phi^p) = \int_{\Omega_{\mathrm{f}}} \phi^p \left(\mathrm{Div}\left(\mathrm{D}_{\Delta \boldsymbol{u}}(\mathrm{J})\boldsymbol{F}^{-1}\boldsymbol{v}\right)\right) \mathrm{dV} + \int_{\Omega_{\mathrm{f}}} \phi^p \left(\mathrm{Div}\left(JD_{\Delta \boldsymbol{u}}(\boldsymbol{F}^{-1})\boldsymbol{v}\right)\right) \mathrm{dV}. \tag{3.85}
$$

3.6.2 Linearized mesh motion equations

The mesh motion equation is only a function of $\boldsymbol{u}$ and there is only one non–zero directional derivative:

$$D_{\Delta \boldsymbol{u}}(R_{\mathrm{f}}, \boldsymbol{\phi}^{\boldsymbol{u}}) = \int_{\Omega_{\mathrm{f}}} \nabla \boldsymbol{\phi}^{\boldsymbol{u}} : \alpha \nabla(\Delta \boldsymbol{u}) \, \mathrm{dV}. \tag{3.86}$$

3.6.3 Linearized structure equations

The linearized equations associated with the structure are as follows. The directional derivatives for (3.58) are

$$D_{\Delta \boldsymbol{v}}(R_{\mathrm{s}}, \boldsymbol{\phi}^{\boldsymbol{v}}) = \int_{\Omega_{\mathrm{s}}} \boldsymbol{\phi}^{\boldsymbol{v}} \cdot \rho_{\mathrm{s}} \frac{\partial \Delta \boldsymbol{v}}{\partial t} \, \mathrm{dV}, \tag{3.87}$$

$$D_{\Delta \boldsymbol{u}}(R_{\mathrm{s}}, \boldsymbol{\phi}^{\boldsymbol{v}}) = \int_{\Omega_{\mathrm{s}}} \nabla \boldsymbol{\phi}^{\boldsymbol{v}} \cdot \left(\frac{\partial \boldsymbol{P}}{\partial \boldsymbol{F}} : \nabla(\Delta \boldsymbol{u}) \right) \mathrm{dV}, \tag{3.88}$$

$$D_{\Delta p}(R_{\mathrm{s}}, \boldsymbol{\phi}^{\boldsymbol{v}}) = \int_{\Omega_{\mathrm{s}}} \nabla \boldsymbol{\phi}^{\boldsymbol{v}} \cdot \Delta p J \boldsymbol{F}^{-T} \, \mathrm{dV}. \tag{3.89}$$

The directional derivatives for (3.59) are

$$D_{\Delta \boldsymbol{v}}(R_{\mathrm{s}}, \boldsymbol{\phi}^{\boldsymbol{u}}) = -\int_{\Omega_{\mathrm{s}}} \boldsymbol{\phi}^{\boldsymbol{u}} \cdot \Delta \boldsymbol{v} \, \mathrm{dV}, \tag{3.90}$$

$$D_{\Delta \boldsymbol{u}}(R_{\mathrm{s}}, \boldsymbol{\phi}^{\boldsymbol{u}}) = \int_{\Omega_s} \boldsymbol{\phi}^{\boldsymbol{u}} \cdot \Delta \boldsymbol{u} \, \mathrm{dV}. \tag{3.91}$$

The directional derivatives for (3.60) are

$$D_{\Delta \boldsymbol{u}}(R_{\mathrm{s}}, \phi^{p}) = \int_{\Omega_s} \phi^{p} \left(D_{\Delta \boldsymbol{u}}(J) \right) \mathrm{dV}. \tag{3.92}$$

The tangent $\mathcal{A} = \frac{\partial \boldsymbol{P}}{\partial \boldsymbol{F}}$ can be split additively into an isotropic part and a part associated with anisotropic deformations,

$$\mathcal{A} = \mathcal{A}_{\mathrm{g}} + \mathcal{A}_{\mathrm{fib}}. \tag{3.93}$$

The calculations for the tangent make use of the chain rule. Before the tangent is computed, two partial derivatives of (3.15) and (3.52) that will be useful in the calculation are shown:

$$
\begin{aligned}
\left[\frac{\partial S}{\partial C}\right]_{mjop} =& \mu \frac{\partial J^{-\frac{2}{3}}}{\partial C_{op}} I_{mj} - \left(\frac{\mu I_1}{3}\frac{\partial J^{-\frac{2}{3}}}{\partial C_{op}}\right) C^{-1}_{mj} \\
& - \left(\frac{\mu J^{-\frac{2}{3}}}{3}\frac{\partial I_1}{\partial C_{op}}\right) C^{-1}_{mj} - \left(\frac{\mu J^{-\frac{2}{3}} I_1}{3}\right) \frac{\partial C^{-1}_{mj}}{\partial C_{op}} \\
& + p\left(\frac{\partial J}{\partial C_{op}} C^{-1}_{mj} + J \frac{\partial C^{-1}_{mj}}{\partial C_{op}}\right) \\
=& -\frac{1}{3}\mu J^{-\frac{2}{3}} I_{mj} C^{-1}_{op} + \\
& \left(pJC^{-1}_{op} - \frac{\mu}{3}\left(J^{-\frac{2}{3}} I_{op} - \frac{I_1}{3} J^{-\frac{2}{3}} C^{-1}_{op}\right)\right) C^{-1}_{mj} \\
& + \frac{1}{2}\left(-pJ + \frac{\mu J^{-\frac{2}{3}} I_1}{3}\right)\left(C^{-1}_{mo} C^{-1}_{jp} + C^{-1}_{mp} C^{-1}_{jo}\right),
\end{aligned} \tag{3.94}
$$

and

$$
\begin{aligned}
\left[\frac{\partial C}{\partial F}\right]_{ijkl} &= \frac{[\partial F^T F]_{ij}}{\partial F_{kl}} = \frac{\partial (F^T_{im} F_{mj})}{\partial F_{kl}} \\
&= \frac{\partial F_{mi}}{\partial F_{kl}} F_{mj} + F_{mi} \frac{\partial F_{mj}}{\partial F_{kl}} \\
&= \delta_{mk}\delta_{il} F_{mj} + F_{mi}\delta_{mk}\delta_{jl} \\
&= \delta_{il} F_{kj} + F_{ki}\delta_{jl}.
\end{aligned} \tag{3.95}
$$

Using (3.94-3.95) the tangent associated with the ground matrix is calculated as:

$$
\begin{aligned}
\mathcal{A}_{\mathrm{g},ijkl} &= \left[\frac{\partial \boldsymbol{P}}{\partial \boldsymbol{F}}\right]_{ijkl} \\
&= \frac{\partial (F_{im} S_{mj})}{\partial F_{kl}} \\
&= \frac{\partial F_{im}}{\partial F_{kl}} S_{mj} + F_{im} \frac{\partial S_{mj}}{\partial C_{op}} \frac{\partial C_{op}}{\partial F_{kl}} \\
&= \delta_{ik}\delta_{ml} \left(\mu J^{-\frac{2}{3}} I + \left(pJ - \frac{\mu J^{-\frac{2}{3}} I_1}{3} \right) C^{-1} \right)_{mj} \\
&\quad + F_{im} \left[\left(pJ C^{-1}_{op} - \frac{\mu}{3} \left(J^{-\frac{2}{3}} I_{op} - \frac{I_1}{3} J^{-\frac{2}{3}} C^{-1}_{op} \right) \right) C^{-1}_{mj} \right. \\
&\quad \left. - \frac{1}{2} \left(pJ - \frac{\mu J^{-\frac{2}{3}} I_1}{3} \right) \left(C^{-1}_{mo} C^{-1}_{jp} + C^{-1}_{mp} C^{-1}_{jo} \right) \right] (\delta_{ol} F_{kp} + F_{ko} \delta_{pl}) \\
&\quad + F_{im} \left[-\frac{1}{3} \mu J^{-\frac{2}{3}} C^{-1}_{op} I_{mj} \right] (\delta_{ol} F_{kp} + F_{ko} \delta_{pl}) \\
&= \delta_{ik} (\mu J^{-\frac{2}{3}} I_{lj} + \left(pJ - \frac{\mu J^{-\frac{2}{3}} I_1}{3} \right) C^{-1}_{lj}) \\
&\quad + F_{im} \left[\left(pJ C^{-1}_{lp} - \frac{\mu}{3} \left(J^{-\frac{2}{3}} I_{lp} - \frac{I_1}{3} J^{-\frac{2}{3}} C^{-1}_{lp} \right) \right) C^{-1}_{mj} + \frac{1}{2} \left(-pJ + \frac{\mu J^{-\frac{2}{3}} I_1}{3} \right) \left(C^{-1}_{ml} C^{-1}_{jp} + C^{-1}_{mp} C^{-1}_{jl} \right) \right] F_{kp} \\
&\quad + F_{im} \left[\left(pJ C^{-1}_{ol} - \frac{\mu}{3} \left(J^{-\frac{2}{3}} I_{ol} - \frac{I_1}{3} J^{-\frac{2}{3}} C^{-1}_{ol} \right) \right) C^{-1}_{mj} + \frac{1}{2} \left(-pJ + \frac{\mu J^{-\frac{2}{3}} I_1}{3} \right) \left(C^{-1}_{mo} C^{-1}_{jl} + C^{-1}_{ml} C^{-1}_{jo} \right) \right] F_{ko} \\
&\quad + F_{im} \left[-\frac{1}{3} \mu J^{-\frac{2}{3}} C^{-1}_{lp} I_{mj} \right] F_{kp} + F_{im} \left[-\frac{1}{3} \mu J^{-\frac{2}{3}} C^{-1}_{ol} I_{mj} \right] F_{ko}.
\end{aligned}
$$

The tangent associated with the fibres can be calculated using (3.55),(3.56) and (3.95) and as:

$$
\begin{aligned}
\mathcal{A}_{\mathrm{fib},ijkl} &= \left[\frac{\partial \boldsymbol{P}}{\partial \boldsymbol{F}}\right]_{ijkl} \\
&= \frac{\partial (F_{im} S_{mj})}{\partial F_{kl}} \\
&= \frac{\partial F_{im}}{\partial F_{kl}} S_{\mathrm{fib},mj} + F_{im} \frac{\partial S_{\mathrm{fib},mj}}{\partial C_{op}} \frac{\partial C_{op}}{\partial F_{kl}} \\
&= [\delta_{ik} S_{\mathrm{fib,lj}} \\
&\quad \left. + F_{im} \left[\frac{\partial S_{\mathrm{fib}}}{\partial C} \right]_{mjop} (\delta_{ol} F_{kp} + F_{ko} \delta_{pl}) \right] \\
&= \left[\delta_{ik} \left[(2k_1 G_i) \exp\left\{ k_2 G_i^2 \right\} \frac{\partial G_i}{\partial C} \right]_{lj} \right. \\
&\quad \left. + F_{im} \{ 2 \frac{\partial S_{f,mj}}{\partial I_1} F_{ko} I_{ol} + \frac{\partial S_{f,mj}}{\partial I_4} F_{kp} A^T_{pl} + \frac{\partial S_{f,mj}}{\partial I_4} F_{ko} A_{ol} \} \right],
\end{aligned}
\tag{3.96}
$$

with

$$\left[\frac{\partial S_{\text{fib}}}{\partial C}\right]_{mjop} = \frac{\partial S_{\text{fib},mj}}{\partial I_1}\frac{\partial I_1}{\partial C_{op}} + \frac{\partial S_{\text{fib},mj}}{\partial I_i}\frac{\partial I_i}{\partial C_{op}} \tag{3.97}$$

$$\begin{aligned}
\frac{\partial S_{\text{fib},mj}}{\partial I_1}\frac{\partial I_1}{\partial C_{op}} =& 2k_1\left[\frac{\partial G}{\partial I_1}\exp\left\{k_2G_i^2\right\}\frac{\partial G_i}{\partial C} + G\frac{\partial(\exp\{k_2G_i^2\})}{\partial I_1}\frac{\partial G_i}{\partial C}\right.\\
&\left.+G\exp\left\{k_2G_i^2\right\}\frac{\partial}{\partial I_1}\left(\frac{\partial G_i}{\partial C}\right)\right]_{mj} I_{op}\\
=& 2k_1\left[\kappa J^{-\frac{2}{3}}\exp\left\{k_2G_i^2\right\}\frac{\partial G_i}{\partial C} + 2k_2\kappa G^2J^{-\frac{2}{3}}\exp\left\{k_2G_i^2\right\}\frac{\partial G_i}{\partial C}\right.\\
&\left.\frac{1}{3}\kappa J^{-\frac{2}{3}}G\exp\left\{k_2G_i^2\right\}C^{-1}\right]_{mj} I_{op}
\end{aligned} \tag{3.98}$$

$$\begin{aligned}
\frac{\partial S_{\text{fib},mj}}{\partial I_i}\frac{\partial I_i}{\partial C_{op}} =& 2k_1\left[\frac{\partial G}{\partial I_i}\exp\left\{k_2G_i^2\right\}\frac{\partial G_i}{\partial C} + G\frac{\partial(\exp\{k_2G_i^2\})}{\partial I_i}\frac{\partial G_i}{\partial C}\right.\\
&\left.+G\exp\left\{k_2G_i^2\right\}\frac{\partial}{\partial I_i}\left(\frac{\partial G_i}{\partial C}\right)\right]_{mj} A_{op}\\
=& 2k_1\left[(1-3\kappa)J^{-\frac{2}{3}}\exp\left\{k_2G_i^2\right\}\frac{\partial G_i}{\partial C} + 2k_2G^2(1-3\kappa)J^{-\frac{2}{3}}\exp\left\{k_2G_i^2\right\}\frac{\partial G_i}{\partial C}\right.\\
&\left.+\frac{1}{3}(1-3\kappa)J^{-\frac{2}{3}}G\exp\left\{k_2G_i^2\right\}C^{-1}\right]_{mj} A_{op}.
\end{aligned} \tag{3.99}$$

3.7 Chapter summary

The ALE framework makes it possible to write the balance equations for the fluid in terms of the mesh motion. To describe the mesh motion in the fluid domain a harmonic equation is used. To solve the fluid–structure interaction equations monolithically, the balance equations of both the fluid and solid need to be written in the reference configuration. A fibre–reinforced material is used to model the vessels. The incompressibility of the structure is dealt with by using a two–field variational formula when deriving the weak form. The non–linear discretized equations are solved with Newton's method.

To develop a model for a patient–specific fistula, suitable boundary conditions, geometry and in vivo stress must be included. The next chapter explores the methods and software used to find the mesh, pre–stress and appropriate inlet and outlet boundary conditions.

4

Considerations for a patient–specific model

The model presented in Chapter 3 is a general one. For biomedical applications, attention must be given to the geometry and boundaries of the computational domain. Velocity inlet boundaries can be obtained from MRI data or Doppler–ultrasonography. The inlet and outlet are not physical boundaries but result from truncating the computational domain. Dirichlet and Neumann boundary conditions are insufficient to let waves pass unhindered through the outlet boundaries. For a patient–specific model, geometrical data obtained from computed tomography (CT) or MRI should be processed in order to generate the computational mesh. This generated geometry is not in a configuration that is stress free and an appropriate pre–stress should be calculated so that the generated geometry can be used in simulations. The purpose of this chapter is to discuss these features and the methods used to include them in the computational model.

4.1 Boundary Conditions

4.1.1 Inlet

Velocities at the inlet of the fistula can be obtained from MRI or Doppler ultrasonography. 2D MRI slices capturing velocity encoded data (normal to the slice) of the artery and surrounding areas were taken for a number of time slabs within a heartbeat. The MRI was ECG (electrocardiogram) gated, i.e. synchronized with the beating heart, in order to find an accurate and sufficient temporal resolution.

These velocities were obtained as a 3D array in Matlab [58]. The velocity perpendicular to the slice can be shown for each time slab (see Fig. 4.1(a)). From this the velocity at a point over time as well as the velocity profile across the inlet can be obtained (see Fig. 4.1(b) and (c)).

The velocity across the mid line of the slice has a profile that is close to a parabolic shape. For this reason the maximum velocity over the period of the heartbeat was found and the velocity profile assumed to be parabolic. Another reason for approximating the velocity profile is that MRI data is not always generally available to find 2D velocities. A more practical and accesible way to find the velocities at the inlet, would be to use Doppler–ultrasonography. The output of the ultrasound is a single value of the velocity over time. In order to use this data to prescribe the flow at the inlet, the assumption of a parabolic velocity profile needs to be made.

4.1.2 Outlet conditions

Outlet boundary conditions for cardiovascular applications are not trivial to prescribe. As the boundary is only a computational and not a physical one, the effect that the downstream vasculature has on the domain needs to be taken into account when prescribing a boundary condition. Waves should be able to travel through the domain unhindered. These waves travel at the speed of sound of the system.

Another complication that arises from imposing an artificial outlet boundary condition is simulation divergence due to back flow. The back flow stabilization implemented to circumvent this complication is discussed below.

A Windkessel model is used to describe the non–reflecting boundary conditions. The weak form and linearization of this boundary term follows the discussion of back flow stabilization.

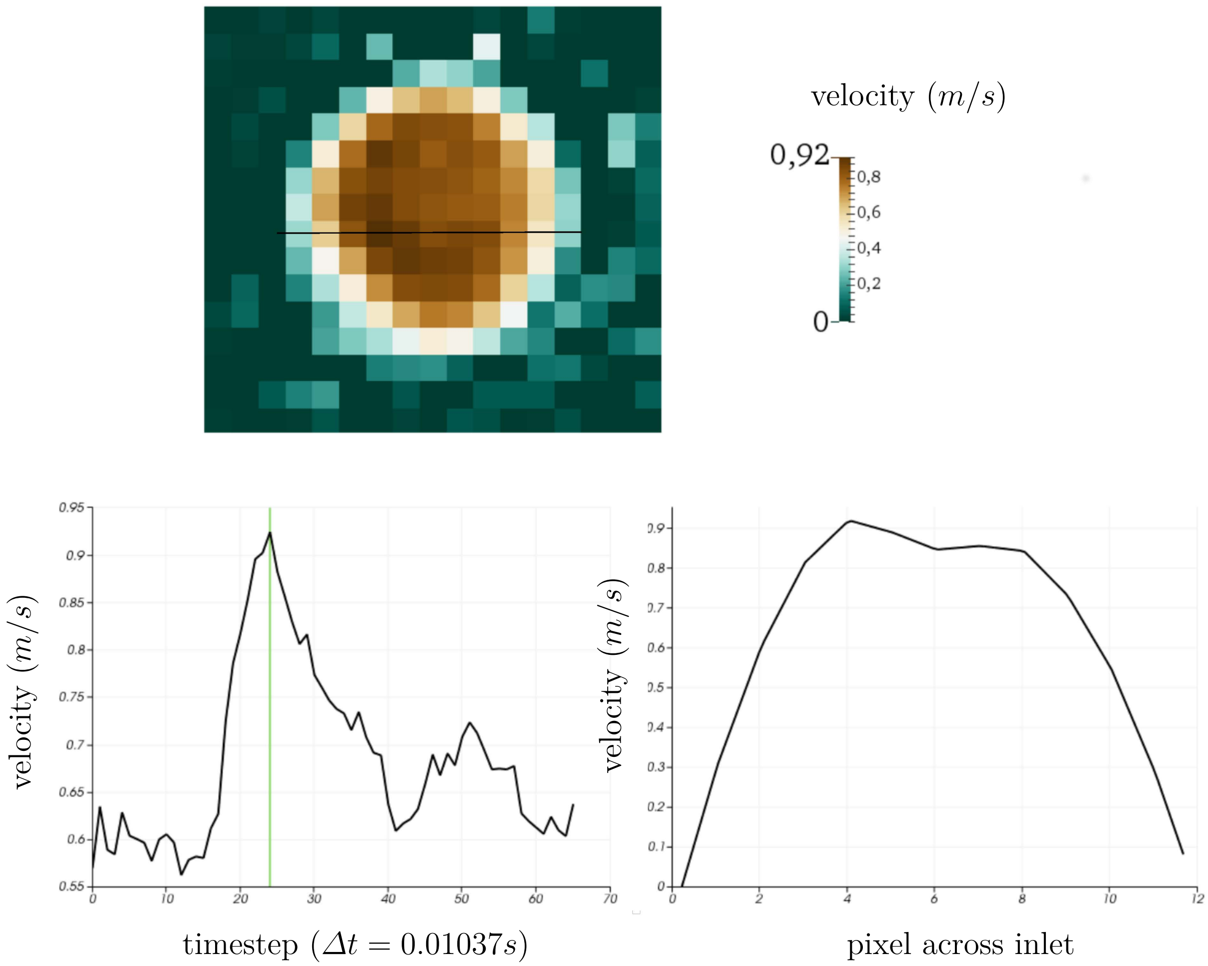

Fig. 4.1: Inlet boundary conditions at $t = 0.249s$: (a) a processed image from MRI; (b) the velocity at a point on the inlet over the period of a heartbeat; (c) the velocity profile across the artery.

Back flow stabilization

Back flow is a physiological phenomenon in which flow reversal takes place. These local flow dynamics must be captured in a simulation. Complex geometries such as the presence of stenoses, anastomoses or an increased cross sectional area are a common cause of flow separation, flow recirculation or vortex shedding [74]. Back flow at a boundary can give rise to simulation divergence. These numerical instabilities originate when Neumann boundary conditions on the outlet faces are imposed and the velocity profile is not specified. To prevent artificial alteration of local flow dynamics, careful treatment is necessary when modelling back flow.

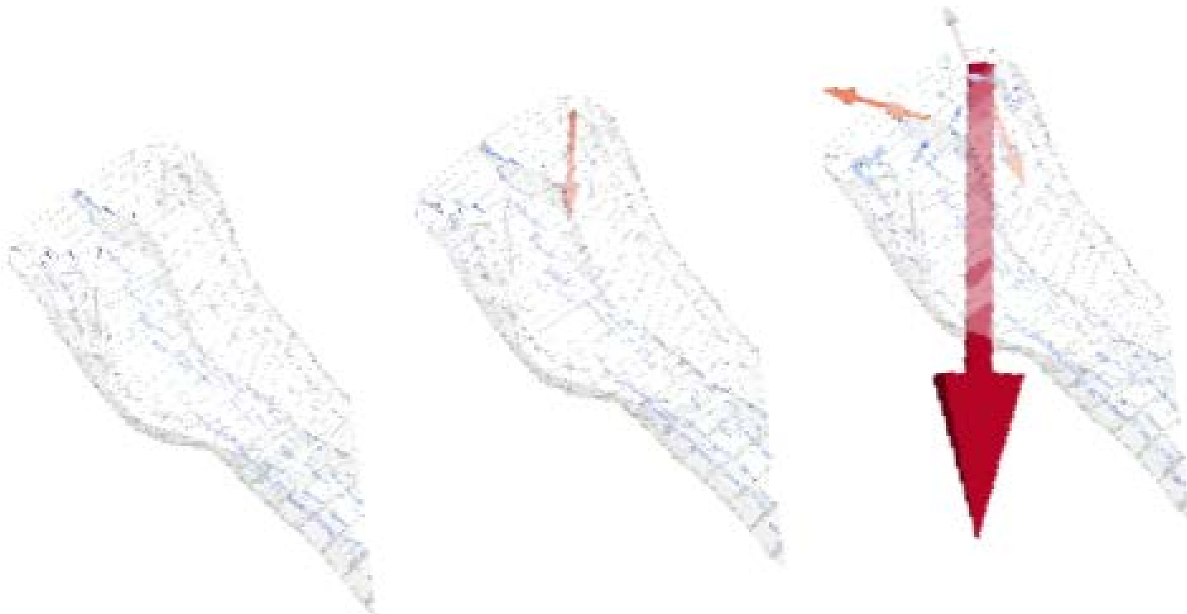

Fig. 4.2: Velocity vectors at different time steps showing simulation divergence at an outlet as a result of numerical instabilities in the presence of back flow.

There are several methods available in the literature for solving the issue of back flow divergence. It is very simple to artificially elongate the outlets by adding straight sections, or to add additional vessels to the model until the flow becomes unidirectional. However, these methods increase the model generation and computational costs significantly. In [74] the authors considered three alternative methods currently in use when solving the issue of back flow divergence in finite element solvers. The impact on the flow physics, implementation effort, computational cost and robustness were compared.

In addition to back flow stabilization, the two further methods in use are confining the back flow velocity to a desired direction, and the use of Lagrange–multipliers to constrain the velocity profile. When confining the back flow velocity direction, the linearized equations are rotated by a matrix into the normal and tangential directions. A zero Dirichlet velocity is then imposed on the tangential directions at the outlet. To constrain the velocity profile, an augmented Lagrangian formulation is used.

Outlet stabilization, a method first proposed in [11] and augmented in [74], adds an additional convective traction on the outflow boundary. This traction is an outward traction, in the opposite direction of back flow. The purpose of this traction is to provide the convective flow information that is not present as a result of the artificial outlet boundary.

The results from [74] are summarized in Table 4.1. The back flow stabilization method has the highest robustness, smallest impact on the flow field, is easy to use and has no additional computational cost.

Table 4.1: Summary of comparison in [74] between methods solving the issue of backflow divergence

	Back flow stabilization	Back flow in normal direction only	Prescribed velocity profile
Stability	Stable	Unstable	Stable
Flow physics	Similar	Similar	Significant change
Computational cost	Not expensive	Not expensive	Expensive
Implementation effort	Minimal	Minimal	High

To include back flow stabilization of the fluid, the traction boundary term $\int_{\Gamma_{\mathrm{f}}} (\boldsymbol{\phi}^{\boldsymbol{v}} \cdot \boldsymbol{g})\, \mathrm{dS}$ in the weak form of the momentum equation (3.41) must be augmented for the outflow boundaries $\int_{\Gamma_{\mathrm{out}}}$. The back flow stabilization method adds an extra convective traction to the outlet conditions that is only active when back flow is present. At the outlets the following must hold:

$$\boldsymbol{n} \cdot \tilde{\boldsymbol{\sigma}} \boldsymbol{n} + R \int_{\Gamma_{\mathrm{out}}} \boldsymbol{v} \cdot \boldsymbol{n}\, \mathrm{dS} + p_0 = 0. \tag{4.1}$$

Here

$$\tilde{\boldsymbol{\sigma}} \boldsymbol{n} = -p\boldsymbol{n} + \rho_{\mathrm{f}} \nu_{\mathrm{f}} (\nabla \boldsymbol{v} \boldsymbol{F}^{-1} + \boldsymbol{F}^{-T} \nabla \boldsymbol{v}^T) \boldsymbol{n} - \rho_{\mathrm{f}} \beta \boldsymbol{v} (\boldsymbol{v} \cdot \boldsymbol{n})_{-}. \tag{4.2}$$

The second term in (4.1) represents a pressure that is a function of the flow over the boundary. This term will be discussed in more detail in the next section. Here $0 < \beta < 1$ and $(\boldsymbol{v} \cdot \boldsymbol{n})_{-}$ denotes the part associated with back flow of $\boldsymbol{v} \cdot \boldsymbol{n}$; that is;

$$(\boldsymbol{v} \cdot \boldsymbol{n})_{-} = \begin{cases} -\boldsymbol{v} \cdot \boldsymbol{n}, & \text{if } \boldsymbol{v} \cdot \boldsymbol{n} < 0, \\ 0, & \text{otherwise.} \end{cases} \tag{4.3}$$

When applying this boundary condition this additional term must be added to the weak form of the fluid equations (3.41). It is written in the reference configuration and using Nanson's law, $\boldsymbol{n}\,\mathrm{dS_t} = \mathrm{J}\boldsymbol{F}^{-\mathrm{T}}\boldsymbol{N}\,\mathrm{dS}$, the traction boundary term in $(3.41)_a$ is given by

$$\begin{aligned} \int_{\Gamma_{\text{out}}} (\boldsymbol{\phi}^{\boldsymbol{v}} \cdot \boldsymbol{g})\,\mathrm{dS} = &- \int_{\Gamma_{\text{out}}} \boldsymbol{\phi}^{\boldsymbol{v}} \cdot \rho_{\mathrm{f}} \boldsymbol{v} (\boldsymbol{v} \cdot J\boldsymbol{F}^{-T}\boldsymbol{N})_{-}\,\mathrm{dS} \\ &+ \left(\int_{\Gamma_{\text{out}}} \boldsymbol{\phi}^{\boldsymbol{v}} \cdot J\boldsymbol{F}^{-T}\boldsymbol{N}\,\mathrm{dS} \right) \left(R \int_{\Gamma_{\text{out}}} \boldsymbol{v} \cdot J\boldsymbol{F}^{-T}\boldsymbol{N}\,\mathrm{dS} + p_0 \right). \end{aligned} \tag{4.4}$$

The resistive boundary condition can be generalized so that any functional relationship between the normal stress and blood flow rate can be prescribed so that (4.1) becomes:

$$\boldsymbol{n} \cdot \tilde{\boldsymbol{\sigma}} \boldsymbol{n} + f(Q_{\text{out}}) = 0, \tag{4.5}$$

where

$$Q_{\text{out}}(\boldsymbol{v}, \boldsymbol{F}) = \int_{\Gamma_{\text{out}}} \boldsymbol{v} \cdot J\boldsymbol{F}^{-T}\boldsymbol{N}\,\mathrm{dS}. \tag{4.6}$$

The linearization of this boundary condition requires a precomputed global vector which contains the linearization of the flow terms

$$D_{\Delta \boldsymbol{v}} Q_{\text{out}} = \int_{\Gamma_{\text{out}}} \Delta \boldsymbol{v} \cdot J\boldsymbol{F}^{-T}\boldsymbol{N}\,\mathrm{dS}. \tag{4.7}$$

The linearization of the second term in (4.4) using the generalized resistive boundary condition is given by

$$D_{\Delta \boldsymbol{v}} f(Q_{\text{out}}) = \left(\int_{\Gamma_{\text{out}}} \boldsymbol{\phi}^{\boldsymbol{v}} \cdot J\boldsymbol{F}^{-T}\boldsymbol{N}\,\mathrm{dS} \right) (f'(Q_{\text{out}})) D_{\Delta \boldsymbol{v}} Q_{\text{out}}. \tag{4.8}$$

For a the particular case of a purely resistive boundary, such as present in (4.4), $f(Q_{\text{out}}) = RQ_{\text{out}}$ and the derivative to be used in (4.8) is $(f'(Q_{\text{out}})) = R$.

The Windkessel model

The choice of outflow boundary conditions has a significant effect on both the velocity and the pressure fields of a 3D blood flow simulation. To prescribe either flow or pressure at the outlets is not practical, as it is difficult to obtain such data and also to synchronize these waveforms in a way that is consistent with the wave propagation and thus the wall properties. A common practice is to prescribe, not the flow rate or the pressure, but rather the functional relationship that exists between the pressure and flow. The simplest of these relations is the resistive boundary condition that is shown in (4.1). A lumped parameter model is used to describe the relation and this 0D model can be directly coupled to the 3D equations. The lumped parameter models are described by ordinary differential equations that represent the dynamic description of the physics whilst neglecting the spatial variation of its parameters and variables. By using the multi–domain method [34], these ODEs can be incorporated in the weak form of the equation. Apart from the resistive effects of the downstream vessels, the compliance of the vessels should also be taken into account. Different forms of the Windkessel model are available in the literature to incorporate both the resistance and capacitance of non–periodic blood flow.

We follow the implementation in [97] where a three–element Windkessel is used (Fig. 4.3). It consists of a resistance in series with a parallel configuration of a capacitance and resistance.

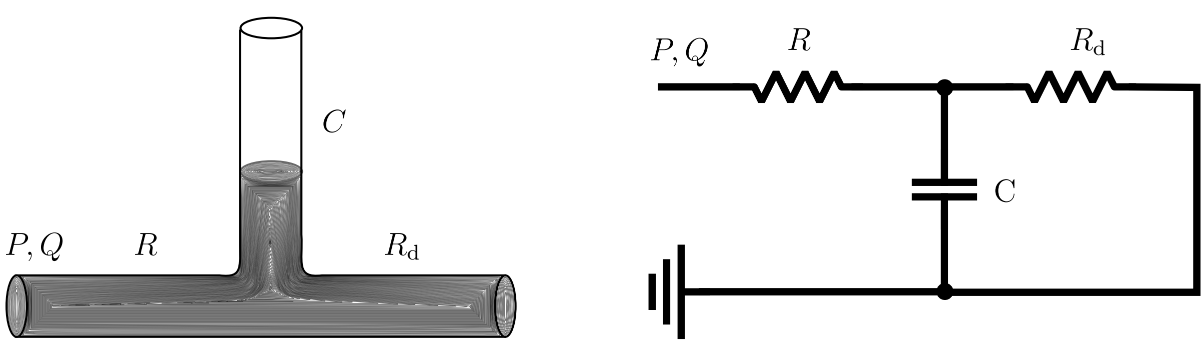

Fig. 4.3: The Windkessel model presented mechanically (left) and through an electrically analogue (right).

Weak form

To prescribe this relationship between the flow and pressure, $f(Q_{\text{out}})$ is given by

$$f(Q_{\text{out}}) = RQ_{\text{out}} + \int_0^{t_{n+1-\alpha_\text{f}}} \frac{e^{-\frac{t-s}{\tau}}}{C} Q_{\text{out}}\,\text{ds} \tag{4.9}$$

where C is the capacitance, R the resistance at the outlet, $\tau = R_\text{d}C$ the relaxation parameter and R_d the resistance downstream.
The velocity evaluated at some time s during the timestep t^l to t^{l+1} is given by

$$\begin{aligned} \boldsymbol{v}(s) &= \boldsymbol{v}^l + (\boldsymbol{v}^{l+1} - \boldsymbol{v}^l)\left(\frac{s - t_l}{t_{l+1} - t_l}\right) \\ &= \boldsymbol{v}^l \left(\frac{t_{l+1} - s}{\triangle t}\right) + \boldsymbol{v}^{l+1}\left(\frac{s - t_l}{\triangle t}\right). \end{aligned} \tag{4.10}$$

After time discretization $f(Q_{\text{out}}^{n+1-\alpha_\text{f}})$ can be evaluated by

$$f(Q_{\text{out}}^{n+1-\alpha_f}) = R\left((1-\alpha_\text{f})Q^{n+1} + \alpha_\text{f} Q^n\right) + h^{n+1}, \tag{4.11}$$

where h^{n+1} is given by

$$h^{n+1} = \left(e^{-\frac{\triangle t}{\tau}}\right) h^n + \int_{t_n}^{t_{n+1-\alpha_\text{f}}} \frac{e^{-\frac{t-s}{\tau}}}{C}\left(Q_{\text{out}}^n \left(\frac{t_{n+1} - s}{\triangle t}\right) + Q_{\text{out}}^{n+1}\left(\frac{s - t_n}{\triangle t}\right)\right) \text{ds}. \tag{4.12}$$

Finally, after integrating over time,

$$\begin{aligned} h^{n+1} = \left(e^{-\frac{\triangle t}{\tau}}\right) h^n + R_d \Bigg[& Q^n \left(\frac{t_{n+1} - t_{n+1-\alpha_\text{f}}}{\triangle t} - e^{-\frac{t-s}{\tau}} + \frac{\tau}{\triangle t}\left(1 - e^{-\frac{t-s}{\tau}}\right)\right) \\ & + Q^{n+1}\left(\frac{t_{n+1-\alpha_\text{f}} - t_n}{\triangle t} - \frac{\tau}{\triangle t}\left(1 - e^{-\frac{t-s}{\tau}}\right)\right)\Bigg]. \end{aligned} \tag{4.13}$$

Linearization

The find the directional derivative with an incremental change in the velocity field $\Delta \boldsymbol{v}$, (4.8) is used and the derivative of $f(Q_{\text{out}})$ is given by:

$$f'(Q_{\text{out}}) = \left(R + \int_{t_n}^{t_{n+1-\alpha_\text{f}}} \frac{e^{-\frac{t-s}{\tau}}}{C}\left(\frac{s - t_n}{\triangle t}\text{ds}\right)\right). \tag{4.14}$$

The directional derivative of $f(Q_{\text{out}})$ with respect to an incremental change in the displacement field $\Delta \boldsymbol{u}$ is:

$$
\begin{aligned}
D_{\Delta u} f(Q_{\text{out}}) =& R \int_{\Gamma_{\text{out}}} \boldsymbol{v} \cdot \left(D_{\Delta u} J \boldsymbol{F}^{-T} + J D_{\Delta u} \boldsymbol{F}^{-T} \right) \boldsymbol{N} \, \mathrm{dS} \\
&+ \int_0^{t_{n+1-\alpha_\mathrm{f}}} \frac{e^{-\frac{t-s}{\tau}}}{C} \int_{\Gamma_{\text{out}}} \boldsymbol{v} \cdot \left(D_{\Delta u} J \boldsymbol{F}^{-T} + J D_{\Delta u} \boldsymbol{F}^{-T} \right) \boldsymbol{N} \, \mathrm{dS} \, \mathrm{ds}. \qquad (4.15)
\end{aligned}
$$

4.1.3 Damping of structure

In a similar fashion in which the Windkessel model enables the pressure waves to exit the computational domain unhindered, the waves should be able to exit the structural domain without being reflected. In others words the energy of the waves should be absorbed. This is done by extending the computational domain of the structure artificially and by adding damping terms to the artificial structure [98].

Weak form

To include the damping of the structure, (3.58) is changed to

$$
\begin{aligned}
&\int_{\Omega_\mathrm{s}} \left(\boldsymbol{\phi}^{\boldsymbol{v}} \cdot \rho_s \frac{\partial \boldsymbol{v}}{\partial t} \right) \mathrm{dV} + \int_{\Omega_\mathrm{s}} \left(\nabla \boldsymbol{\phi}^{\boldsymbol{v}} \cdot \boldsymbol{P} \right) \mathrm{dV} \\
&\quad - \int_{\Gamma_\mathrm{s}} \left(\boldsymbol{\phi}^{\boldsymbol{v}} \cdot \boldsymbol{g} \right) \mathrm{dS} + \gamma_\mathrm{w} \int_{\Omega_\mathrm{s}} \left(\boldsymbol{\phi}^{\boldsymbol{v}} \cdot \boldsymbol{v} \right) \mathrm{dV} \\
&\quad + \gamma_\mathrm{s} \int_{\Omega_\mathrm{s}} \left(\nabla \boldsymbol{\phi}^{\boldsymbol{v}} \cdot \frac{1}{2} \left(\nabla \boldsymbol{v} + \nabla \boldsymbol{v}^T \right) \right) \mathrm{dV} = 0 \qquad \forall \boldsymbol{\phi}^{\boldsymbol{v}} \in \mathcal{V}^0, \qquad (4.16)
\end{aligned}
$$

where γ_w and γ_s denotes the strong and weak damping coefficients respectively and $\gamma_\mathrm{w}, \gamma_\mathrm{s} \geq 0$.

The linearization of the damping terms is trivial and therefore not shown here.

4.2 Geometry acquisition and processing

To capture the different flow patterns in each patient with a finite element simulation, a mesh representing the patient's specific geometry is necessary. To use deal.II to implement the finite element simulation, this mesh needs to consist of quadrilateral and hexahedral elements only. We need a way to process MRI or CT into a CAD model and from there create a hexahedral mesh that in turn should be formatted in such a way that deal.II can import this mesh (Fig. 4.4).

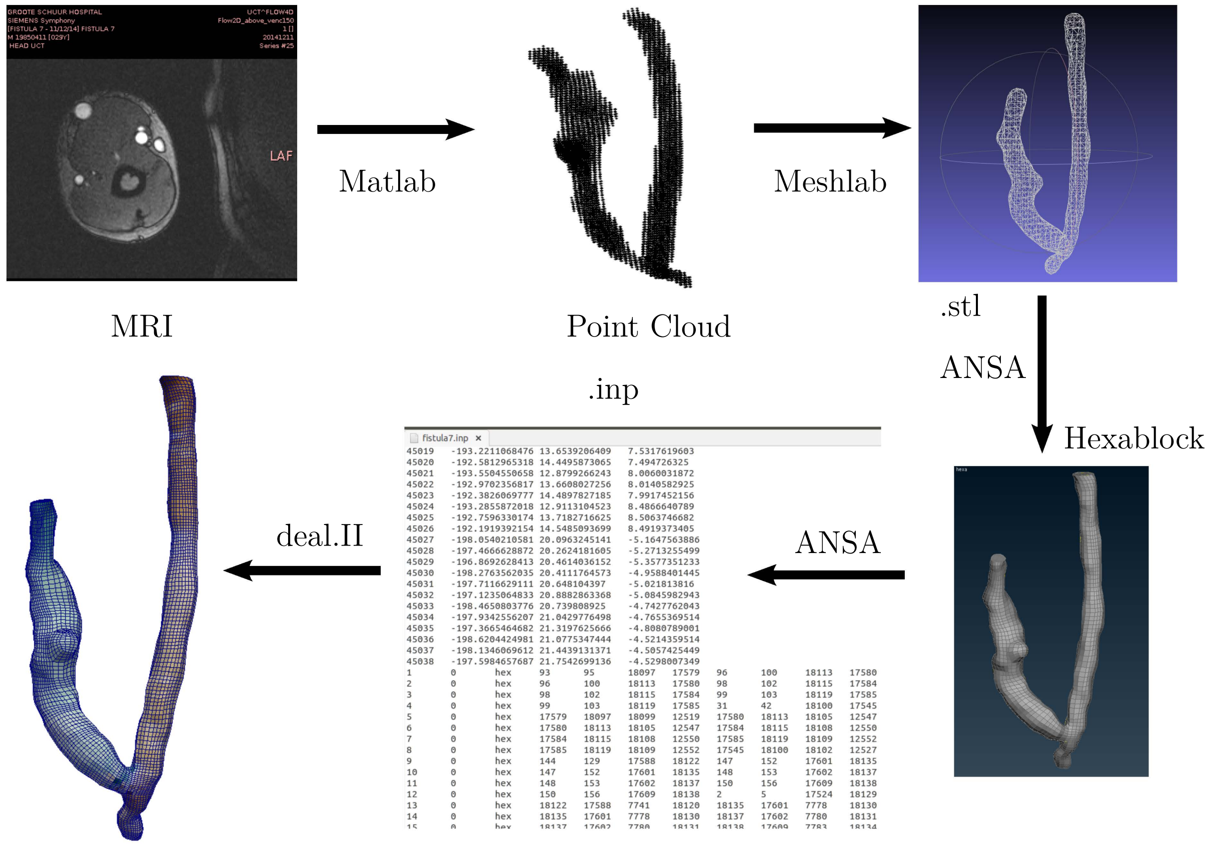

Fig. 4.4: Flowchart showing the process to create patient–specific geometry.

3D MRI or CT can be used in conjunction with 3D image processing and mesh generation software such as ScanIP [88] to obtain a mesh. Unfortunately the default ScanIP mesh, consists of tetrahedral elements, and the hexahedral elements are derived from the tetrahedral elements, and as a result are of poor quality. The geometry created by Simpleware can however be exported in a STL (Stereo Lithography) file format and imported into a meshing software that has the ability to create hexahedral elements. This approach would be suitable in the future because CT scanners are more readily available than MRI scanners. For the present work, the 4D MRI provides a short cut to extracting the geometrical data with the 4D Flow tool (Siemens AG). It produces a point cloud of all data points for which the flow is above a certain threshold over time. The resulting point cloud was converted into an STL format using Meshlab [24]. The geometry from the 4D flow tool smoothes the geometry and neglects some of the features of the fistula. The generation of the geometry using ScanIP is however more time intensive.

The STL file was imported into the meshing software ANSA [13]. The hexablock tool in ANSA can be used to create a mesh consisting of only hexahedral elements. The mesh was exported as a .inp (Abaqus) file and small changes made in order that deal.II can import the mesh.

4.2.1 Pre–stress

The geometry from the MRI which will be used for the simulations is in a configuration that is neither load nor stress free. To find the zero stress state for a patient–specific vessel is not trivial, but can be done by inverse analysis [42].

We chose to instead find the pre–stress that is present in the known geometry. It is assumed that the vessel and blood are in equilibrium for the geometry obtained from the MRI. There are two ways of applying this pre–stress: to apply an a additional deformation gradient or add an additional stress to the structure. In [42] an iterative method that is based on a modified updated Lagrangian formulation is presented to find the pre–stressed state for a known geometric configuration. The deformation gradient $\tilde{\boldsymbol{F}}$ is updated until the system is in equilibrium and this altered deformation gradient is then stored. When running the forward simulations, the deformation gradient used to calculate the stress is changed to $\boldsymbol{F}_{\text{forward}} = \boldsymbol{F}(\boldsymbol{u})\tilde{\boldsymbol{F}}$.

We follow [52] to find the pre–stress $\boldsymbol{S}_0$ that is present in the known configuration directly. To do this the first Piola–Kirchhoff stress tensor in (3.58) is calculated from $\boldsymbol{P} = \boldsymbol{F}(\boldsymbol{S} + \boldsymbol{S}_0)$. To determine $\boldsymbol{S}_0$ it must be noted that when $\boldsymbol{F} = \boldsymbol{I}$ or $\boldsymbol{u} = \boldsymbol{0}$ the blood vessel is in equilibrium with the forces present in the blood flow.

In other words the symmetric pre–stress tensor $\boldsymbol{S}_0$ needs to be found such that for all $\boldsymbol{\phi}^{\boldsymbol{u}}$,

$$\int_{\Omega} \nabla \boldsymbol{\phi}^{\boldsymbol{u}} \cdot \boldsymbol{S}_0 \mathrm{dV} + \int_{\Gamma_{\mathrm{i}}} (\boldsymbol{\phi}^{\boldsymbol{u}} \cdot \tilde{\boldsymbol{g}}) \, \mathrm{dS} = 0, \tag{4.17}$$

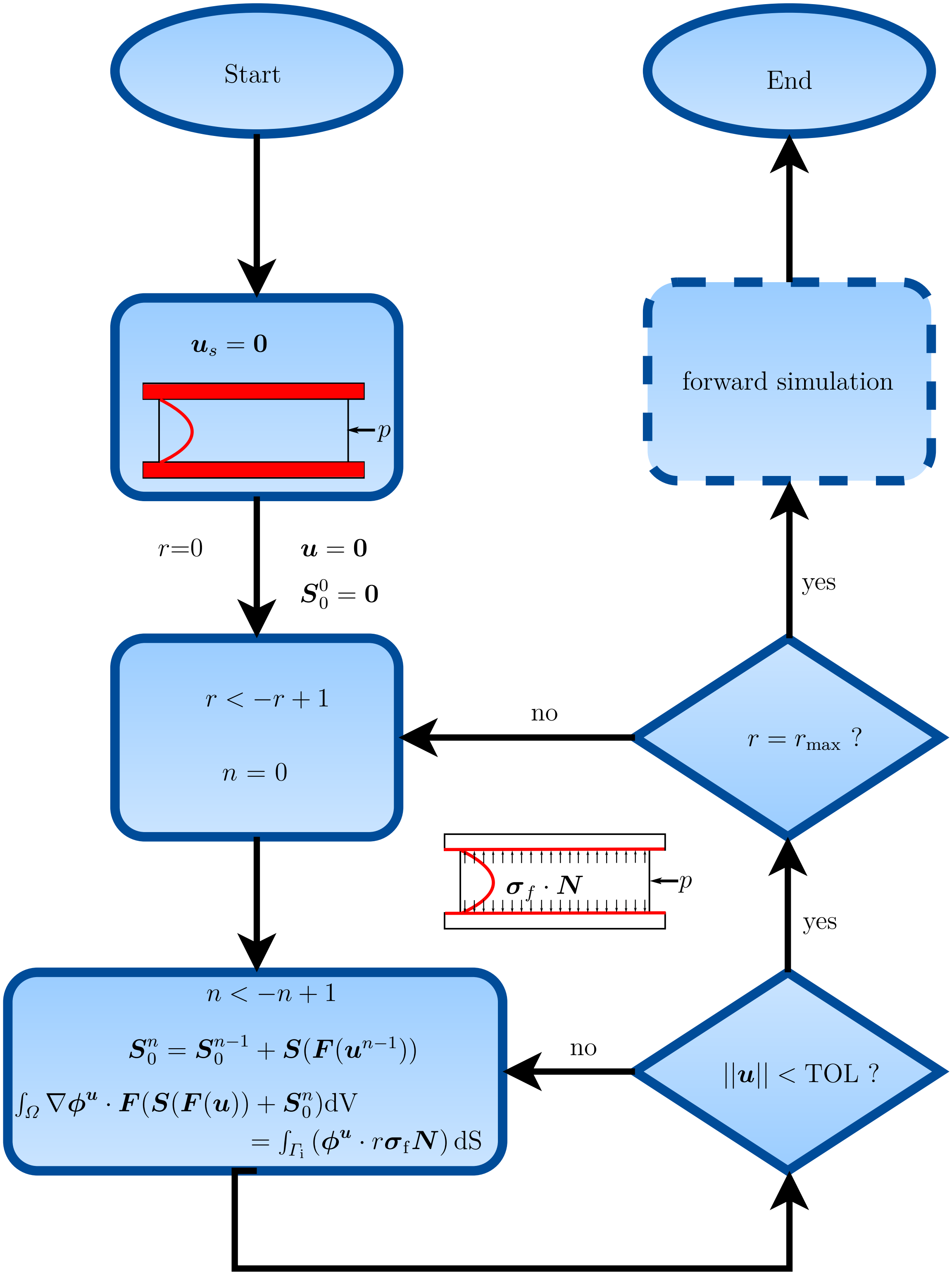

Fig. 4.5: Calculating the prestress.

where $\tilde{\boldsymbol{g}}$ is the fluid traction vector.

The computational strategy used to determine $\boldsymbol{S}_0$ is shown in Fig. 4.5. Firstly $\tilde{\boldsymbol{g}}$ is determined by using a rigid wall simulation with a physiological realistic pressure applied at the outlet. This traction vector is applied incrementally on $\Gamma_{i,s}$ by using r/r_{max}. For $r = 0$, $\boldsymbol{S}_0^0 = \boldsymbol{0}$, and $\boldsymbol{u} = \boldsymbol{0}$. For each increment $\boldsymbol{S}_0$ is found so that $\boldsymbol{u} = \boldsymbol{0}$ and thus $\boldsymbol{F} = \boldsymbol{I}$. This is done in an iterative manner:

1. Update the pre–stress: $\boldsymbol{S}_0^n = \boldsymbol{S}_0^{n-1} + \boldsymbol{S}^{n-1}$
2. Solve for $\boldsymbol{u}$:

$$\int_{\Omega} \nabla \boldsymbol{\phi}^{\boldsymbol{u}} \cdot \boldsymbol{F}(\boldsymbol{S} + \boldsymbol{S}_0^n)\mathrm{dV} + \int_{\Gamma_\mathrm{i}} (\boldsymbol{\phi}^{\boldsymbol{u}} \cdot \tilde{\boldsymbol{g}})\,\mathrm{dS} = 0, \tag{4.18}$$

This is done until $\boldsymbol{u} = \boldsymbol{0}$. When the total load has been applied the forward simulation can commence.

4.2.2 Fibre directions

Two preferred directions should be prescribed when using the material model (3.49). This is done by prescribing the angle between the local coordinate system and the fibre directions (Fig. 4.6). For a block or cylinder this is straightforward and the global Cartesian or cylindrical coordinate system can be used to find the local coordinate system. For a patient–specific geometry with vessel bifurcations a different strategy must be adopted.

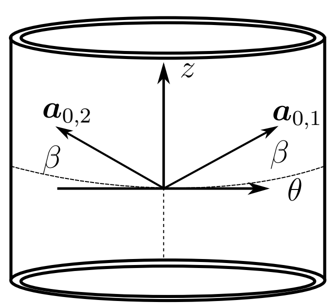

Fig. 4.6: Prescribing preferred directions.

The principal stress distribution of a cylindrical tube under internal pressure was studied in [1]. It was observed that the maximum principal stress is always positive and in the circumferential direction, the direction of the intermediate principal stress is in line with the axial line of the vessel and the minimum principal stress is aligned with the radial direction. This idea was used to determine the local coordinate system. This was implemented explicitly when calculating the pre–stress. After $\boldsymbol{S}_0$ was determined for each increment of the load, the eigenvalue problem was solved for $\boldsymbol{S}_0$. In other words the principal stresses (eigenvalues) and directions of the principal stresses (eigenvectors) were determined: $\boldsymbol{S}_0 = \sum S_{0,a}\boldsymbol{n}_a \otimes \boldsymbol{n}_a, \ \ a = 1, 2, 3$. With the directions of the principal stresses $\boldsymbol{n}_a$ known,the fibre directions $\boldsymbol{a}_{0,i}$ can be determined when the angle β defining the direction is given (Fig. 4.7).

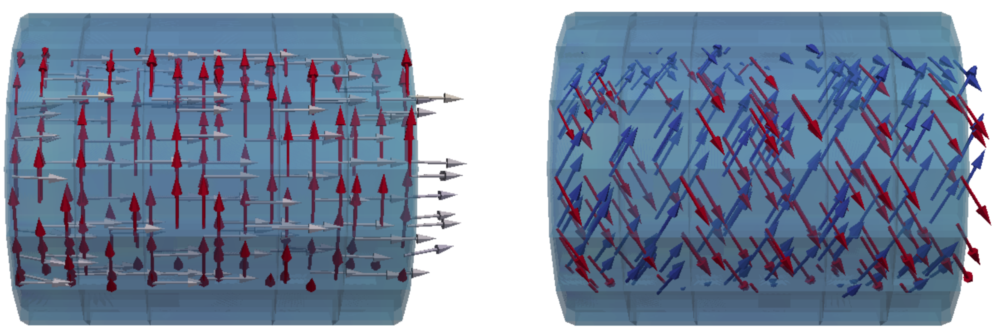

Fig. 4.7: The direction of the principal stresses (left) and associated fibre directions (right) in a cylinder.

4.2.3 Velocity encoded MRI

Verification and validation of the mathematical model and numerical implementation of the fluid–structure interaction is very important. To verify that the model was implemented correctly, several benchmark examples were created to test different parts of the code. To validate biomedical models is more complicated. Data from 4D velocity encoded MRI was used to compare the flow in the fistula from the simulations to the flow in the patients [71].

Other technologies that have been used for validation purposes are Doppler ultrasound and computed tomography. While Doppler ultrasound is more widely available and

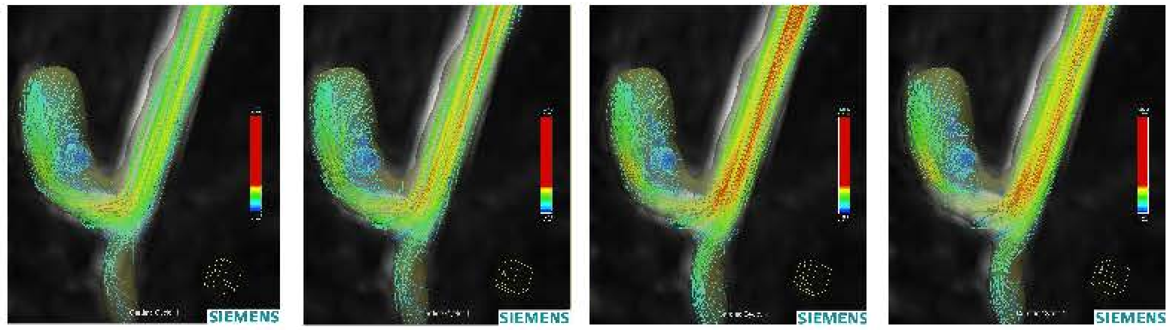

Fig. 4.8: Processed flow results from the 4D MRI at different times during the heart cycle.

easier to use, it is limited because it detects only the component of the velocity directed to or from the transducer. It is a less accurate measure because it is subject to user variability. Although computed tomography has excellent spatial resolution, it can not measure velocity and can therefore not be used to validate flow patterns.

4D velocity acquisition is also known as "3D cine" acquisition. It employs phase contrast magnetic resonance to measure the three directional velocity components of blood flow, for the three spatial dimensions and the temporal dimension. It is a combination of 3D spatial encoding, three–directional velocity encoding and cine acquisition. The data it provides makes the visualization of the temporal evolution of complex flow patterns throughout a volume possible (see for example Fig 4.8). The collection of these data sets relies on efficient synchronization relative to cardiac movements. The time dimension of this cine velocity acquisitions does not represent real time but rather an effectively averaged heart cycle. This means that it does not capture any instabilities or beat–to–beat variations of the blood flow.

4.3 Chapter Summary

This chapter has dealt with the considerations relevant to modelling patient–specific flow. It looked at the data acquisition necessary to create the computational mesh, prescribe the inlet flow and validate the flow. It has also considered the extensions necessary to the weak form of the model by including pre–stress and the directions of the fibres. The third aspect covered has been the method to absorb outgoing waves using the Windkessel model and damping of the structure.

The next chapter describes the numerical implementation of the mathematical model.

5

Implementation

This chapter focuses on the implementation of the model within the open–source library deal.II [8]. Some attention is given to the finite element formulation and the elements used. The block structure of the discrete linearized equations is shown, before and after the use of Gauss quadrature. The Gauss quadrature are shown in a format that resembles the deal.II implementation. Attention is drawn to the implementation of the boundary conditions in deal.II.

To solve the fluid–structure interaction of a patient–specific model a fine mesh is required, resulting in a very large number of degrees of freedom. To solve this large system of equations within a reasonable time frame, the finite element code was adapted to run in parallel. The second section of this chapter is devoted to the software and data structures that were necessary to run the code in parallel.

5.1 Finite element formulation in deal.II

In Section 3.5.3 the equations were developed in terms of global interpolants or shape functions and nodal unknowns. Recall that the domain was divided into n_e elements with N nodes. An element is denoted by Ω^e. The global residual (3.76) can be replaced by the sum of the integrals on the n_e elements:

$$R(\boldsymbol{U}_h^n)(\boldsymbol{\phi}_h^{\boldsymbol{v}}, \boldsymbol{\phi}_h^{\boldsymbol{u}}, \phi_h^p) = \sum_e^{n_e} R^e(\boldsymbol{U}_h^n)(\boldsymbol{\phi}_h^{\boldsymbol{v}}, \boldsymbol{\phi}_h^{\boldsymbol{u}}, \phi_h^p) = 0, \qquad \forall \boldsymbol{\phi}_h \in \mathcal{X}_h^0. \tag{5.1}$$

Up to this point, nothing has been said about the interpolants used for the Galerkin approach in (3.76). The equations are solved monolithically, and Q_2^c/P_1^{dc} finite elements are used to approximate the continuous unknowns and weight functions. This comprises a continuous triquadratic element for the displacement field and a discontinuous linear element for the pressure field (Fig. 5.1). The Q_2^c/P_1^{dc} element is a good choice to impose the incompressibility in the fluid and to prevent locking in the incompressible solid.

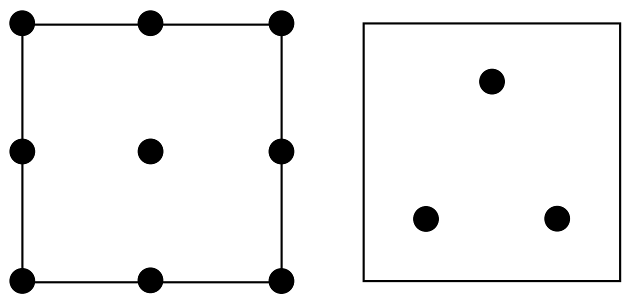

Fig. 5.1: The Q_2^c/P_1^{dc} shown in 2D. It consists of a continuous quadratic element (left) and a discontinuous linear element (right).

5.1.1 The block–structure of the equations

In Section 3.6 the linearization of the non–linear equations and Newton's method were discussed (3.77). The block–structure of the linear system of equations is described here.

The linear system of equations that are solved has the form:

$$\boldsymbol{A}\boldsymbol{x} = \boldsymbol{b}, \tag{5.2}$$

where $\boldsymbol{A}$ denotes the tangent matrix, $\boldsymbol{b}$ the residual vector and $\boldsymbol{x}$ the change in the solution vector. Referring to the discretized form of the equations from Sections 3.4 and 3.6 the block–structure of the linearized equation can be expanded:

$$\begin{bmatrix} (3.78) & 0 & (3.79) & 0 & (3.83) & 0 \\ 0 & (3.87) & 0 & (3.88) & 0 & (3.89) \\ 0 & 0 & (3.86) & 0 & 0 & 0 \\ 0 & (3.90) & 0 & (3.91) & 0 & 0 \\ (3.84) & 0 & (3.85) & 0 & 0 & 0 \\ 0 & 0 & 0 & (3.92) & 0 & 0 \end{bmatrix} \begin{bmatrix} \delta \boldsymbol{v}_f \\ \delta \boldsymbol{v}_s \\ \delta \boldsymbol{u}_f \\ \delta \boldsymbol{u}_s \\ \delta p_f \\ \delta p_s \end{bmatrix} = \begin{bmatrix} R_{\boldsymbol{v},f} & (3.41_a) \\ R_{\boldsymbol{v},s} & (3.58) \\ R_{\boldsymbol{u},f} & (3.61) \\ R_{\boldsymbol{u},s} & (3.59) \\ R_{p,f} & (3.41_b) \\ R_{p,s} & (3.60) \end{bmatrix}. \tag{5.3}$$

5.1.2 Numerical integration and deal.II implementation

Numerical integration is carried out by using Gauss quadrature on each element. To illustrate Gauss quadrature and how it correlates with the deal.II implementation the second entry of the right hand side vector (the integral on Ω_s of the terms associated with the velocity degrees of freedom (3.58)) is, for an element,

$$\begin{aligned} R^e_{\boldsymbol{v},\mathrm{s}} = &\sum_q \sum_i^{N_{\mathrm{dof}}} \varphi(\boldsymbol{x}^e_q, i) \cdot \left(\rho_{\mathrm{s}} \frac{\boldsymbol{v}^n(\boldsymbol{x}^e_q) - \boldsymbol{v}^{n-1}(\boldsymbol{x}^e_q)}{\triangle t} \right) J^e_q w^e_q + \theta \sum_q \nabla \varphi(\boldsymbol{x}^e_q, i) : \boldsymbol{P}^n(\boldsymbol{x}^e_q) J^e_q w^e_q \\ &+ (1-\theta) \sum_q \nabla \varphi(\boldsymbol{x}^e_q, i) : \boldsymbol{P}^{n-1}(\boldsymbol{x}^e_q) J^e_q w^e_q, \end{aligned} \tag{5.4}$$

where J^e_q denotes the mapping (determinant of the Jacobian) from the reference element to element e and w^e_q the quadrature weights for each quadrature point $\boldsymbol{x}^e_q$.

Deal.II is written in a way which makes the assembly of the residual vector very convenient. The algorithm for this assembly is shown in Algorithm 1. For each element (or `cell` in deal.II language) the local residual vector is assembled. This is done by looping over the quadrature points and degrees of freedom of the `cell` and then adding the entries to each velocity degree of freedom that is non–zero at a particular quadrature point. Deal.II always calculates J^e_q and w^e_q together and returns the product of the two `JxW`. The values of the variables at the quadrature points can be calculated in deal.II by using the deal.II object `FEValues` created for the `cell`. The function involved takes the solution vector (values of the solution at the nodal points) as the argument and populates a vector (with the size of the quadrature points in the `cell`) with the values of the variables at the quadrature points. The `FeValues` object contains a function that

Algorithm 1 Assembly of residual

procedure ASSEMBLE_SYSTEM_RHS
  for each element **do**
    for each face on outlet boundary **do**
      for each quadrature point on the face qp **do**
        for each degree of freedom i **do**
          if i is a velocity degree of freedom in the solid domain **then**
            cell_rhs[i]-= $(\rho/\Delta_t(\boldsymbol{v}[qp] - \boldsymbol{v}_{old}[qp])\boldsymbol{\varphi}[i, qp] + \theta(\nabla\boldsymbol{\varphi}[i, qp] : \boldsymbol{P}[qp])$
            $+(1-\theta)(\nabla\boldsymbol{\varphi}[i, qp] : \boldsymbol{P}_{old}[qp]))JxW;$
          end if
        end for
      end for
    end forassemble cell_rhs into global residual vector
  end for
end procedure

can be used to determine the group of variables the degree of freedom is associated with.

5.2 Applying boundary conditions in deal.II

This section elaborates on how the different boundary conditions are applied. When importing the geometry, different boundaries are distinguished by their boundary indicators. The way in which homogeneous and non–homogeneous Dirichlet boundary conditions are applied and distributed is first described. Secondly the implementation of the Windkessel model is described with comments on how a standard Neumann boundary condition would differ from the Windkessel model. Lastly, a few remarks are made about the condition imposed on the displacement of the fluid mesh on the interface.

5.2.1 Dirichlet boundary conditions

There are different ways to implement homogeneous Dirichlet boundary conditions. The boundary degrees of freedom can be eliminated before or after assembly of the vectors and matrices, and before or after distributing the local vectors and matrices into the global ones. It is easier to deal with small, dense local contributions than with global linear systems and it is preferable to assemble each `cell` in exactly the same way. That is why the recommended way of implementing Dirichlet boundary conditions in deal.II is to assemble the local `cell`s first and to eliminate the boundary degrees of freedom at the same time when distributing the local vectors and matrices into the global ones (Algorithm 2).

The homogeneous Dirichlet boundary conditions are conveniently implemented using only a few lines of code. A deal.II `ConstraintMatrix` object is created and populated to include the degrees of freedom on which the zero Dirichlet boundary condition is to be imposed. The function that populates the `ConstraintMatrix` takes as argument the boundary indicator of the boundary on which the condition is to be imposed (`boundary_id`), the function that is to be imposed (`ZeroFunction<dim>(n_components)`), the `ConstraintMatrix` to be populated (`constraints`) and the components of the variables on which it should be imposed upon (`fe.component_mask.component`). After the local vector or matrix of a `cell` is assembled, a function in the `ConstraintMatrix` class is called to distribute the assembled vector or matrix into the global vector or matrix. During this operation the rows of the local vector and the rows and columns of the local matrix associated with the zero boundary condition are changed to contain only zeroes. The same function then fixes the local matrix by replacing the zeros on the diagonal with a value of a similar size to the other entries in the matrix (to ensure that it is not ill–conditioned or under–determined). Lastly this function distributes the changed local vector or matrix into the global matrix.

Algorithm 2 Applying zero Dirichlet boundary conditions

```
Initialize a constraints matrix
procedure MAKE_CONSTRAINTS
    Populate the constraints matrix
end procedure
procedure ASSEMBLE_RHS
    for each element do
        assemble cell_rhs into global vector using the constraints matrix
    end for
end procedure
procedure ASSEMBLE_TANGENT
    for each element do
        assemble cell_tangent into global vector using the constraints matrix
    end for
end procedure
```

The implementation of nonhomogeneous Dirichlet boundary conditions of the linearized equations builds on the implementation of the homogeneous Dirichlet conditions. Note that when the linearized equations are solved, the solution of the equations does not contain the values of the variables, but instead the incremental change in the variables (5.3). The nonhomogeneous Dirichlet boundary conditions are applied in two steps. The first step is to set the variables to the prescribed value (see Algorithm 3). This is done at the beginning of each time step. The second step is to apply homogeneous Dirichlet boundary conditions on the same boundary; in other words prescribing no change to the value that has been set. An example of this is shown in the Step–15 tutorial programme in deal.II.

Algorithm 3 Applying non–zero Dirichlet boundary conditions

```
procedure MAKE_CONSTRAINTS_INITIAL
    Initialize a map that links the degree of freedom and its associated value
    Populate map with values for relevant degrees of freedom
    Use the map to set the solution variables associated with the relevant degrees of freedom
end procedure
```

5.2.2 Implementing the Windkessel model

To implement the Windkessel model discussed in Section 4.1.2 the flow needs to be calculated at the outlet of the fluid domain. The Windkessel value that is calculated from the flow (4.5, 4.9) is applied when the residual vector is assembled in a fashion almost identical to a standard Neumann boundary condition. For this reason the implementation of the standard Neumann boundary condition is not discussed separately.

A `Windkessel` object is created for each outlet. These objects store the values of the Windkessel parameters (R, R_d, C), the flow over the outlet, and calculates and stores the Windkessel value (resulting pressure) at each outlet. After every Newton iteration, the flow and the linearized flow vectors need to be updated and a new value calculated for the pressure. The flow is calculated by integrating the velocity over the outlet area. The contribution to the flow of an element is given by

$$Q^e_{\text{out}}(\boldsymbol{v}^e, \boldsymbol{F}^e) \simeq \sum_q \sum_i^{N_{\text{dof}}} \varphi(\boldsymbol{x}^e_q, i)\boldsymbol{v}(\boldsymbol{x}^e_q) \cdot J(\boldsymbol{x}^e_q)\boldsymbol{F}^{-T}(\boldsymbol{x}^e_q)\boldsymbol{N}(\boldsymbol{x}^e_q) J^e_q w^e_q. \tag{5.5}$$

The calculated scalar value at each quadrature point is then added to the stored value in the `Windkessel` object. When all the contributions have been added to the `Windkessel`

Algorithm 4 Updating the flow and the linearized flow vectors

procedure UPDATE_QPH_INCREMENTAL
  for each element **do**
    for each face on outlet boundary **do**
      for each quadrature point on the face qp **do**
        for each degree of freedom i **do**
          if i is part of velocity degrees of freedom **then**
            windkessel.add_Q($\boldsymbol{v}[qp] \cdot J[qp]\boldsymbol{F}^{-T}[qp]\boldsymbol{N}[qp]N_*[i]$JxW)
            WK_D_v_cell[i] $= (R + \frac{e^{-\frac{\triangle t_n}{2\tau}}(\triangle t)}{2C_{\text{out}}})J[qp]\boldsymbol{F}^{-T}[qp]\boldsymbol{N}[qp] \cdot \boldsymbol{\phi}^{\boldsymbol{v}}[i]$JxW
          end if
          if i is part of displacement degrees of freedom **then**
            WK_D_u_cell[i] $= (R + \frac{e^{-\frac{\triangle t_n}{2\tau}}(\triangle t)}{2C_{\text{out}}})[(D\_u\_J[qp][j]\boldsymbol{F}^{-T}[qp]\boldsymbol{N}[qp]) \cdot \boldsymbol{v}N_*[i])$
            $+(J[qp]D_u_\boldsymbol{F}^{-T}[qp][j]\boldsymbol{N}[qp]) \cdot \boldsymbol{v}N_*[i]]$JxW
          end if
        end for
      end for
    end for
    assemble lcoal WK_D_v_cell and WK_D_u_cell into global Dv and Du
  end for
windkessel.calculate_p_wk(Q)
end procedure

object, the pressure value is updated. This is the pressure value that is enforced on the outlet boundary. Next, the pressure term is added to the velocity degrees of freedom of the residual vector in the same way that a standard Neumann boundary condition would be added (Algorithm 5).

Algorithm 5 Assembling the Windkessel contribution to the residual

procedure ASSEMBLE_RHS
  for each element **do**
    for each face on outlet boundary **do**
      for each quadrature point on the face qp **do**
        for each degree of freedom i **do**
          if i is a velocity degree of freedom in the fluid domain **then**
            cell_$rhs[i] -= J[qp]\boldsymbol{F}^{-T}[qp]\boldsymbol{N}[qp] \cdot \boldsymbol{\phi}^{\boldsymbol{v}}[i, qp]\mathrm{p}_{WK}$JxW
          end if
        end for
      end for
    end for
    assemble cell_rhs into global residual vector
  end for
end procedure

The vectors that store the values of the second integral of the linearized equations are also updated after every Newton iteration. These vectors have the same structure as the solution vector and are assembled in a way similar to the residual vector. The contributions to these vectors from each element are:

$$\mathtt{Dv} = \sum_q \sum_i^{N_{\text{dof}}} \varphi(\boldsymbol{x}_q^e, i) \cdot J(\boldsymbol{x}_q^e)\boldsymbol{F}^{-T}(\boldsymbol{x}_q^e)\boldsymbol{N}(\boldsymbol{x}_q^e)J_q^e W_q^e, \tag{5.6}$$

(from 4.7) and

$$
\begin{aligned}
\mathtt{Du} = \sum_q \sum_i^{N_{\mathrm{dof}}} \boldsymbol{v}(\boldsymbol{x}_q^e) \cdot D_{\Delta u} J(\boldsymbol{x}_q^e) \boldsymbol{F}^{-T}(\boldsymbol{x}_q^e) \\
+ J(\boldsymbol{x}_q^e) D_{\Delta u} \boldsymbol{F}^{-T}(\boldsymbol{x}_q^e) \boldsymbol{N}(\boldsymbol{x}_q^e) * J_q^e W_q^e,
\end{aligned}
\tag{5.7}
$$

from (4.15).

The local vectors are updated after every Newton iteration and assembled into the global vectors `Dv` and `Du`. These global vectors contain mostly zeroes, with the exception of the entries associated with the velocity on the outlet boundaries. The ith entry of the global vector `Dv` thus contains the contributions from all the quadrature points surrounding the node associated with the ith degree of freedom.

With these precomputed integral vectors, the tangent can be assembled similarly to the residual, but with an extra loop over the degrees of freedom.

Algorithm 6 Assembling the Windkessel contribution to the tangent

procedure ASSEMBLE_TANGENT
  for each element **do**
    for each face on outlet boundary **do**
      for each quadrature point on the face qp **do**
        for each degree of freedom i **do**
          for each degree of freedom j **do**
            if i is part of v_fe **then**
              cell_$tangent[i,j] -= J[qp]\boldsymbol{F}^{-T}[qp]\boldsymbol{N}[qp] \cdot \boldsymbol{\phi}^{\boldsymbol{v}}[i]$WK_D_v[j]JxW
            end if
            if i is part of u_fe **then**
              cell_$tangent[i,j] += [(J[qp]\boldsymbol{F}^{-T}[qp]\boldsymbol{N}[qp] \cdot \boldsymbol{\phi}^{\boldsymbol{v}}[i])$WK_D_u[j]
              +(D_u_J[qp][j]$\boldsymbol{F}^{-T}$[qp]$\boldsymbol{N}$[qp]+$J[qp]$D_u_$\boldsymbol{F}^{-T}$[qp][j]$\boldsymbol{N}[qp]) \cdot \boldsymbol{\phi}^{\boldsymbol{v}}$[i]$\mathrm{P}_{WK}$]JxW
            end if
          end for
        end for
      end for
    end for
    assemble cell_tangent into global tangent matrix
  end for
end procedure

5.2.3 Dirichlet condition of mesh on interface

To implement the interface condition of the mesh $(3.25)_{\mathrm{a}}$, a different approach needs to be followed than the one discussed in Section 5.2.1. The total contribution to the residual and tangent matrix are not zero; only the contributions from the fluid domain Ω_{f} that are associated with the displacement degrees of freedom are zero. The first step in implementing the interface condition is to create a vector with size N_{dof} and to flag all the degrees of freedom that are associated with displacements and that are on the interface Γ_{i}. This vector is used when assembling the residual vector and tangent matrix to determine which degrees of freedom are associated with the interface condition. The second step is to add only the contributions from the fluid equations that are not associated with the interface condition to the residual vector and tangent matrix.

5.3 Parallelization

Solving the linear equations on a patient–specific mesh introduces some computational challenges. To achieve mesh independence and to be certain that the flow at the boundaries is resolved, a fine mesh is necessary. This results in a large system of equations that needs to be assembled and solved. The following section gives attention to the concepts of shared memory and distributed memory parallelization. It looks at the software and data structures that are necessary for the code to run on multiple processors or machines.

5.3.1 Shared memory and distributed memory

There are two basic strategies that can be used to run a code in parallel: shared memory and distributed memory. If only one machine is available a shared memory approach is beneficial. In this approach the complete mesh, residual and solution vector and tangent matrix are stored in one part of the memory (Fig. 5.2 a)). Different processors carry out operations simultaneously. To assemble the residual vector and tangent matrix, the Threaded Building Blocks library is used [80]. In deal.II the `WorkStream` class uses Threaded Building Blocks to assemble each `cell`. A scheduler is used to indicate that it has available resources, at which point another local vector or matrix is sent to be assembled. The `Workstream` class ensures that only one local vector or matrix is assembled into the global vector or matrix at a time to avoid a race condition, so that no contribution is lost.

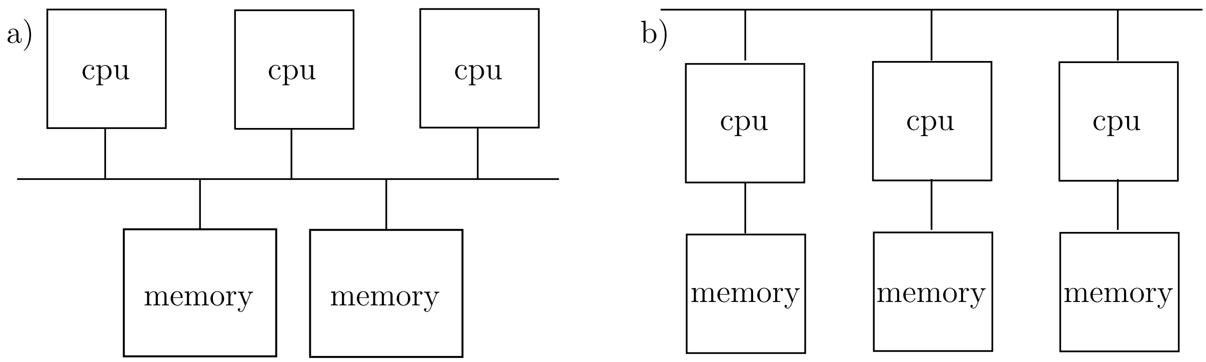

Fig. 5.2: Layout of parallel programs using a) shared memory and b) distributed memory .

The distributed memory approach for parallelization is designed for computations on multiple machines but can also be used on one machine with multiple processors. Each processor owns a part of memory (Fig. 5.2 b)). The network employs Message Passing Interface (MPI) to pass messages and data between processors. Each processor owns a part of the mesh and the associated parts of the residual and solution vector and tangent matrix.

Deal.II employs the software library p4est [7] to enable the dynamic distribution and management of the mesh on many processors (Fig. 5.3). The mesh is distributed so that each processor owns some `cell`s of the mesh (locally owned `cell`s) as well as a layer of ghost `cell`s around the locally owned `cell`s (locally relevant `cell`s).

The residual and solution vectors and the tangent matrix are also distributed between the processors. The processor can only write into entries of the data structures that are associated with the locally owned `cell`s, but can read data from the locally relevant `cell`s. In other words, each processor assembles the local `cell`s which it owns and distributes it to the part of the global data structure that it owns. After the global data structure has been assembled on each processor, it is compressed so that the relevant information (associated with the ghost `cell`s) is passed to other processors.

We made use of the distributed memory approach so that the code can be run on a single machine but can also scale to a distributed cluster environment.

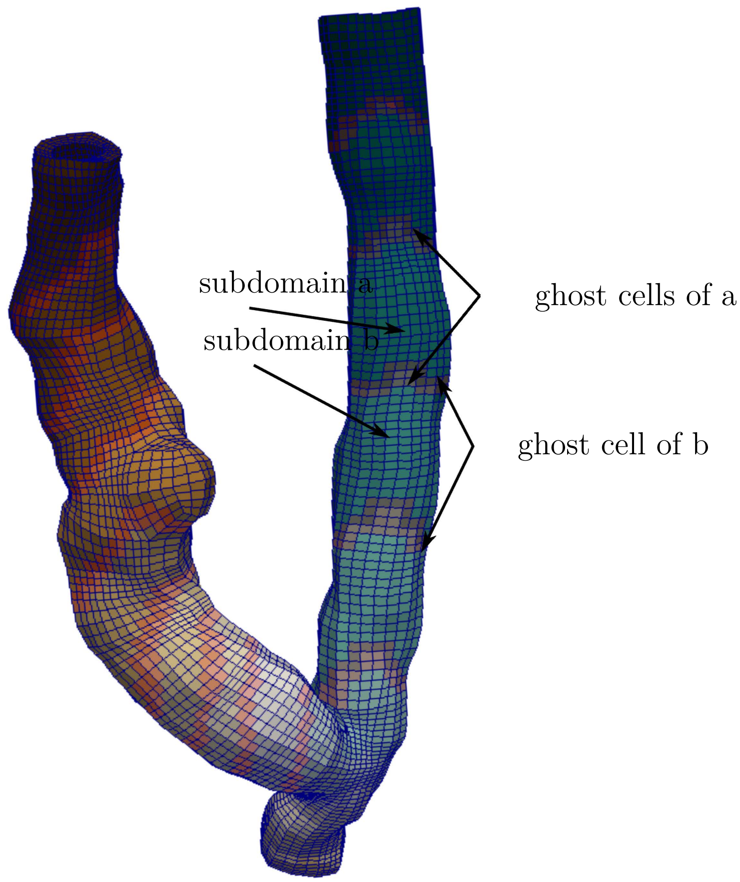

Fig. 5.3: Subdomains containing locally owned `cells` and the surrounding ghost `cells`.

5.3.2 Solving the system of linear equations

Solving the system of equations (5.3) for a problem with many elements is not straightforward. The system matrix is neither symmetric nor positive–definite. High condition numbers may be expected which will lead to slow convergence when using iterative solvers such as the generalized minimal residual method (GMRES) without a suitable preconditioner. Large systems of equations can not be solved with a direct solver that uses only one processor.

The best approach to improve the convergence rate of iterative solvers would be to make use of a suitable preconditioner. A Block–Schur preconditioner or geometric multigrid preconditioner may be adapted for this problem. There are several suggestions for algorithms to solve fluid–structure interaction equations available in the literature (see for example [46]). As the emphasis of this study is on the application of the model, the implementation of a suitable pre–conditioner is left as a future challenge.

The approach followed was to implement a parallel direct solver. Deal.II wraps the preconditioners and solvers from Trilinos [47]. The Trilinos project is a group of packages that contains algorithms for the solution of large–scale, complex multi–physics engineering problems. The parallel direct solver that has been wrapped into deal.II is called superLU [67].

5.4 Chapter summary

In this chapter attention was given to the implementation of the model using deal.II. Pseudo–code was used to illustrate some of the interesting parts of the computer implementation. The software and data structures necessary to enable the parallelization of the code were discussed. Lastly the available solvers were discussed.

The next chapter presents results from benchmark tests and patient–specific simulations.

6

Results and analysis

The theory and finite element implementation developed in the previous chapters are now applied to a series of benchmark problems. The verified code is then used to validate the model by comparing flow results from the FSI simulations to actual patient data obtained by MRI.

6.1 Verification of code

Every part of the finite element code is verified separately by simulating a suitable benchmark problem from the literature. The benchmark problems cover the fibre–reinforced materials, Navier–Stokes equations, FSI and the Windkessel model.

6.1.1 Fibre–reinforced material

The benchmark problem chosen to verify the material model for the vessels consists of uni–axial tensile tests conducted on circumferential and axial specimens of a dissected vessel [41]. The transverse isotoropic hyperelastic material model employed here was discussed in Section 3.3.1.

The simulations were carried out on specimens resembling strips cut from the adventitious layer of a vessel. Strips with length $L = 10\,\text{mm}$, width $W = 3.0\,\text{mm}$ and thickness $T = 0.5\,\text{mm}$ were considered. The angle of the collagen fibre as defined in Fig. 4.6 was set to $\beta = 49.98°$. Both axial and circumferential specimens were considered. Material parameters are: $c = 7.64\,\text{kPa}$, $k_1 = 996.6\,\text{kPa}$ and $k_2 = 524.6$. To investigate the effect of the dispersion of the collagen on displacement and stress, values of $\kappa = 0$ and $\kappa = 0.226$ were considered.

A uni–axial tensile load is applied and the end faces of the specimens prevented from deforming.

Q_2^c/P_1^{dc} (see Fig. 5.1) elements are used along with the two–field formulation described in Sections 3.47 and 3.48. In [41] a mixed displacement–pressure formulation using Q_1^c/P_0^{dc} elements was adopted in conjunction with an augmented Lagrangian method and an Uzawa algorithm. The mesh in the present study was constructed in such a way that the number of degrees of freedom was approximately the same as that in the study in [41]. The mesh consisted of 400 Q_2^c/P_1^{dc} hexahedral elements compared to 3200 Q_1^c/P_0^{dc} hexahedral elements used in [41].

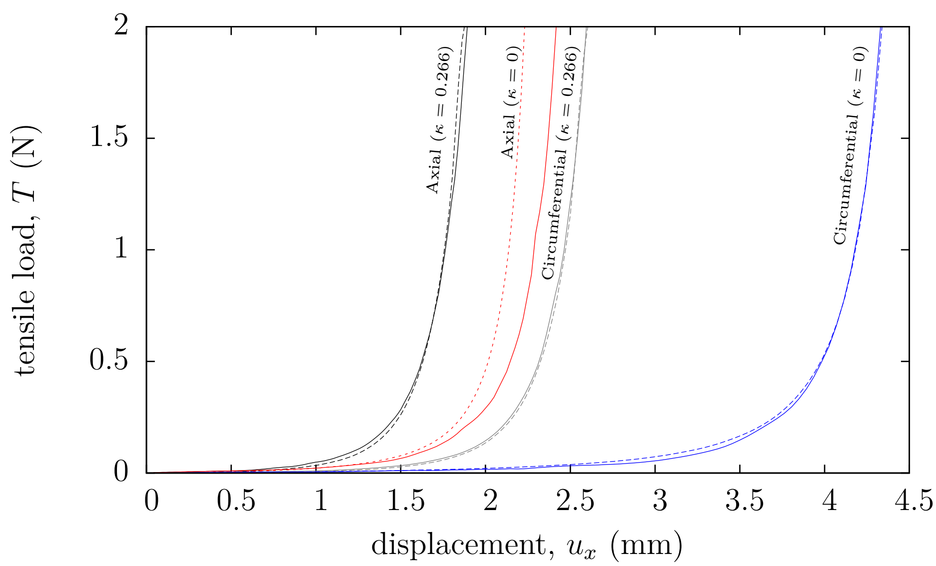

Fig. 6.1: Comparison of tensile load/displacement response of different specimens showing the influence of the collagen fibre and the mean alignment β. The solid curves are from [41] and the dashed lines represent our results.

The response of the material is illustrated in Fig. 6.1. Initially the material is flexible and a small force T causes a large extension in the direction of loading. When the collagen fibres are approximately aligned with the tensile direction the material stiffens significantly. The results generally correlate well with those found in [41]. There is however a difference for the axial strip when $\kappa = 0$.

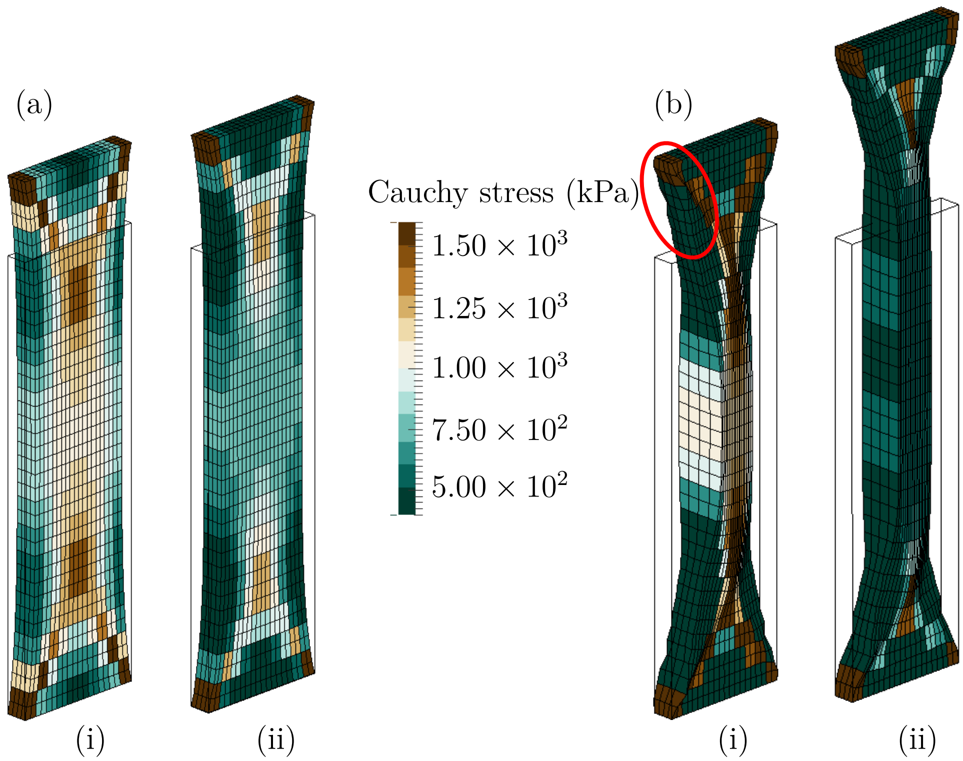

Fig. 6.2: Cauchy stress in the direction of the applied load when a tensile load of $1N$ is applied. Results (a) for $\kappa = 0.226$ and (b) for $\kappa = 0$ are shown for specimens in the (i) axial and (ii) circumferential directions.

The Cauchy stress in the strips for the case in which $T = 1\,N$ are shown in Fig. 6.2. These results also correlate well with the benchmark. When $\kappa = 0$ the strip thickens in the middle as a result of the collagen having to align with the loading direction in order to sustain load. When $\kappa = 0$ for the axial strip in Fig. 6.2 (b)(i), hourglassing can be seen at the corners of the specimen in the region where the stress is high. Hourglassing is a spurious deformation mode of a finite element mesh that manifests as a patchwork of zig–zag or hourglass like element shapes, where elements are severely deformed, while the overall mesh section is undeformed.

The premature stiffening of the specimen seen in Fig. 6.1 points to locking of the axial strip. The locking arises from the use of the two–field formulation without paying special consideration to the combination of the incompressibility and the absence of dispersion of the fibres.

To circumvent locking, the incompressibility constraint can be relaxed by regularization procedures such as the perturbed Lagrange–multiplier method. The perturbed Lagrange–multiplier method can be considered as a two–field principle in which the potential functional is perturbed by a penalty term. Thus the internal potential functional (3.45) is replaced by

$$\Pi_{\text{int}}(\boldsymbol{u}, p) = \int_{\Omega_0} \left[p \left(J \left(\boldsymbol{u} \right) - 1 \right) + \Psi_{\text{iso}}(\bar{\boldsymbol{C}}(\boldsymbol{u})) \right] \mathrm{dV} - \frac{1}{2} \int_{\Omega_0} \frac{1}{\zeta} p^2 \mathrm{dV} \tag{6.1}$$

where $\zeta > 0$ is the penalty parameter. The weak form remains mainly unaltered except that (3.60) is replaced by

$$\int_{\Omega_\text{s}} \phi^p \left(J - 1 - \frac{p}{\zeta} \right) \mathrm{dV} = 0. \tag{6.2}$$

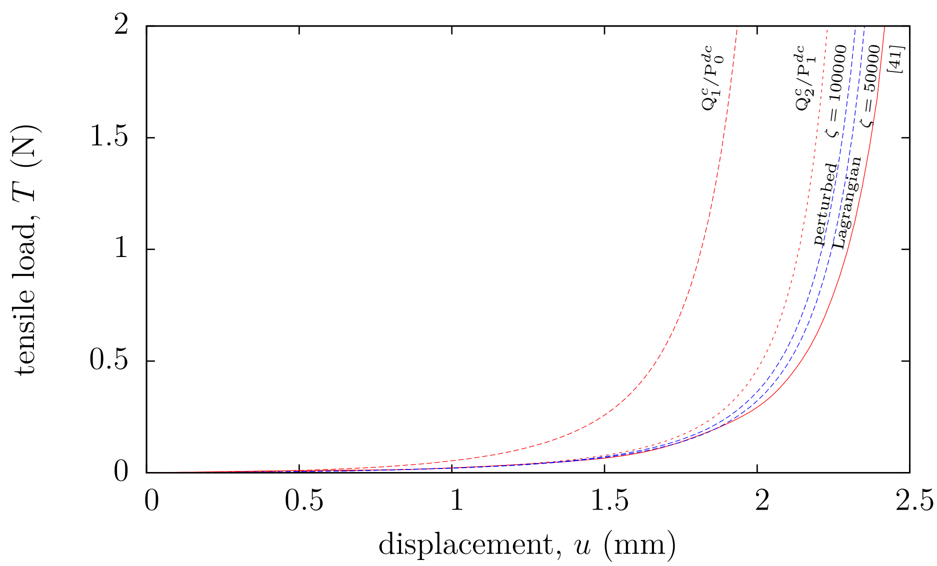

Fig. 6.3: The load–displacement response of the axial strip for $\kappa = 0$. The solid line represents the results from the literature, the red dashed line shows the results from the Lagrange–multiplier method and the blue lines show the results from the perturbed Lagrange–multiplier method with $\zeta = 100\,000$ and $\zeta = 50\,000$.

In Fig. 6.3 the results from the perturbed Lagrange–multiplier method are compared to those from the Lagrange–multiplier method using Q_1^c/P_0^{dc} and Q_2^c/P_1^{dc} and results from [41]. As ζ decreases, the incompressibility constraint is relaxed, the locking decreases and the displacement approaches the displacement in [41]. The model used is highly nonlinear and the Newton solver does not achieve a quadratic convergence rate, but a convergence rate slightly better than linear convergence can be observed.

For the patient–specific simulations the dispersion will be set to $\kappa = 0.266$.

6.1.2 Flow around a flag

The implementation of the Navier–Stokes equations and fluid–structure interaction was verified against the 2D "Turek–flag" benchmark tests [94]. The simulation consists of a flexible flag attached to a rigid cylinder immersed in fluid (Fig. 6.4). The centre of the cylinder is positioned at $B = (0.2, 0.2)$. The flag is modelled as a St. Venant–Kirchhoff material, for which the second Piola-Kirchoff stress is given by

$$\boldsymbol{S} = \lambda \mathrm{tr}(\boldsymbol{E})\boldsymbol{I} + 2\mu\boldsymbol{E}. \tag{6.3}$$

The Navier–Stokes equations are first verified when the flag is rigid, and thereafter the FSI is verified when the flag is flexible. Comparisons are made of the mean values, amplitude and frequency of the displacement at point $A = (0.6, 0.2)$ and the drag and lift forces around the cylinder and beam. The drag and lift forces are calculated as $(F_D, F_L) = \int_S \boldsymbol{\sigma}\boldsymbol{n}\mathrm{dS}$. The mean values of the displacement and forces are calculated as the average of the min/max values of the last oscillation, and the amplitude is the difference of the min/max from the mean.

Newtonian flow

For the fluid tests, the solid was rigid. The density and viscosity of the fluid were set to $\rho_f = 1 \times 10^3\,\mathrm{kg/m^3}$ and $\nu_\mathrm{f} = 1 \times 10^{-3}\,\mathrm{m^2/s}$. A parabolic profile was prescribed for the velocity at the inlet and characterized by the mean velocity $\bar{\boldsymbol{v}}$. No–slip conditions

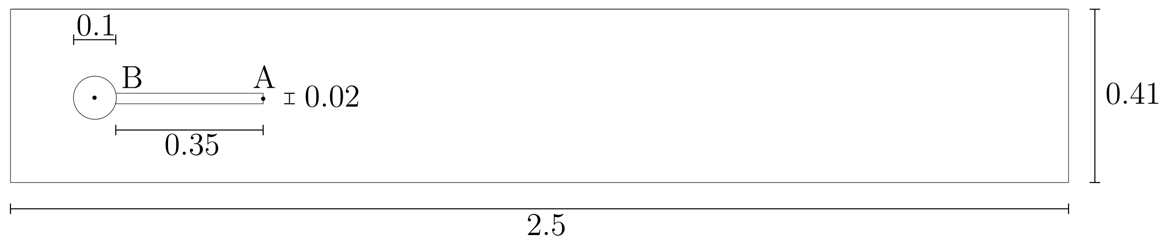

Fig. 6.4: The Turek flag.

were prescribed at the top and bottom boundaries of the fluid domain and zero mean pressure at the outlet.

Table 6.1: Summary of results for CFD1, CFD2 and CFD3

	$\bar{\boldsymbol{v}}$(m/s)	drag (N) ± amplitude [frequency]	lift (N) ± amplitude [frequency]
CFD1 [94]	0.2	14.29	1.119
CFD1		14.151	1.12029
CFD2 [94]	1	136.7	10.53
CFD2		129.186	10.77
CFD3 [94]	2	439.45 ± 5.6183 [4.3956]	-11.893 ± 437.81 [4.3956]
CFD3		391.46 ± 4.1995 [4.4209]	-10.474 ± 356.576 [4.4209]

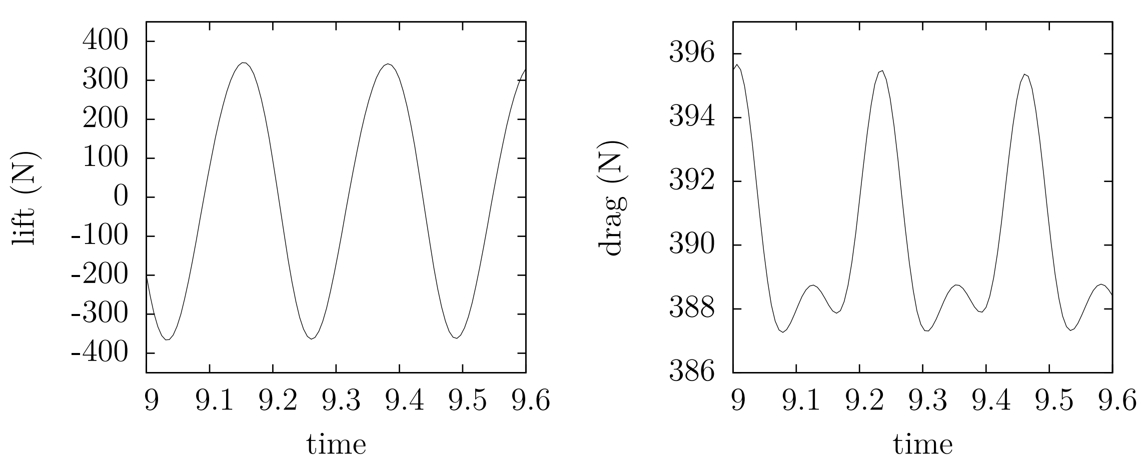

Fig. 6.5: Lift and drag forces on the cylinder and flag (CFD3).

The nomenclature for the different test cases in [94] is adopted here. CFD1 and CFD2 are steady–state fluid flow test cases with different values for the inlet velocity. CFD3 is a time–dependent fluid flow test case. Results for steady–state simulations CFD1 and CFD2 and time–dependent simulation CFD3 are shown in Table 6.1. For time–dependent problems mean values are followed by the amplitude and the frequencies are shown in brackets.

Results for the two steady state cases (CFD1 and CFD2) correspond well to the results found in literature. The results for CFD3 shown in Fig. 6.5 shows good qualitative agreement with the benchmark test. While the frequencies of the lift and drag forces correspond well, there is a significant difference in the mean values and amplitude of the lift and drag forces. The errors are all below 25 %, which is in the range observed in [95] when different solution methods are used. These differences can be ascribed to different techniques used with regards to discretization, solver and coupling mechanisms.

Fluid–structure interaction

The same arrangement that was used to verify the implementation of the Navier–Stokes equation was adopted to verify the implementation of the fluid–structure interaction. This time the flag is flexible. Results for a fluid–structure interaction test case (FSI3) [94] were compared to those using different solution methods [95].

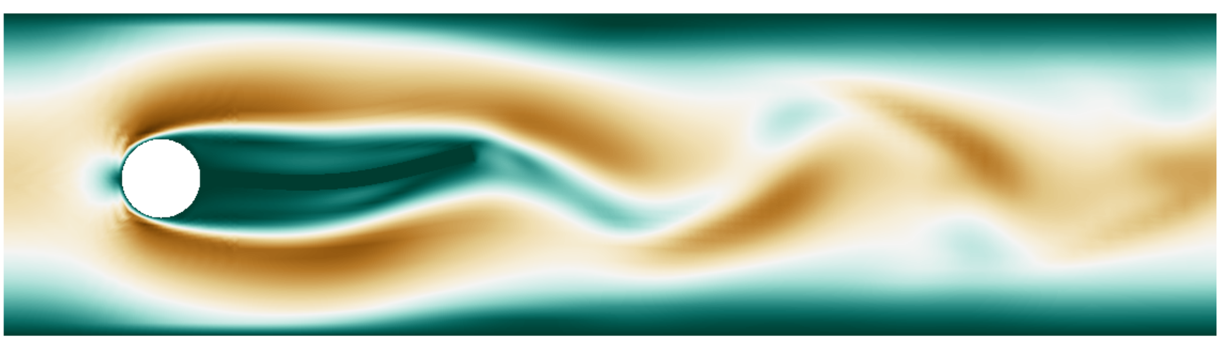

Fig. 6.6: The flow around the flag at $t = 9.072\,\mathrm{s}$.

The material parameters were set to $\rho_\mathrm{s} = 1000\,\mathrm{kg/m^3}$, $\nu_\mathrm{s} = 0.4$, $\mu_\mathrm{s} = 2 \times 10^6\,\mathrm{kg/ms^2}$, $\rho_\mathrm{f} = 1000\,\mathrm{kg/m^3}$, $\nu_\mathrm{f} = 1 \times 10^{-3}\,\mathrm{m^2/s}$ and $\bar{\boldsymbol{v}} = 0.2\,\mathrm{m/s}$. The harmonic mesh motion parameter was set as $\alpha = \frac{(J-1)^2}{D_\mathrm{cell}}$ where D_cell is the diameter of the cell.

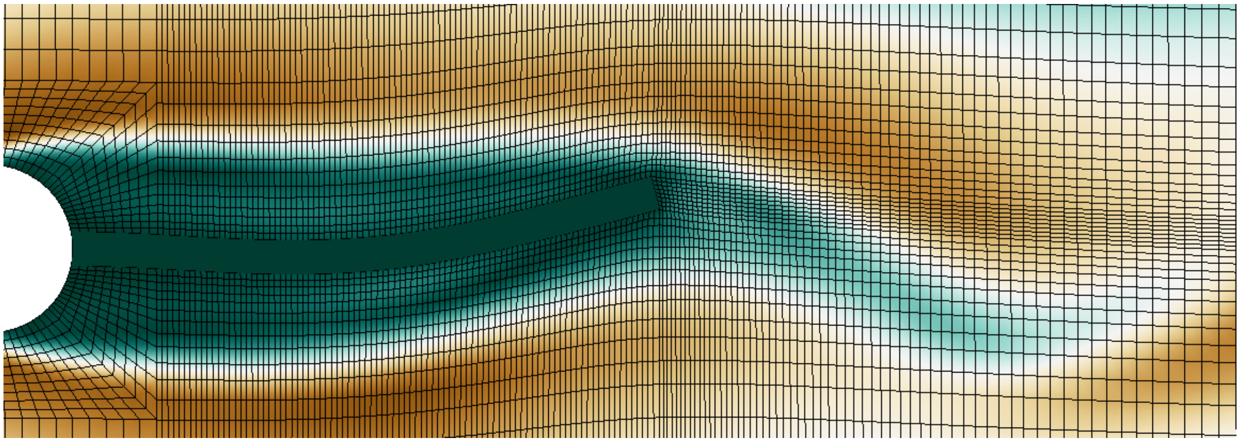

Fig. 6.7: The mesh at $t = 9072\,\mathrm{s}$.

After some time, the flag oscillates and vortex shedding occurs (Fig. 6.6). The motion of the mesh can be seen in Fig. 6.7. The bigger cells of the mesh closest to the edge of the boundary deform more than the small cells closer to the flag. When a cell deforms, the value of $(J-1)^2$ of that cell increases and α from (3.26) increases to prevent further distortion.

Table 6.2: Summary of results for FSI3

	u_x of A[$\times 10^{-3}$]	u_y of A[$\times 10^{-3}$]	drag	lift
FSI3 [94]	-2.69 ± 2.53 [10.9]	1.48 ± 34.58 [5.3]	457 ± 22.66 [10.9]	2.22 ± 149.78 [5.3]
FSI3	-2.41 ± 2.28[10.75]	1.42 ± 31.61 [5.4]	392.30 ± 23.42 [10.75]	0.481 ± 172.122 [5.4]

Table 6.2 shows a summary of the results. The oscillations of point A correlate well with the benchmark results (Fig. 6.8). The oscillations of the lift and drag forces have a good qualitative agreement with the benchmark results (Fig. 6.9). Though a significant difference can be seen in the mean and amplitude values of the drag and

lift forces, it is still within the order of 50% that was observed in [95] between different solution methods.

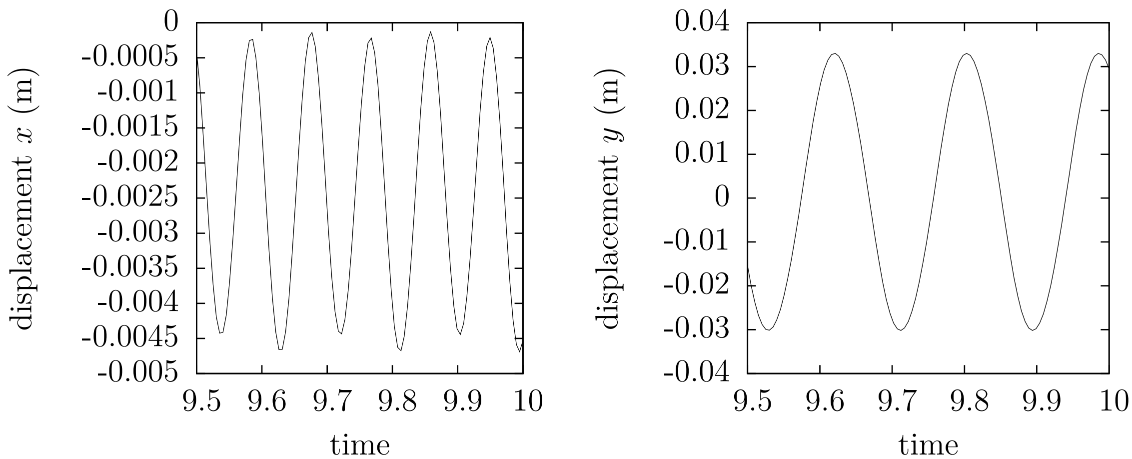

Fig. 6.8: x and y displacement of the point A (FSI3).

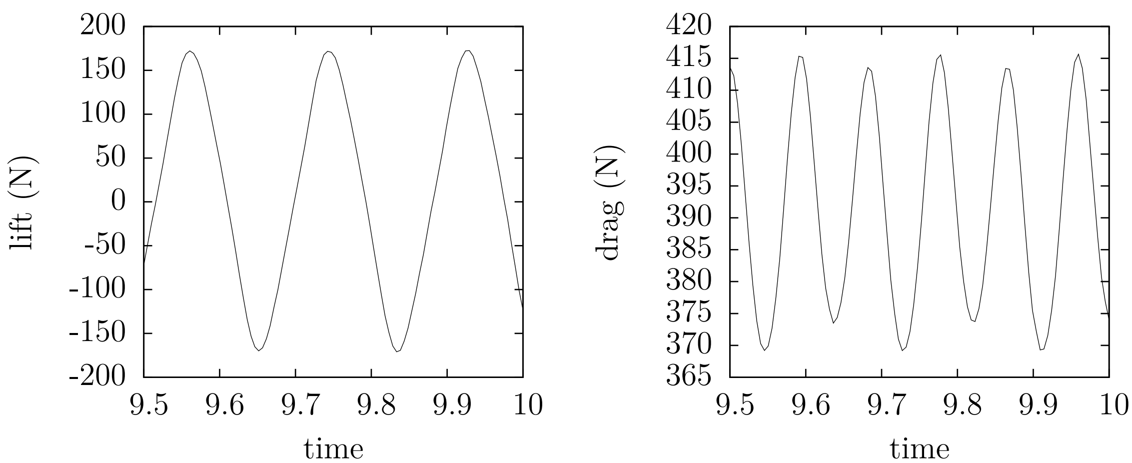

Fig. 6.9: Lift and drag forces on the cylinder and flag (FSI3).

6.1.3 Windkessel outlet

The implementation of the outlet boundary conditions described in section 4.1.2 is verified against a problem taken from [97]. There are slight differences in the setup of the simulation: for example, a Neo–Hookean material is used here instead of the linear elastic enhanced thin–membrane model.

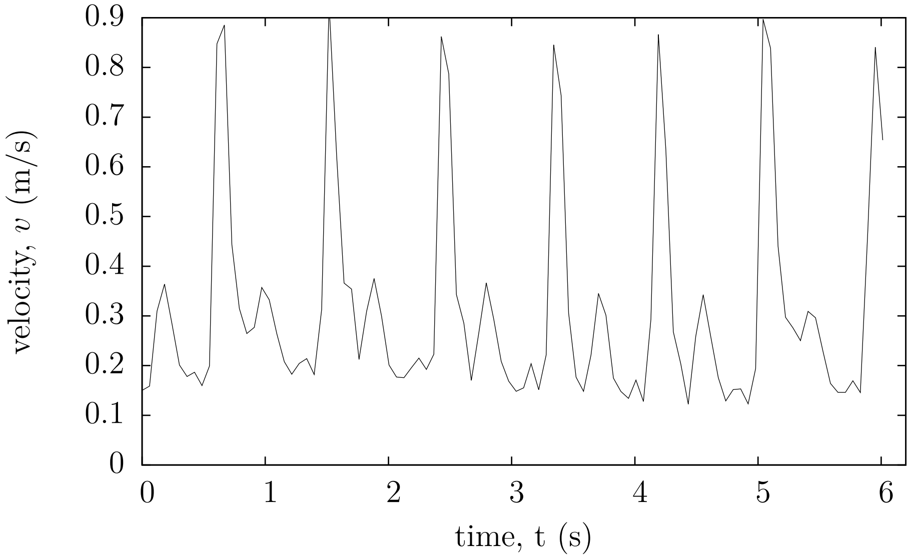

Fig. 6.10: Mean velocity at inlet taken from Doppler measurements [97].

Pulsatifle flow through a straight cylindrical vessel with cross–sectional area $2.4 \times 10^{-5}\,\mathrm{m}^2$, length $3.5 \times 10^{-2}\,\mathrm{m}$ and thickness 9.0×10^{-4} m is simulated. The vessel wall is modelled by an incompressible neo–Hookean material with shear modulus $\mu = 1.36 \times 10^5$ Pa and density $\rho_s = 1000\,\mathrm{kg/m^3}$. A Newtonian approximation is assumed for the blood with kinematic viscosity $\nu = 4.0 \times 10^{-6}\,\mathrm{m^2 s^{-1}}$ and density $\rho_f = 1006\,\mathrm{kg/m^3}$. A time–varying mean velocity taken from Doppler–measurements was prescribed at the inlet (Fig. 6.10).

The values for resistance, downstream resistance and capacitance were set as $R = 1.1171 \times 10^8\,(\mathrm{Pa\,s})/\mathrm{m}^3$, $R_d = 1.21441 \times 10^9\,(\mathrm{Pa\,s})/\mathrm{m}^3$ and $C = 3.18 \times 10^{-10}\,\mathrm{m}^3/(\mathrm{Pa\,s})$ respectively.

To verify the pressure calculation, a zero–dimensional test is carried out by taking flow values from [97] over time and calculating the resulting pressure using the Windkessel–model. This was done over two cycles consisting of 7 cardiac cycles. From the results in Fig. 6.11 it can be seen that the pressure waves converge to the same solution after the first cycle. The behaviour of the pressure waves corresponds well with those found in [97].

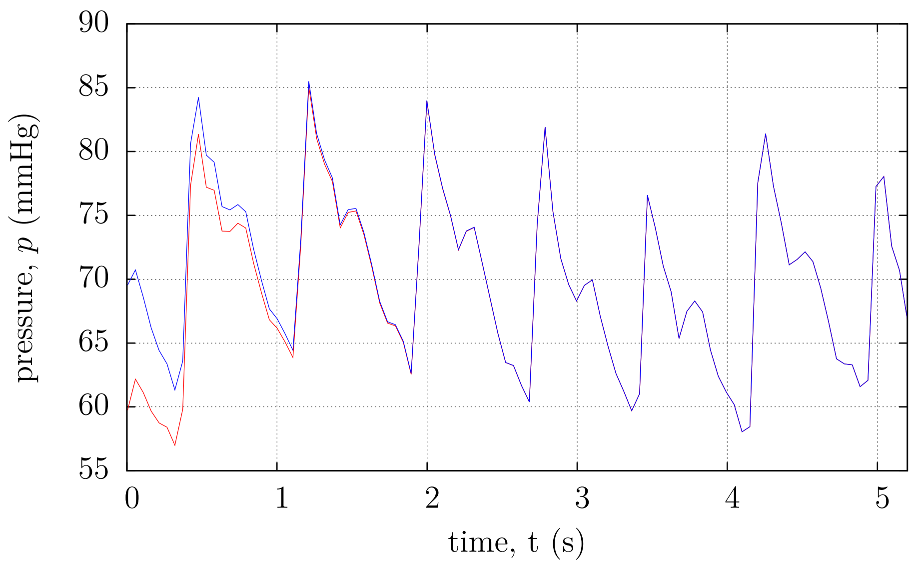

Fig. 6.11: Pressure at the outlet for two repititions of seven cardiac cycles. The first cycle is shown in red and second in blue.

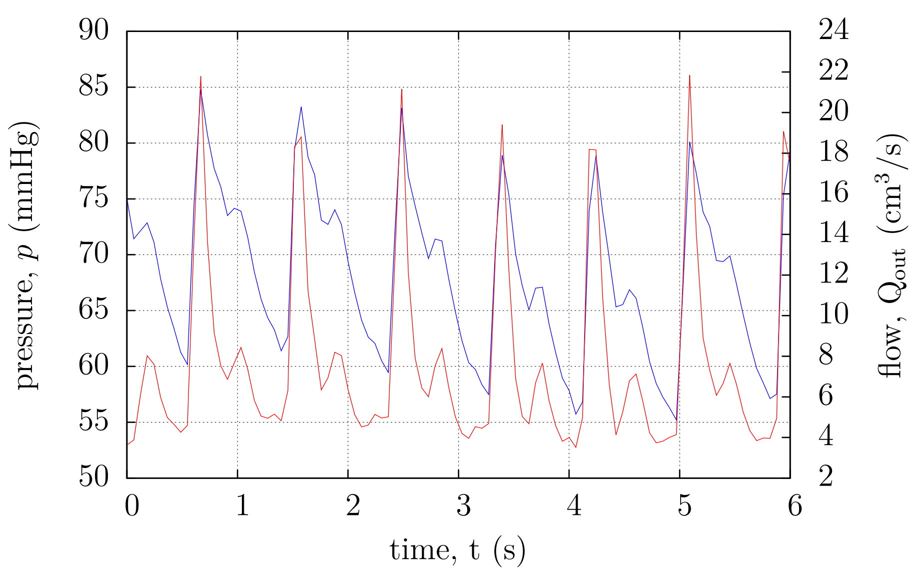

Fig. 6.12: Non–periodic flow (red) and pressure (blue) at the outlet of an idealized vessel.

To verify the implementation of the FSI combined with the Windkessel–model a simulation was run prescribing the flow using the data from Fig. 6.10. A parabolic velocity profile was prescribed at the inlet. Results for Q_{out} and p are shown in Fig. 6.12. Here it can be seen that the pressure waves lag the flow waves. The behaviour of both the flow and pressure waves corresponds well with those found in [97].

6.2 Patient–specific simulations

This section focuses on the results of the patient–specific FSI simulations of an arteriovenous fistula.

The set–up of the simulation includes the treatment of boundary conditions not discussed in Chapter 4 as well as the calibration of certain parameters. The implementation and outcome of individual features of the model such as fibre directions, pre–stress and back flow stabilization are presented here. The influence of the numerical damping and time discretization scheme on the results are investigated.

Lastly the flow patterns of the simulations are compared against those processed from the 4D MRI. This will serve as verification of the model. The stresses experienced in the structure, wall shear stress, oscillatory wall shear stress and reflection of pressure waves are analysed.

6.2.1 Setup and calibration of simulation

The geometry used for the patient–specific fistula is acquired from MRI and processed as described in section 4.2. The mesh imported into deal.II contains information that identifies the different materials for each hexahedral element using a material number. Different boundaries can also be identified by a boundary number. Fig. 6.13 shows regions of different materials.

The blood is described by its density $\rho_{\mathrm{f}} = 1060\,\mathrm{kg/m^3}$ and viscosity $\nu = 4.0\times10^{-6}\,\mathrm{m^2/s}$. The fibre–reinforced vessel as defined by the free–energy (3.49) is described by its

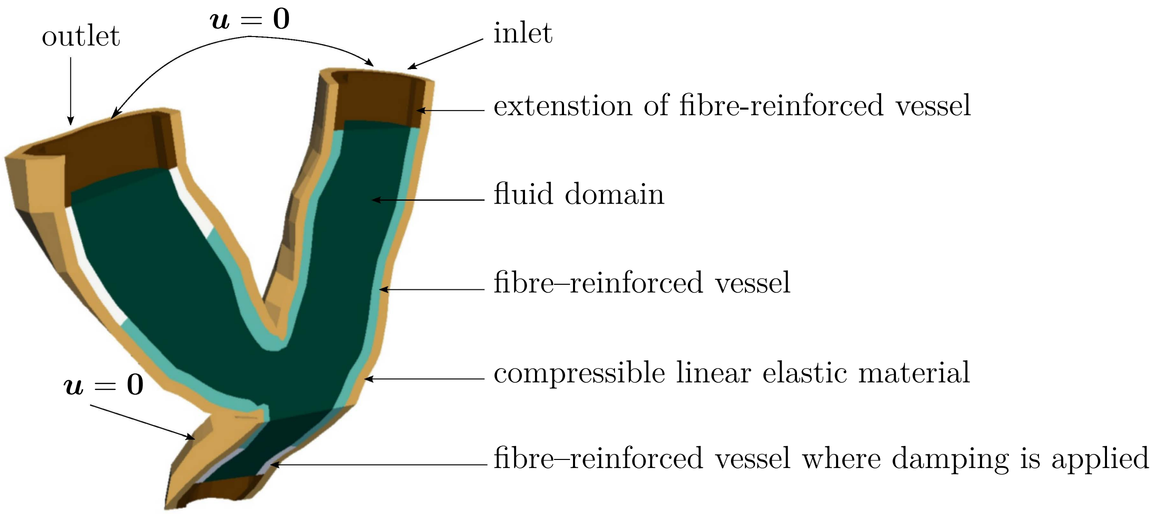

Fig. 6.13: A highly compressible linear–elastic material surrounds the vessel. The fibre–reinforced vessel is extended to allow displacement at the inlet and outlets. These extensions are fixed at the ends.

density $\rho_s = 1000\,\mathrm{kg/m^3}$, Lamé's first parameter $\lambda = 38200$ Pa, the first and second fibre constants $k_1 = 199320$ Pa and $k_2 = 108.4$, the local fibre direction $\beta = 49.98^o$ and the dispersion parameter $\kappa = 0.226$. These values are all physically realistic. Fig. 6.14 shows the change in area when applying a pressure on the inside of a vessel. The experimental data shown have been measured with the smooth muscle of the brachial arterial wall relaxed with nitroglycerin [9, 84] and from in vitro experiments performed on porcine carotid arteries [59]. The fibre–reinforced material where damping is applied is defined by the same parameters and values with the added strong and weak damping coefficients set as $\gamma_s = 1.34 \times 10^4$ and $\gamma_w = 1.34 \times 10^3$ respectively (see section 4.1.3).

The fibre–reinforced vessel is extended beyond the fluid domain at the inlet and outlets. The ends of these extensions are fixed in space. The reasoning behind these extensions is that it allows displacement in both the radial and axial directions at the inlets and outlets.

The vessel is surrounded by a compressible linear elastic material that represents the soft tissue. This provides some resistance against bending of the domain. The material is defined by Lamé's first parameter $\lambda = 38200$ Pa and Poisson's ratio $\nu_s = 0$. There is no added stiffness from fibres. The boundary on the outside of the linear elastic

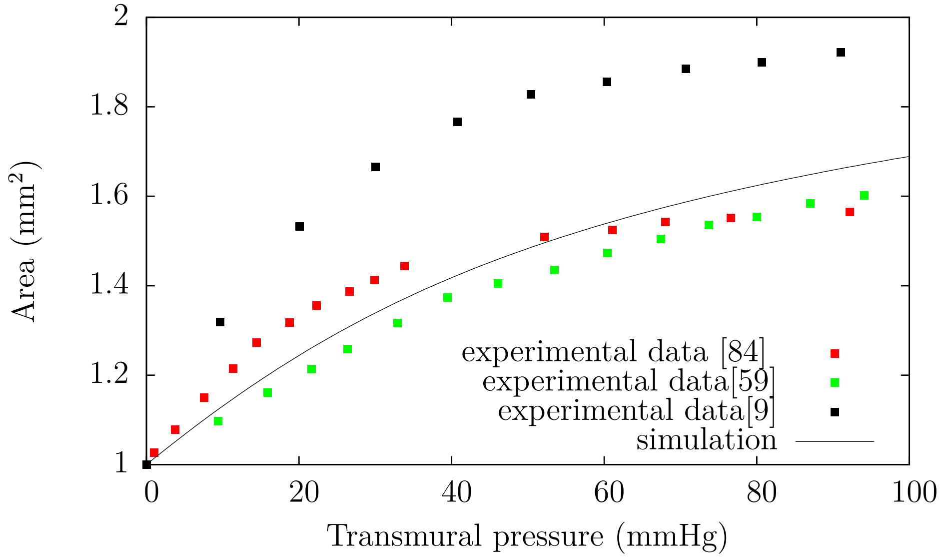

Fig. 6.14: Material parameters [59],[84].

material is fixed.

The Windkessel values are found by fitting the flow division to that found in the MRI data, and pressures to those found in the literature. The flow data from the MRI contain some inaccuracies; the spatial resolution prevents one from determining exactly where the boundary of the vessel is. The area and consequently the flow calculated from the images thus contains some error. The resolution of the velocity data from the MRI depend on the velocity encoding (VENC) setting. This setting reflects the maximum velocity expected. For example, if the VENC setting is 150, velocities of $\pm$ 150 cm/s can be captured accurately. The higher the VENC setting, the more difficult it is to capture small velocity differences. If however the VENC settings are not high enough to capture the velocity, wrapping occurs and incorrect values are assigned to the velocity values that fall outside the acceptable range. For example if the VENC setting is 150 and the velocity measured is 160 cm/s, the velocity is recorded as -140 cm/s. Flow at the boundaries is slow and therefore difficult to capture, adding to greater inaccuracy in the flow calculations. For small arteries and veins such as the brachial artery and cephalic vein, these inaccuracies can be significant.

Table 6.3 summarises the VENC settings and the measured velocities. The third column shows the maximum value over time of the mean velocity over the slice. The fourth column shows the mean value over time of the mean velocity over the slice. When integrating over time the flow measured over a cardiac cycle at the inlet and outlets is non–conservative. This highlights the inaccuracies present in the data. The data is however still useful as it gives an idea of the flow profile over the cardiac cycle at the outlets. It is however physically impossible to use the inlet values from the MRI and fit the Windkessel parameters to obtain the values at the outlet.

Table 6.3: VENC settings

	VENC setting (cm/s)	Velocity range ± (m/s)	max of mean $\boldsymbol{v}$ (m/s)	mean of mean $\boldsymbol{v}$ (m/s)
Inlet	80	0.8	0.193	0.0378
Arterial outlet	150	1.5	0.35	0.28
Venous outlet	150	1.5	1.33	0.95

There is little data available on the pressure in brachial–cephalic fistulas. Cuff pressure cannot be measured on the arm where the fistula is situated as the increased pressure from the cuff may rupture the vein. One study measured pressure for a patient at the end of the fistula creation operation before removing the intra–vascular catheter [26]. The systolic and diastolic pressures measured were 50 and 20 mmHg respectively. These were for a fistula created in the radial artery, which is distal to the brachial artery. Another study measured the cuff pressure on the other arm for 110 patients [86]. The mean systolic and diastolic were 151 and 86 mmHg respectively. Yet another study found a way to determine the intra–access pressure ratio in fistulas and grafts [5]. The ratio between the cuff pressure and the pressure present in the fistula was found in the range 0.15-0.2. These values were determined from patients with different fistulas (radial–cephalic or brachial–basilic) and grafts. Using the intra–access pressure ratio values and the cuff pressure measure in [86] we can find a physically realistic range for both the systolic (22.65-30.2 mmHg) and diastolic pressure (12.9-17.2 mmHg) in the brachial vein.

Table 6.4 shows the values used in the Windkessel model. Fig. 6.15 shows a comparison of the outflow obtained from the MRI at the venous and arterial outlets to the outflow obtained from the simulation. The flow from the simulation at both of the outlets is of the same order as the flow from the MRI. The outflow profile at the outlets follows the same pattern over time even though there is a small difference in the values.

Table 6.4: Windkessel parameters

	R (Pa s/m^3)	R_d (Pa s/m^3)	C (m^3/(Pa s))	τ
Arterial outlet	1.3458×10^7	2.0240×10^8	4.9407×10^{-9}	9.999978×10^{-1}
Venous outlet	2.6808×10^9	1.4572×10^{10}	6.2352×10^{-11}	9.086644×10^{-1}

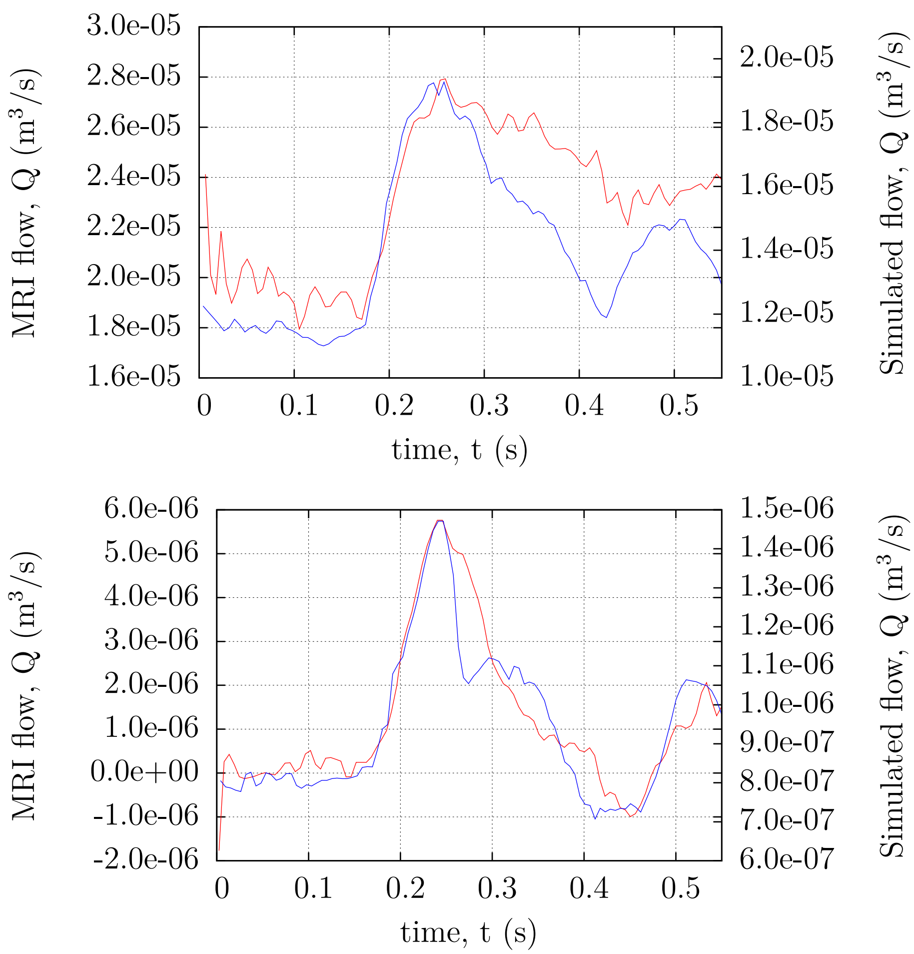

Fig. 6.15: Flow at the venous (top) and arterial (bottom) outlets obtained from MRI (red) and simulation (blue).

6.2.2 Demonstration of patient–specific related features

The implementation of the patient–specific features described in Chapter 4 are illustrated in this section.

Fibre directions

A description of the implementation of the fibre directions can be found in section 4.2.2. The fibre directions in the reference domain $\boldsymbol{a}_{0,i}$ of a patient–specific fistula are shown in Fig. 6.16 (a). The fibre directions were calculated using the pre–stress algorithm described in section 4.2.1. At the anastomosis a smooth transition of the direction of the fibres (Fig. 6.16 (b)) and of the principal stresses (Fig. 6.16 (c)) can be observed.

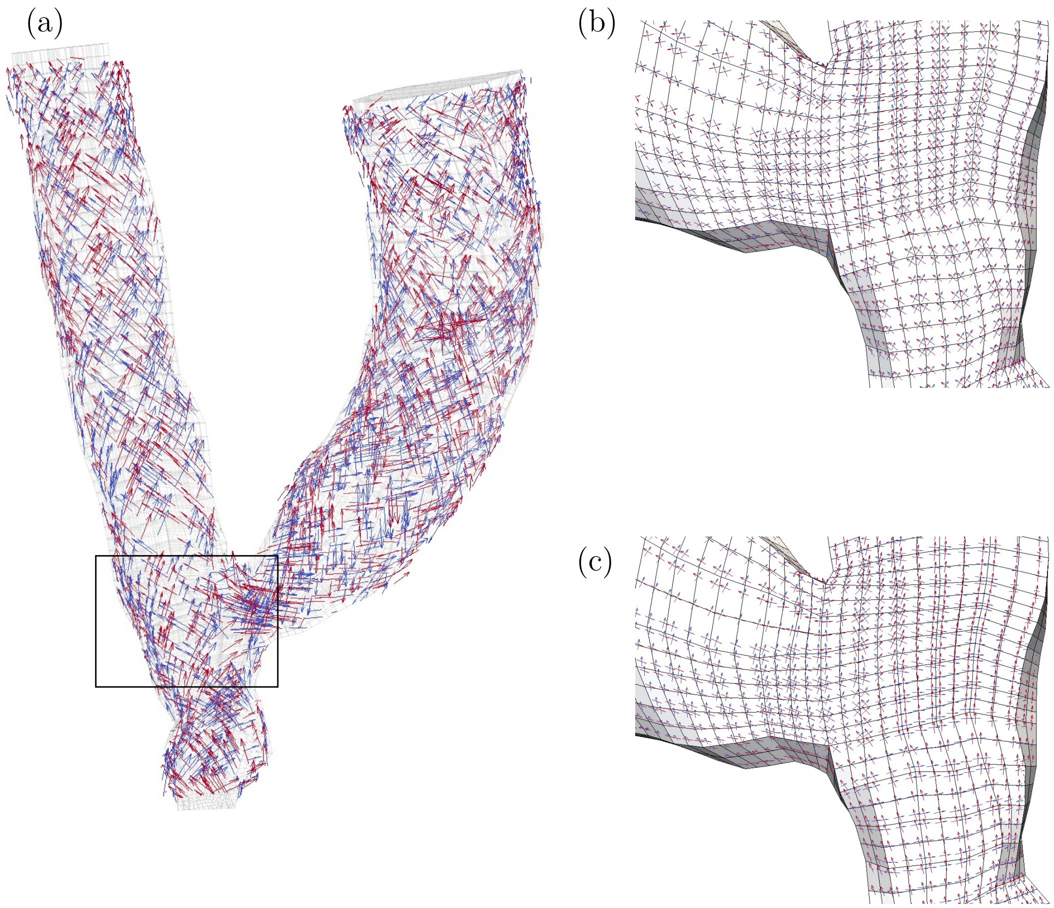

Fig. 6.16: (a) The fibre directions for a patient–specific geometry. (b) Fibre directions at the anastomosis. (c) Directions of the maximum principal stress and mid principal stress are used to find the circumferential and axial directions respectively. The circumferential and axial directions defined at each point are used to define the direction of the fibres.

Back flow stabilization

When the total outflow is negative (Fig. 6.15) or when a part of the outflow boundary experiences back flow (Fig. 6.17), back flow stabilization is needed to ensure that no numerical divergence takes place. The implementation of back flow stabilization was discussed in section 4.1.2.

Fig. 6.17 (top) shows the numerical divergence that occurs over time when back flow stabilization is not applied. Fig. 6.17 (bottom) shows results at the same time steps when back flow stabilization is applied. The numerical divergence is circumvented without altering the flow.

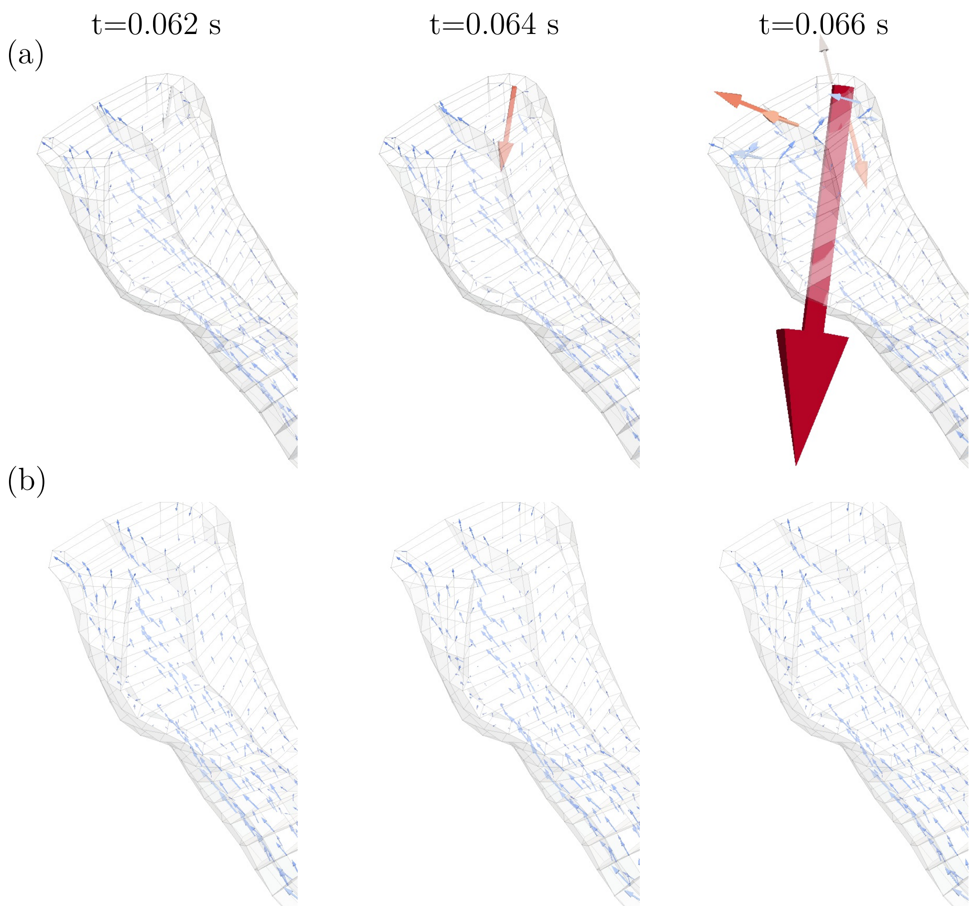

Fig. 6.17: Velocity vectors at different times. (a) Simulation divergence at an outlet as a result of numerical instabilities in the presence of back flow. (b) No simulation divergence at the same time steps when back flow stabilization is applied.

Pre–stress

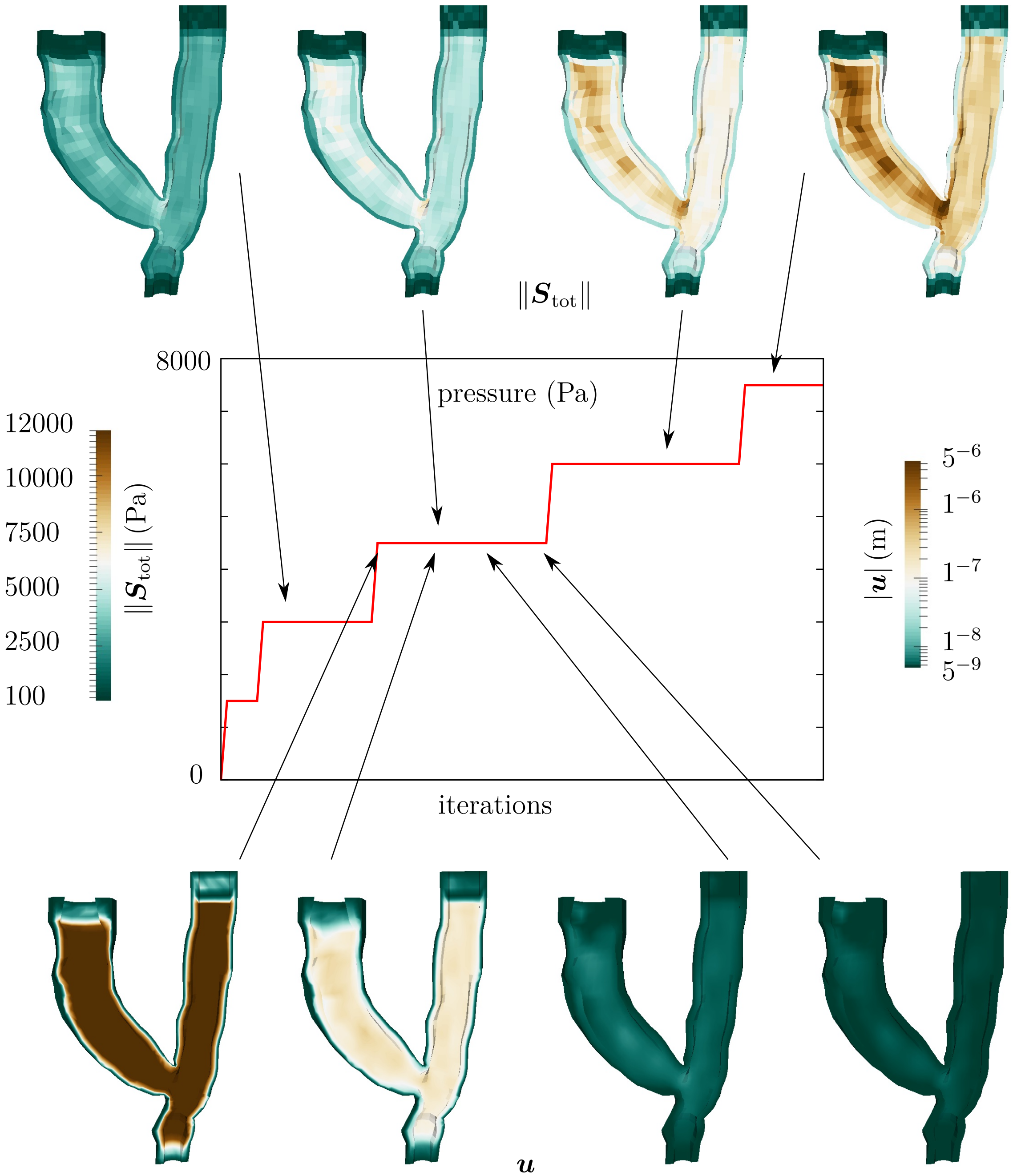

Fig. 6.18: Demonstration of the pre–stress algorithm. The pre–stress increases as the pressure applied at the outlet of the fluid boundary increases. During each iteration the displacements in the vessel and elastic material decrease.

The algorithm to calculate the pre–stress in the geometry acquired from the MRI is described in section 4.2.1. Fig. 6.18 demonstrates how the pre–stress increases for each increment in pressure that is applied at the outlets of the fluid domain. At the top of the figure the element average of the Frobenius norm ($\| \boldsymbol{S}_{\text{tot}} \| = \sqrt{\sum_{i=1}^{3}\sum_{i=j}^{3} | S_{ij} |^2}$) of the stress is shown. This is the total stress, i.e. the sum of the pre–stress and stress related to the strain $\boldsymbol{S}_{\text{tot}} = \boldsymbol{S} + \boldsymbol{S}_0$. As the strain and therefore the stress $\boldsymbol{S}$ approaches zero, the total stress can be regarded as the pre–stress so that $\boldsymbol{S}_{\text{tot}} \approx \boldsymbol{S}_0$.

The series of images at the bottom of Fig. 6.18 demonstrate how the displacement, and therefore strain, decreases when the stress is added to the pre–stress at each iteration $\boldsymbol{S}_0^n = \boldsymbol{S}_0^{n-1} + \boldsymbol{S}^n$ for a constant applied pressure. For each increment in the load the pre–stress algorithm is iterated until the strain becomes negligible ($| \boldsymbol{u} | < 1 \times 10^{-20}$).

6.2.3 Numerical considerations

The next section illustrates the effects of numerical stabilization and damping on the solution.

SUPG stabilization

The implementation of SUPG stabilization for convection dominated flow was described in section 3.5.1. The velocities present in the fistula (in the section distal to the anastomosis) in the time surrounding systolic flow are very high. For these timesteps the Peclet number exceeds the critical value and oscillations in the solution occur (Fig. 6.19 (a)). These oscillations dissapear after SUPG stabilization is implemented (Fig. 6.19 (b)).

Time discretization

Simulations were run using the generalised–α time integration scheme and for different values of ρ_∞. Results are shown in Fig. 6.20. Oscillations are observed when $\triangle t = 0.002$. When $\rho_\infty = 0.7$ some of the energy is damped and the oscillations disappear.

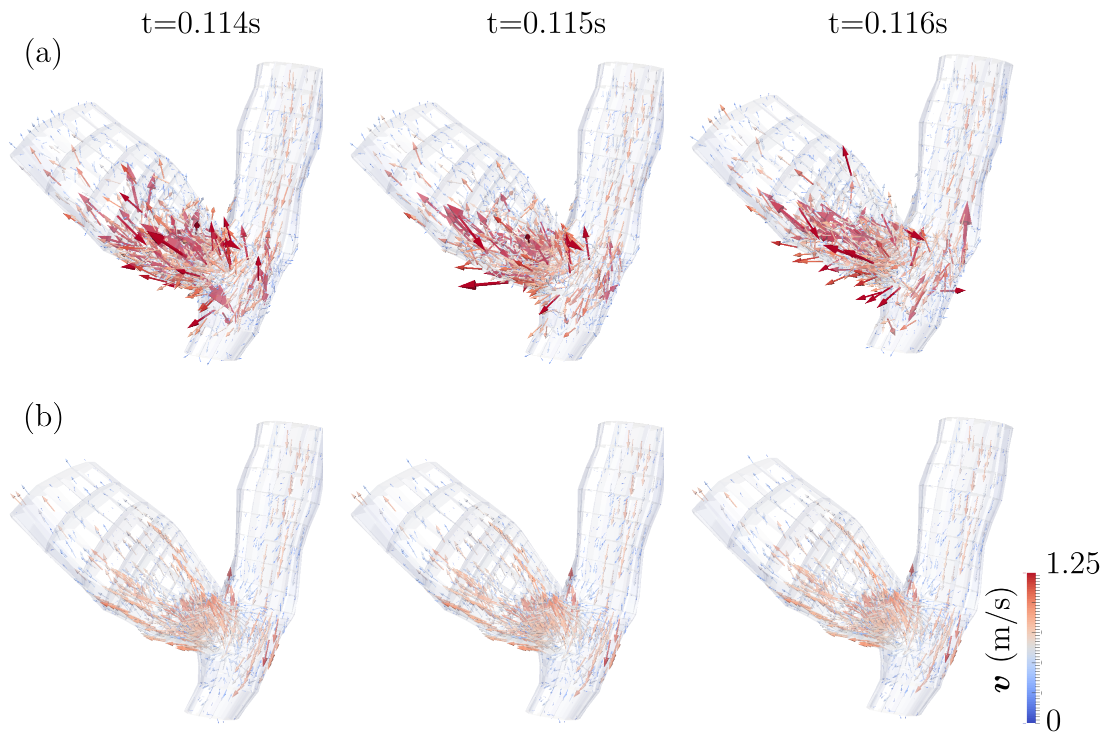

Fig. 6.19: Velocity vectors at different times (a) before and (b) after implementation of SUPG stabilization.

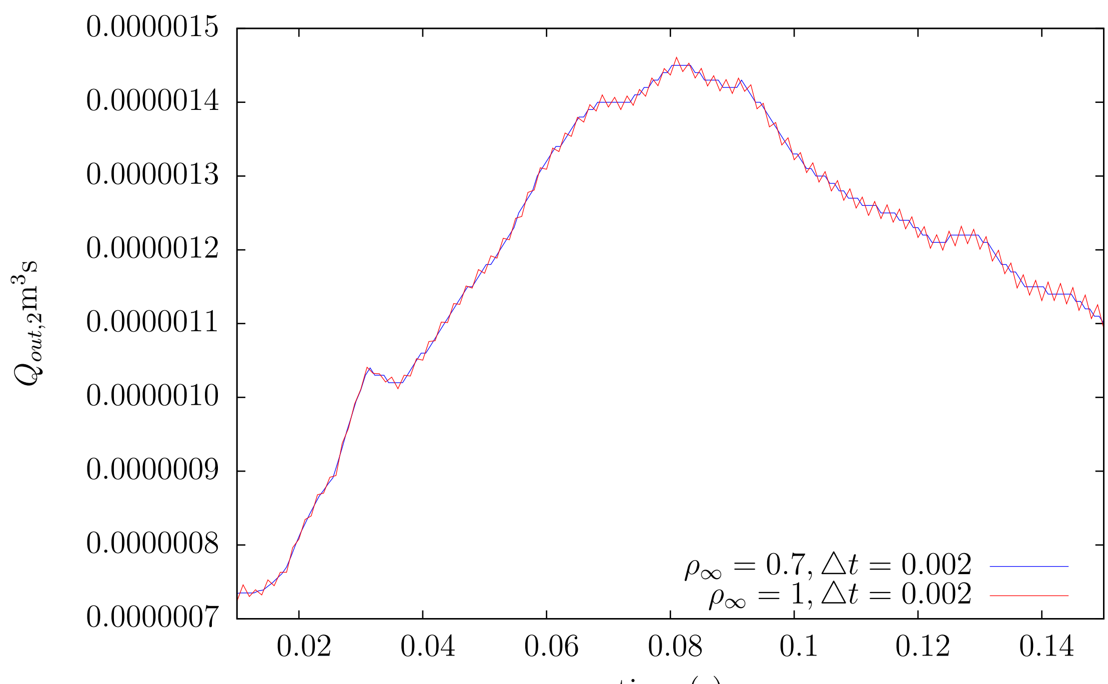

Fig. 6.20: Flow at the arterial outlet of the fistula for different values of ρ_∞. When $\rho_\infty = 1$ there is no damping and when $\rho_\infty = 0.7$ some of the energy is damped.

Damping in solid at outlets

It is important that the pressure–displacement waves that are propagating at the speed of sound of the system, do not reflect at the outlets. The Windkessel boundary conditions allows the pressure waves in the fluid to leave the domain unhindered. The accompanying displacement waves in the solid are dealt with in a different manner. The solid domain is extended (as discussed in section 6.2.1) to allow displacement in all directions at the outlet without having a completely free–moving boundary. Additionally damping terms, that are applied in regions of the structure close to the outlets, absorb some of the energy of the waves (as discussed in section 4.1.3). The effect of these damping terms on the solution is shown in Fig. 6.21. When $\gamma_w = 0$ and $\gamma_s = 0$ small oscillations are present in the solution. When damping is implemented, these oscillations are not present.

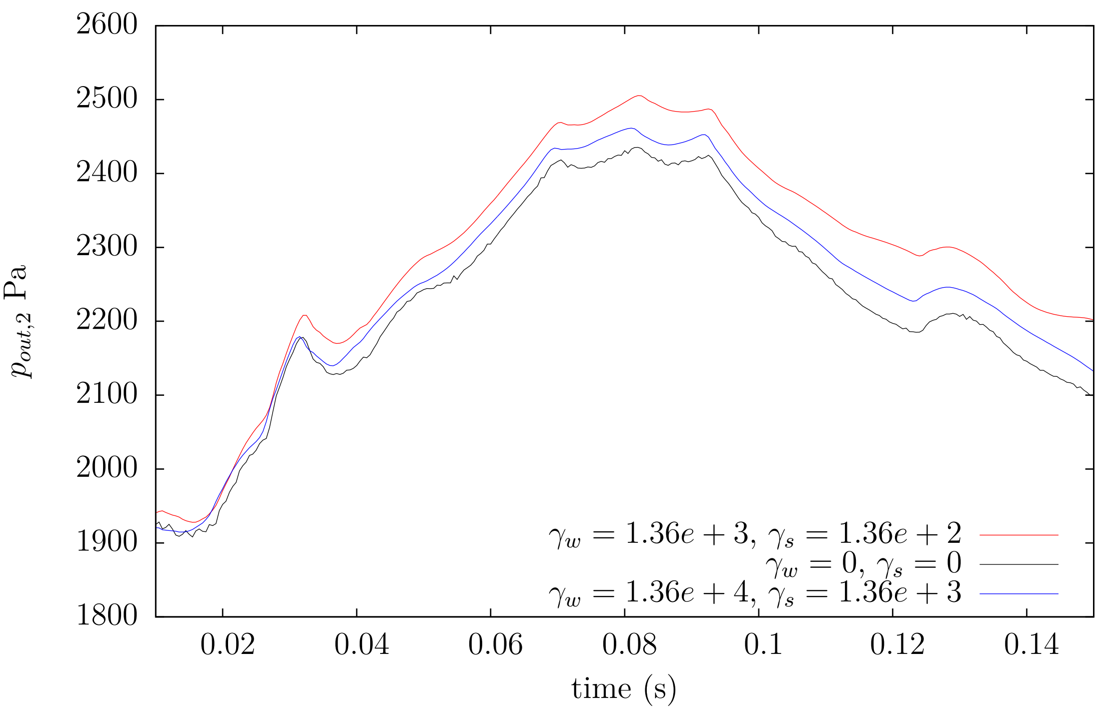

Fig. 6.21: Pressure at the arterial outlet for different values of the damping coefficients γ_w and γ_s.

6.2.4 Validation

To evaluate the reliability of the results from the finite element code the flow fields from the simulations is compared to the flow data obtained from MRI. The velocity acquisition from MRI is discussed in section 4.2.3.

When assessing whether the computational model is reasonable, the sources of inaccuracy from the processed MRI data should be kept in mind. These inaccuracies are discussed in section 6.2.1. The spatial and temporal resolution of the 4D MRI are low. When comparing the flow results from the 4D MRI (Fig.6.22 and Fig. 6.23) to the results from the 2D MRI (Fig. 6.24), it can be observed that the magnitude of the velocities obtained from the 2D data are roughly 4 times larger than the magnitude of the velocities obtained from the 4D data. Fig. 6.22 and 6.23 display 3D streamlines superimposed on a translucent image of the geometry. Fig. 6.24 displays velocity vectors at a cross–section located in the anastomosis.

To enable a comparison to the flow features in the fistula from the 4D MRI, the values of the velocity obtained from the simulation was scaled by 1/2. Two different dynamic ranges was chosen to allow comparisons of both the lower velocity flow patterns and the higher velocity flow patterns. The low dynamic range (Fig. 6.22) highlights the recirculation at the heel of the anastomosis. The high dynamic range (Fig. 6.23) shines a light on the flow patterns with higher velocity at the foot of the anastomosis. The results from the simulation compares well with results from the MRI.

The spatial and temporal resolution of the 3D MRI data is much better than the 4D data. At the anastomosis the velocities are extremely high and wrapping occurs (see section 6.2.1). This is indicated in Fig. 6.24. The velocities are also somewhat smaller than those recorded from the MRI. However, the general flow patterns are captured by the simulation.

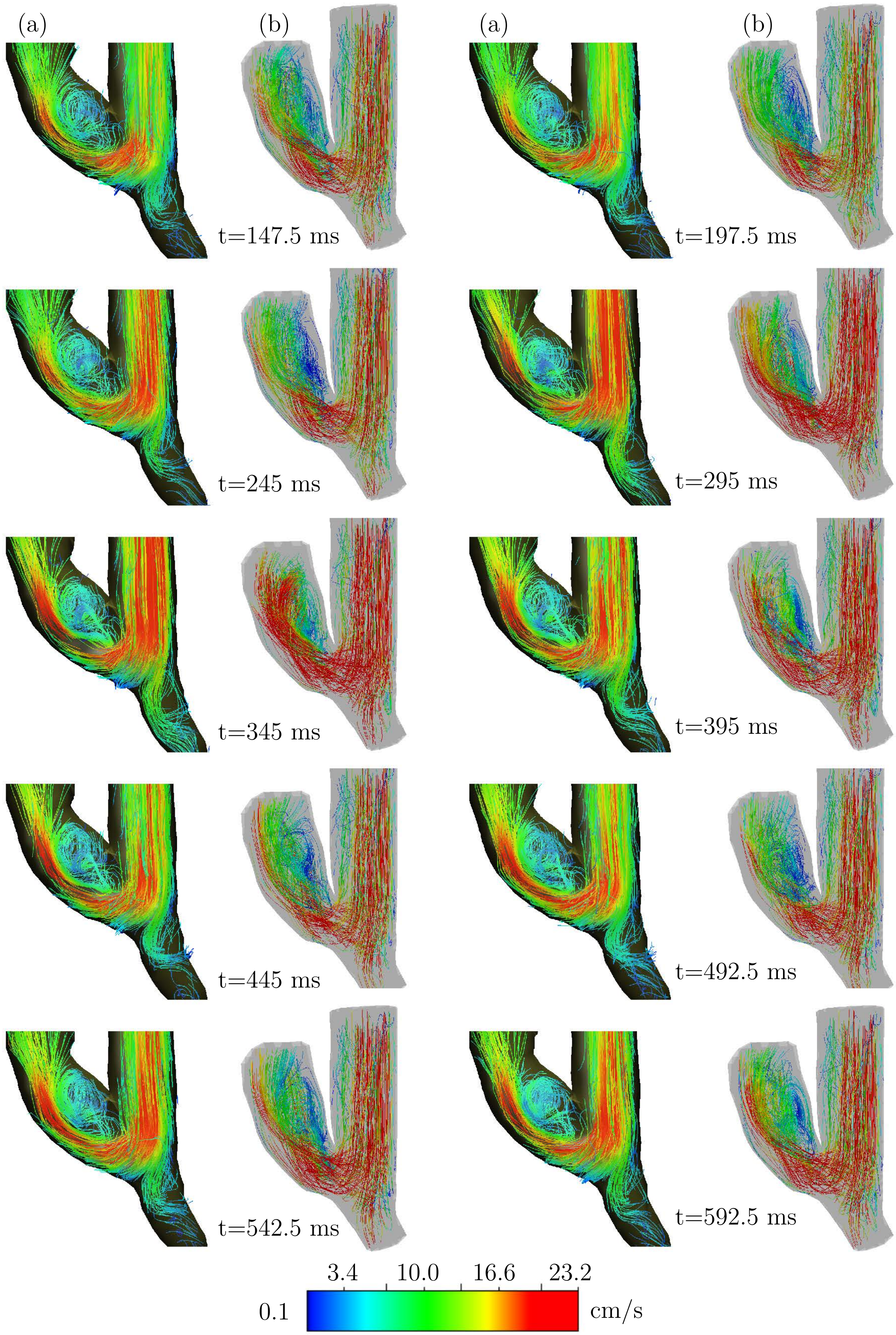

Fig. 6.22: Comparing volume streamlines from (b) the simulation to (a) those from MRI at different times. The 3D streamlines are displayed over a transclucent geometry.

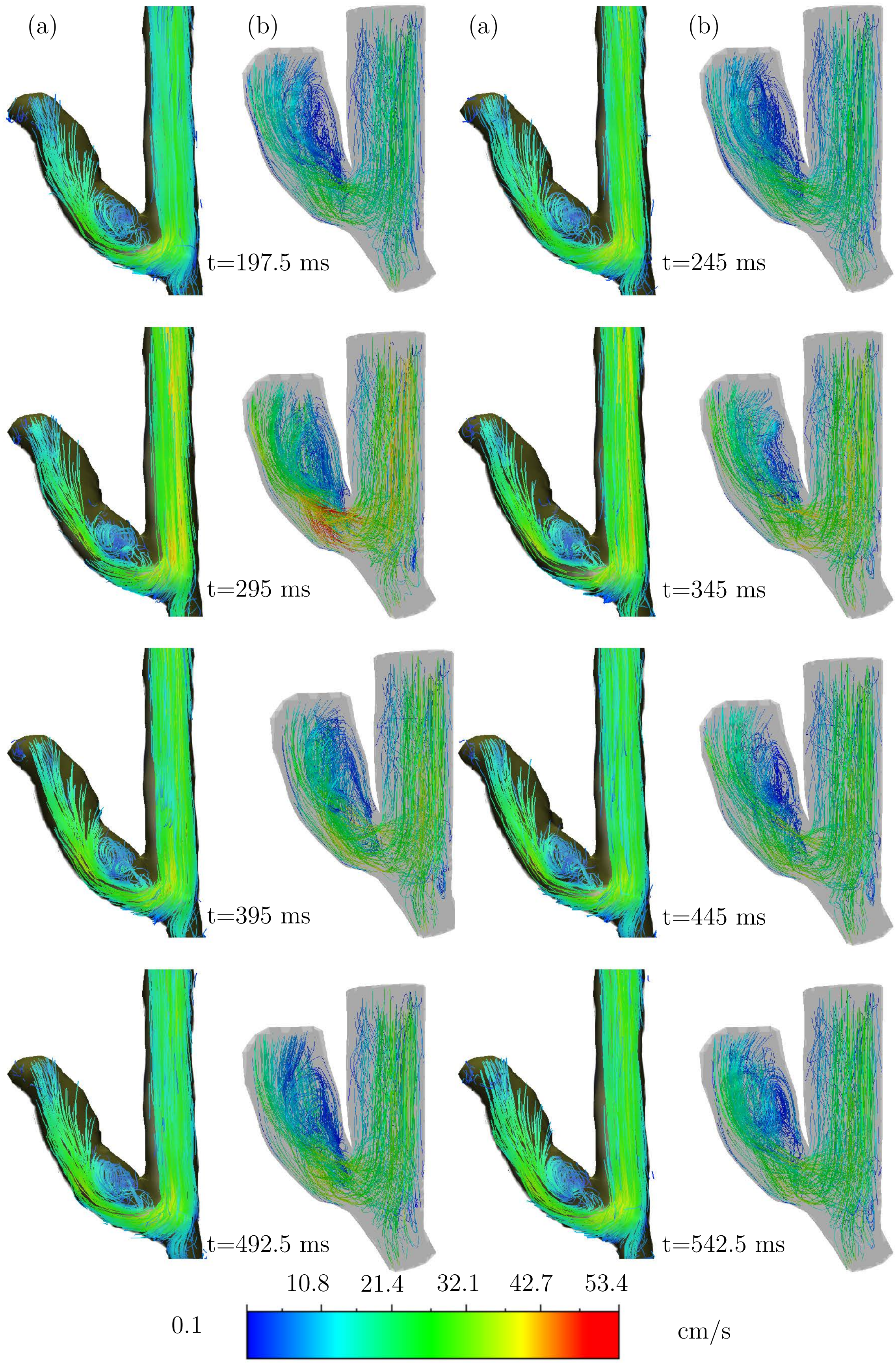

Fig. 6.23: Comparing volume streamlines from (b) the simulation to (a) those from MRI at different times. The 3D streamlines are displayed over a transclucent geometry.

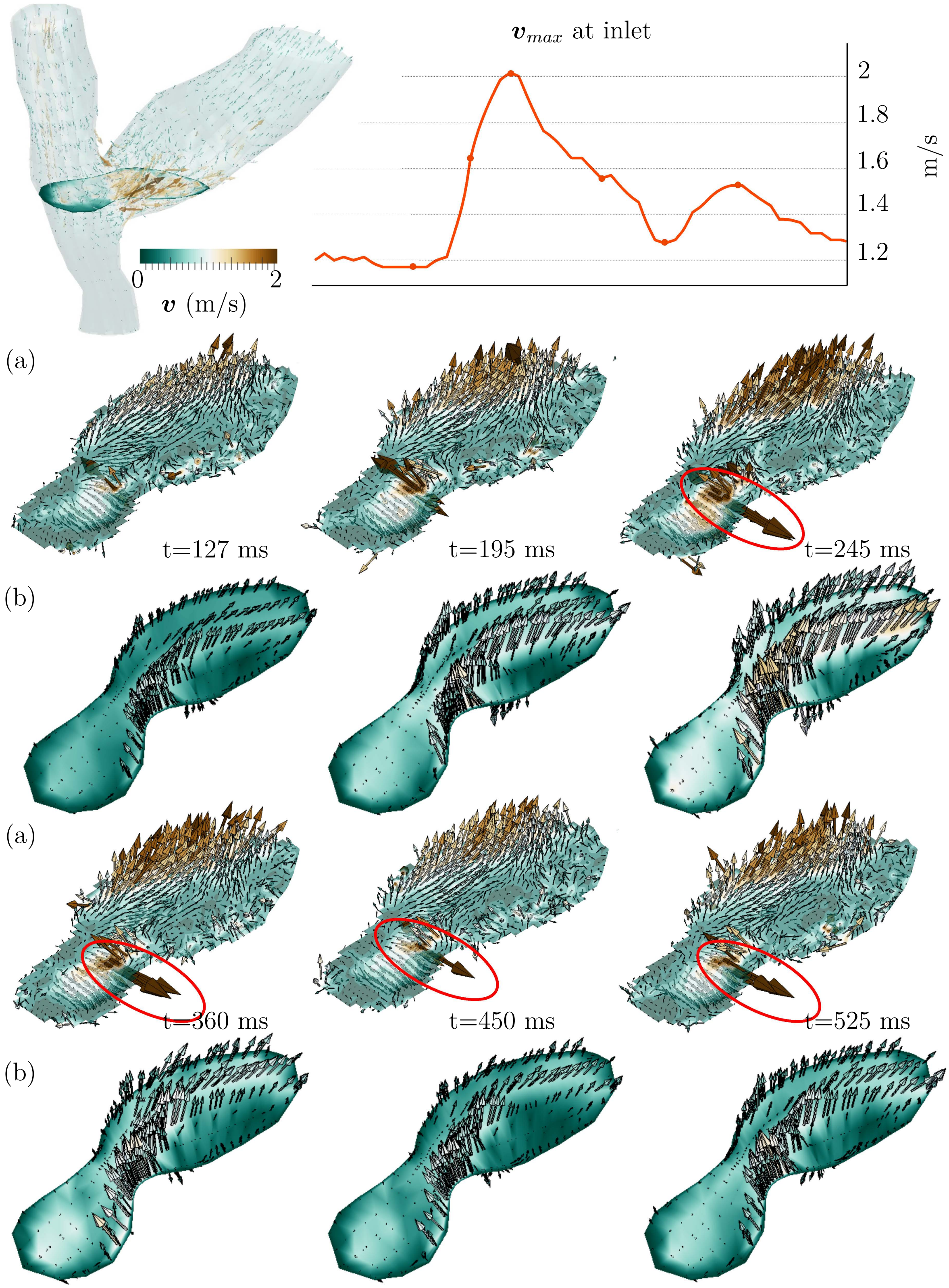

Fig. 6.24: Comparison: (a) 2D MRI results showing velocity vectors at different times compare to (b) results from the simulations. Red dots on the plot at the top of the figure indicates when in the cardiac cycle these times are. The red circles indicate when wrapping occurs.

6.2.5 Analysis

This section looks at information that can not be obtained from the MRI data, but which the simulation shed some light on. The wall shear stress (WSS), oscillatory shear index (OSI), stress present in the wall and propagation of the pressure wave are analysed.The WSS is given by

$$\mathrm{WSS} = \boldsymbol{\sigma n} - (\boldsymbol{\sigma n} \cdot \boldsymbol{n})\boldsymbol{n}, \tag{6.4}$$

and the OSI by

$$\mathrm{OSI} = 0.5\left(1 - \frac{|\int_0^{\mathrm{T}} \mathrm{WSSdt}|}{\int_0^{\mathrm{T}} |\mathrm{WSS}|\mathrm{dt}}\right). \tag{6.5}$$

The WSS is relatively low in most of the fistula, but a section of very high shear stress is present at the anastomosis (Fig. 6.25 (a)). The maximum shear stress is more than 30 times higher than the maximum normal physiological wall shear stress in veins and 10 times higher the normal physiological wall shear stress in large arteries [63]. WSS values of higher than 35 Pa [38] and lower than 0.2 Pa [73] are associated with the intimal hyperplasia. At the toe of the anastomis the WSS is greater than 35 Pa.

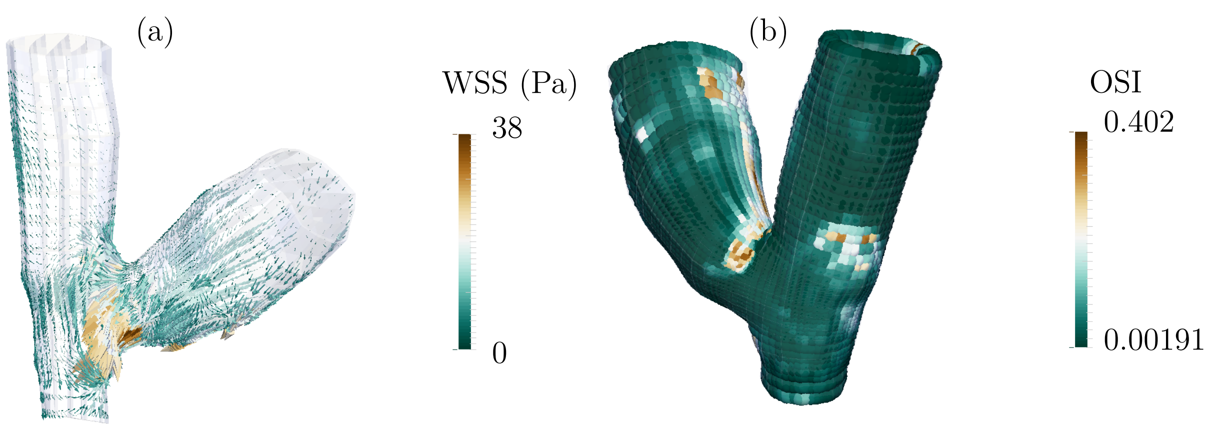

Fig. 6.25: (a) WSS and (b) OSI present in fistula at peak systole.

Regions of high OSI (>0.4) can be seen at the heel of the fistula, the fistula bed (or side–wall) and in the region where WSS are lower than the physiological range as a result of the recirculation (Fig. 6.25 (b)). It has been shown that regions where high oscillations in wall shear stress are present are associated with the formation of atheroma [28]. It has also been shown that when other systemic risk factors are present, altered flow patterns promote atherosclerosis [28].

The regions where the WSS values are above and below the acceptable range or where the OSI values are high, indicate regions where intimal hyperplasia and atheroma may occur. Intimal hyperplasia and atheroma may lead to thrombosis (clots that forms) which in turns leads to stenosis or embolism.

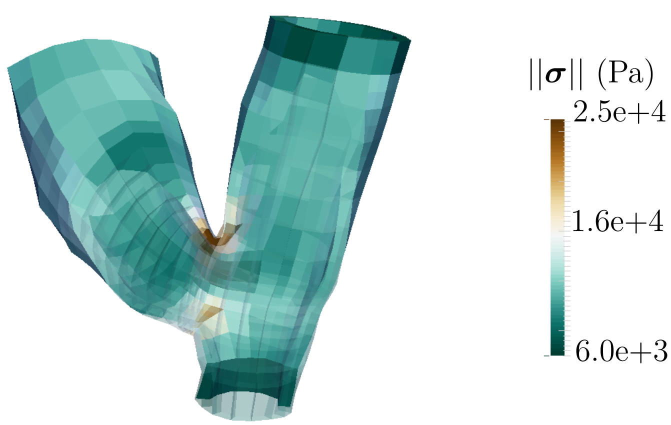

Fig. 6.26: Stress in the vessel walls.

Regions of high stress are present at the heel and toe of the anastomosis (Fig. 6.26). These are regions associated with intimal hyperplasia. The values are slightly higher but of the same order than reported elsewhere in literature [30].

The propagation of the pressure waves is shown in Fig. 6.27 using pressure contours. The figure highlights the propagation of two waves. The blue indicator follows a pressure wave propagating through the venous side of the anastomosis and the red indicator follows a wave propagating through the artery; the wave is reflected at the anastomosis. There is a region of low pressure visible at the heel of the anastomosis and a high pressure region at the toe of the anastomosis. These are the regions mostly associated with the formation of intimal hyperplasia.

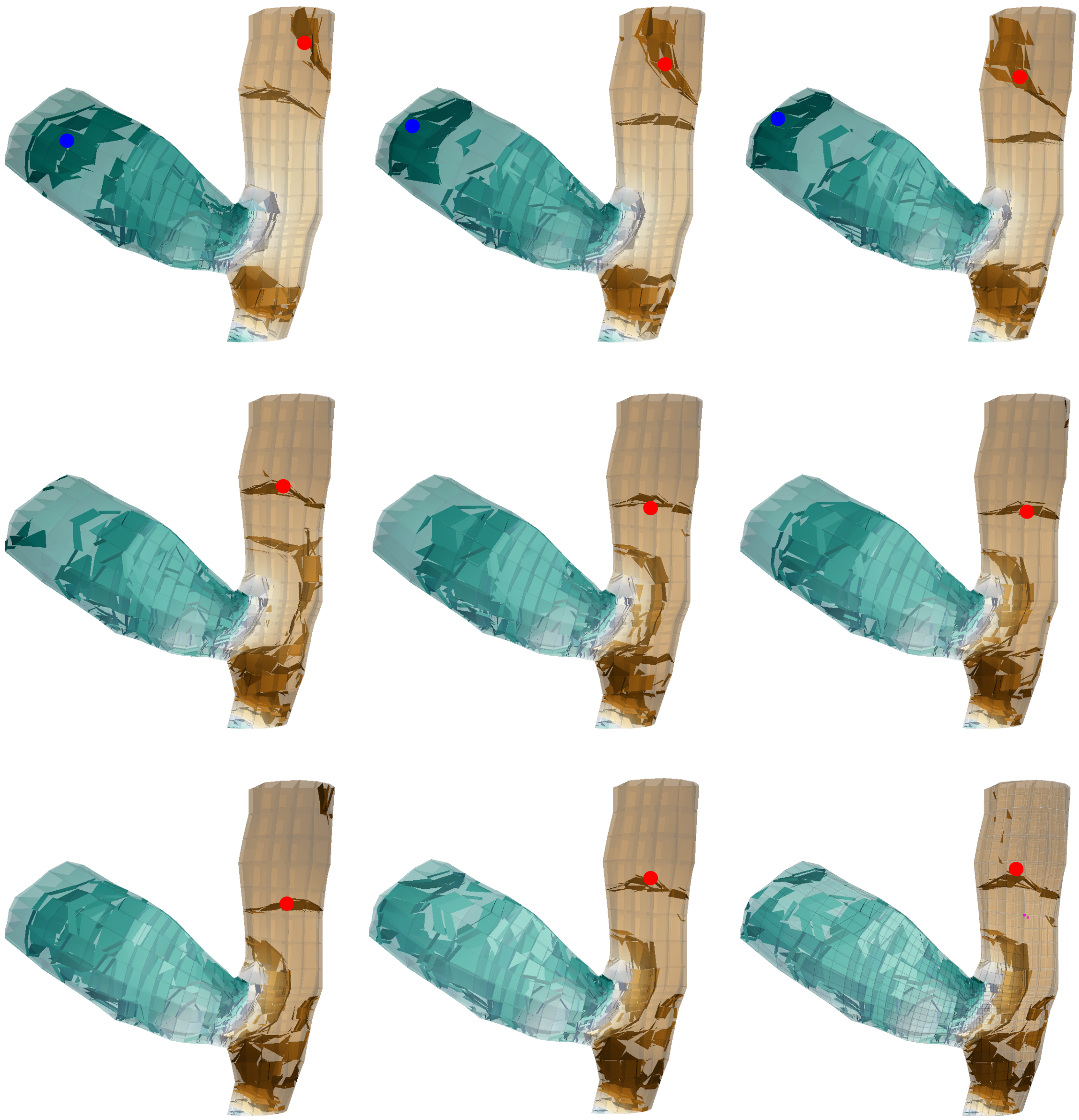

Fig. 6.27: Wave propagation for a period of 0.0038 s. The pictures shows consecutive timesteps from left to right starting at the top row. The blue circle labels a wave propagating throug the vein. The red circle labels a wave propagating through the artery; it gets reflected at the anastomosis.

6.3 Further applications of the computational model

In this section we give an example of how the computational model can be used to analyse other patient–specific fistulas. A geometry is created from MRI taken of a second patient. The images are processed using Simpleware [88]. It is meshed using ANSA [13]. In the absence of velocity data for the patient concerned, velocity data from the patient discussed in the previous section are used as inlet conditions.

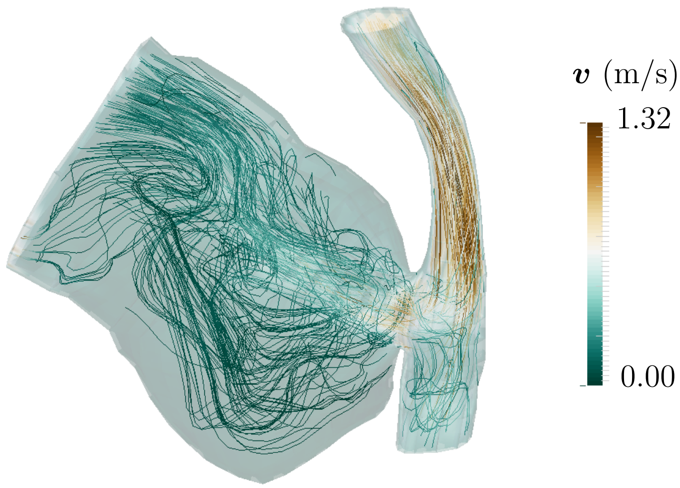

Fig. 6.28: Streamlines in fistula at peak systole.

Results from the simulations at peak systole are shown. The streamlines in Fig. 6.28 shows recirculation in the vein and in the artery distal to the anastomosis. The velocities in the vein are low.

High WSS values are found in the artery and at the toe of the anastomosis. Low WSS values are found in the vein, especially at the bottom of the bulge in the vein where the WSS is lower than 0.2 Pa. Thus there are both regions of high and low WSS that fall in the range associated with intimal hylperplasia. The regions where the WSS are very high and very low corresponds to the regions of high and low WSS values in the patient discussed in the previous section.

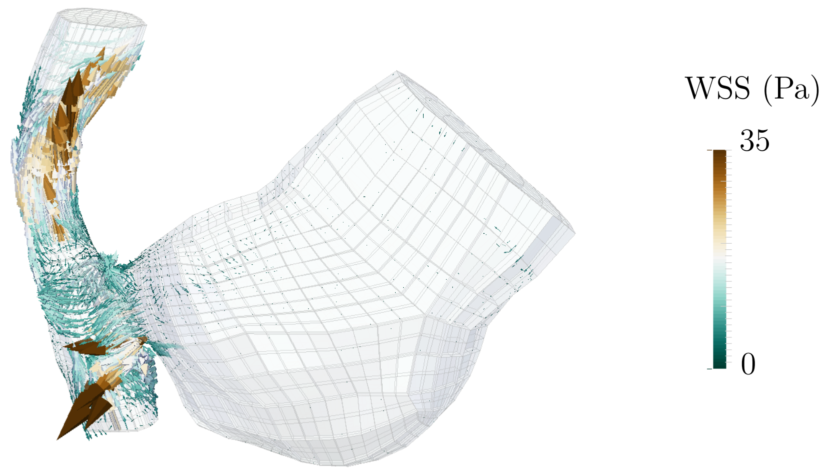

Fig. 6.29: Spatial distribution of WSS in fistula at peak systole.

In regions where flow recirculation in the vein are seen, high OSI values are found (Fig. 6.30). At the heel of the anastomosis OSI values are also high. The areas of high OSI is similar to the regions of high OSI in the patient discussed in the previous section.

Fig. 6.30: Spatial distribution of OSI in fistula at peak systole.

6.4 Chapter summary

The verification and validation of the computational code were shown in this chapter. Several benchmark examples were recreated. The implementation of patient–specific features were illustrated. The flow from the patient–specific simulation was compared to the flow obtained from MRI. Regions of very high and low WSS and high OSI were identified and correspond to the regions where intimal hyperplasia occur.

7

Conclusions and recommendations

7.1 Relevance of this work

This thesis described the development of a 3D parallel FSI code to simulate blood flow in fistulas. Attention was given to creating and using a patient–specific geometry for the simulations. The code was validated against flow data processed from velocity encoded MRI. The most important novelty is the consistent integration of state-of-the-art modelling assumptions into a robust numerical frame. Such robust numerical frames are mandatory to investigate physical phenomena in the cardiovascular system.

Various open source FE codes [79, 99] were extended to account for:

- the 3D geometry;
- parallel computations;
- classes and functions necessary to store relevant data at certain boundaries, to integrate the flow over the boundary and to calculate and store the Windkessel–values;
- classes and functions required to calculate WSS and OSI at the interface;
- classes and functions that calculate the fibre–directions and pre–stress.

Although many FSI codes and studies on haemodynamics and vascular mechanics exist, most of these codes have not been validated by in vivo data. This study incorporated experimental data obtained from velocity encoded 4D MRI. Although it was difficult to execute a quantitative comparison, the flow patterns from the simulation shows very good agreement to those obtained from the MRI.

Regions of very high and low WSS and high OSI corresponds to regions where intimal hyperplasia occur. A region of high (> 35 Pa) WSS is present in both patients at the toe of the anastomosis. A region of high OSI (> 0.4) is present at the heel of the anastomosis. High OSI values are also found where there is flow recirculation, especially in the vein.

Fistulas created in the upper arm that connects the cephalic vein to the brachial artery may be the last resort for patients with end stage renal disease. It is important to create the fistula in such a way that the patency rate is as high as possible. Understanding the flow and stress inside the fistula will contribute to the improvement of haemodialysis procedures. The FSI code developed here is a starting point for further investigations into the angle of connection, the connection site of the fistula and the influence of WSS, oscillatory wall shear stress and stress in the vessel wall.

7.2 Future work

The most urgent work that still needs to be done, is to run the simulations on a finer mesh without increasing the computational time significantly. To achieve this an iterative solver and pre–conditioner should be implemented [46]. Adaptive time-stepping may decrease the simulation time by increasing the time-step size in the temporal regions far from the systolic pressure.

To calibrate the Windkessel parameters more accurately, better flow data is necessary. The effect of shear thinning and other non-linear effects that blood exhibits at low shear rates, should be investigated [101].

In order to make general conclusions into ideal fistula geometries the study should be extended to include more patients.

To be able to assist in surgical planning, a temporal study needs to be done and re-modelling of the vessels should be included in the model [70]. The 3D model should be included in a closed 1D model of the arterial network to predict the flow increase resulting from creating the fistula. Such a simulation tool might assist to predict whether the fistula will mature, and can make a prediction on the patency of the fistula to enable early intervention. Clinical studies need to be performed to prove the merit of FSI simulations prior to their implementation in the clinical work flow.

References

[1] Alastrué, V., Garía, A., Peña, E., Rodríguez, J. F., Martínez, M. A., Doblaré, M., 2010. Numerical framework for patient-specific computational modelling of vascular tissue. International Journal for Numerical Methods in Biomedical Engineering 26 (1), 35–51.

[2] Alastrué, V., Peña, E., Martínez, M. A., Doblaré, M., 2007. Assessing the use of the "opening angle method" to enforce residual stresses in patient-specific arteries. Annals of Biomedical Engineering 35 (10), 1821–1837.

[3] Alastrué, V., Peña, E., Martínez, M. A., Doblaré, M., 2008. Experimental study and constitutive modelling of the passive mechanical properties of the ovine infrarenal vena cava tissue. Journal of Biomechanics 41 (14), 3038–3045.

[4] Allon, M., Robbin, M. L., 2002. Increasing arteriovenous fistulas in hemodialysis patients: problems and solutions. Kidney International 62 (4), 1109–1124.

[5] Ash, S. R., Dhamija, R., Zaroura, M. Y., Hentschel, D. M., 2012. The StenTec gauge for measuring static intra-access pressure ratio (PIa ratio) of fistulas and grafts. In: Seminars in dialysis. Vol. 25. Wiley Online Library, Blackwell Publishing Ltd., pp. 474–481.

[6] Badel, P., Rohan, C. P. Y., Avril, S., 2013. Finite element simulation of buckling-induced vein tortuosity and influence of the wall constitutive properties. Journal of the Mechanical Behavior of Biomedical Materials.

[7] Bangerth, W., Burstedde, C., Heister, T., Kronbichler, M., 2011. Algorithms and data structures for massively parallel generic adaptive finite element codes. ACM Transactions on Mathematical Software (TOMS) 38 (2), 14.

[8] Bangerth, W., Hartmann, R., Kanschat, G., 2007. deal. II-a general-purpose object-oriented finite element library. ACM Transactions on Mathematical Software (TOMS) 33 (4), 24.

[9] Bank, A. J., Kaiser, D. R., Rajala, S., Cheng, A., 1999. In vivo human brachial artery elastic mechanics effects of smooth muscle relaxation. Circulation 100 (1), 41–47.

[10] Bazilevs, Y., Calo, V. M., Hughes, T. J. R., Zhang, Y., 2008. Isogeometric fluid-structure interaction: theory, algorithms, and computations. Computational Mechanics 43 (1), 3–37.

[11] Bazilevs, Y., Gohean, J. R., Hughes, T. J. R., Moser, R. D., Zhang, Y., 2009. Patient-specific isogeometric fluid–structure interaction analysis of thoracic aortic blood flow due to implantation of the Jarvik 2000 left ventricular assist device. Computer Methods in Applied Mechanics and Engineering 198 (45), 3534–3550.

[12] Belytschko, T., Liu, W. K., Moran, B., Elkhodary, K., 2013. Nonlinear finite elements for continua and structures. John Wiley & Sons.

[13] BETA, C. A. E., 2009. Systems sa. ANSA User's Guide.

[14] Boghosian, M., Cassel, K., Hammes, M., Funaki, B., Kim, S., Qian, X., Wang, X., Dhar, P., Hines, J., 2014. Hemodynamics in the cephalic arch of a brachiocephalic fistula. Medical engineering & physics 36 (7), 822–830.

[15] Botti, L., Van Canneyt, K., Kaminsky, R., Claessens, T., Planken, R. N., Verdonck, P., Remuzzi, A., Antiga, L., 2013. Numerical evaluation and experimental validation of pressure drops across a patient-specific model of vascular access for hemodialysis. Cardiovascular Engineering and Technology 4 (4), 485–499.

[16] Boyd, J., Buick, J. M., Green, S., 2007. Analysis of the Casson and Carreau-Yasuda non-Newtonian blood models in steady and oscillatory flows using the lattice Boltzmann method. Physics of Fluids 19, 093103.

[17] Boyd, M. J., Buick, J. M., Green, S., 2007. Comparison of Newtonian and non-Newtonian oscillatory flows using the lattice Boltzmann method. In: World Congress on Medical Physics and Biomedical Engineering 2006. Springer, pp. 3395–3399.

[18] Braack, M., Burman, E., John, V., Lube, G., 2007. Stabilized finite element methods for the generalized oseen problem. Computer Methods in Applied Mechanics and Engineering 196 (4), 853–866.

[19] Brooks, A. N., Hughes, T. J., 1982. Streamline upwind/petrov-galerkin formulations for convection dominated flows with particular emphasis on the incompressible navier-stokes equations. Computer Methods in Applied Mechanics and Engineering 32 (1), 199–259.

[20] Canneyt, K. V., Pourchez, T., Eloot, S., Guillame, C., Bonnet, A., Segers, P., Verdonck, P., 2010. Hemodynamic impact of anastomosis size and angle in side-to-end arteriovenous fistulae: a computer analysis. Journal of Vascular Access 11 (1), 52–58.

[21] Causin, P., Gerbeau, J. F., Nobile, F., 2005. Added-mass effect in the design of partitioned algorithms for fluid-structure problems. Computer Methods in Applied Mechanics and Engineering 194 (42), 4506–4527.

[22] Chabannes, V., Peña, G., Prud'homme, C., 2013. High order fluid structure interaction in 2D and 3D Application to blood flow in arteries. Journal of Computational and Applied Mathematics 246, 1–9.

[23] Chung, J., Hulbert, G. M., 1993. A time integration algorithm for structural dynamics with improved numerical dissipation: the generalized-α method. Journal of Applied Mechanics 60 (2), 371–375.

[24] Cignoni, P., Corsini, M., Ranzuglia, G., 2008. Meshlab: an open-source 3D mesh processing system. Ercim news 73 (45-46), 6.

[25] Cinat, M. E., Hopkins, J., Wilson, S. E., 1999. A prospective evaluation of PTFE graft patency and surveillance techniques in hemodialysis access. Annals of Vascular Surgery 13 (2), 191–198.

[26] Corpataux, J. M., Haesler, E., Silacci, P., Ris, H. B., Hayoz, D., 2002. Low-pressure environment and remodelling of the forearm vein in Brescia–Cimino haemodialysis access. Nephrology Dialysis Transplantation 17 (6), 1057–1062.

[27] Crosetto, P., Reymond, P., Deparis, S., Kontaxakis, D., Stergiopulos, N., Quarteroni, A., 2011. Fluid-structure interaction simulation of aortic blood flow. Computers & Fluids 43 (1), 46–57.

[28] Cunningham, K. S., Gotlieb, A. I., 2005. The role of shear stress in the pathogenesis of atherosclerosis. Laboratory investigation 85 (1), 9–23.

[29] Decorato, I., Kharboutly, Z., Legallais, C., Salsac, A. V., 2011. Numerical study of the influence of wall compliance on the haemodynamics in a patient-specific arteriovenous fistula. Computer Methods in Biomechanics and Biomedical engineering 14 (sup1), 121–123.

[30] Decorato, I., Kharboutly, Z., Vassallo, T., Penrose, J., Legallais, C., Salsac, A.-V., 2014. Numerical simulation of the fluid structure interactions in a compliant patient-specific arteriovenous fistula. International journal for numerical methods in biomedical engineering 30 (2), 143–159.

[31] Donea, J., Giuliani, S., Halleux, J. P., 1982. An arbitrary Lagrangian-Eulerian finite element method for transient dynamic fluid-structure interactions. Computer Methods in Applied Mechanics and Engineering 33 (1), 689–723.

[32] Ene-Iordache, B., Remuzzi, A., 2012. Disturbed flow in radial-cephalic arteriovenous fistulae for haemodialysis: low and oscillating shear stress locates the sites of stenosis. Nephrology Dialysis Transplantation 27 (1), 358–368.

[33] Ethier, C. R., Simmons, C. A., 2007. Introductory Biomechanics: from Cells to Organisms. Cambridge University Press.

[34] Figueroa, C. A., Vignon-Clementel, I. E., Jansen, K. E., Hughes, T. J., Taylor, C. A., 2006. A coupled momentum method for modeling blood flow in three-dimensional deformable arteries. Computer Methods in Applied Mechanics and Engineering 195 (41), 5685–5706.

[35] Fischer, P. F., Loth, F., Lee, S. E., Lee, S. W., Smith, D. S., Bassiouny, H. S., 2007. Simulation of high-Reynolds number vascular flows. Computer Methods in Applied Mechanics and Engineering 196 (31), 3049–3060.

[36] Formaggia, L., Gerbeau, J. F., Nobile, F., Quarteroni, A., 2001. On the coupling of 3D and 1D Navier-Stokes equations for flow problems in compliant vessels. Computer Methods in Applied Mechanics and Engineering 191 (6), 561–582.

[37] Formaggia, L., Quarteroni, A. M., Veneziani, A., 2009. Cardiovascular Mathematics: Modeling and Simulation of the Circulatory System. Vol. 1. Springer.

[38] Fry, D. L., 1968. Acute vascular endothelial changes associated with increased blood velocity gradients. Circulation research 22 (2), 165–197.

[39] Fung, Y. C., 1993. Biomechanics: Mechanical Properties of Living Tissues. Springer.

[40] Gasser, T. C., Holzapfel, G. A., 2002. A rate-independent elastoplastic constitutive model for biological fiber-reinforced composites at finite strains: continuum basis, algorithmic formulation and finite element implementation. Computational Mechanics 29 (4-5), 340–360.

[41] Gasser, T. C., Ogden, R. W., Holzapfel, G. A., 2006. Hyperelastic modelling of arterial layers with distributed collagen fibre orientations. Journal of the Royal Society Interface 3 (6), 15–35.

[42] Gee, M., Förster, C., Wall, W., 2010. A computational strategy for prestressing patient-specific biomechanical problems under finite deformation. International Journal for Numerical Methods in Biomedical Engineering 26 (1), 52–72.

[43] Gee, M. W., Reeps, C. H., Eckstein, H. H., Wall, W. A., 2009. Prestressing in finite deformation abdominal aortic aneurysm simulation. Journal of Biomechanics 42 (11), 1732–1739.

[44] Guidoboni, G., Glowinski, R., Cavallini, N., Canic, S., 2009. Stable loosely-coupled-type algorithm for fluid-structure interaction in blood flow. Journal of Computational Physics 228 (18), 6916–6937.

[45] Haruguchi, H., Teraoka, S., 2003. Intimal hyperplasia and hemodynamic factors in arterial bypass and arteriovenous grafts: a review. Journal of Artificial Organs 6 (4), 227–235.

[46] Heil, M., 2004. An efficient solver for the fully coupled solution of large-displacement fluid-structure interaction problems. Computer Methods in Applied Mechanics and Engineering 193 (1), 1–23.

[47] Heroux, M. A., Bartlett, R. A., Howle, V. E., Hoekstra, R. J., Hu, J. J., Kolda, T. G., Lehoucq, R. B., Long, K. R., Pawlowski, R. P., Phipps, E. T., Salinger, A. G., Thornquist, H. K., Tuminaro, R. S., Willenbring, J. M., Williams, A., Stanley, K. S., 2005. An overview of the trilinos project. ACM Transactions on Mathematical Software 31 (3), 397–423.

[48] Hofer, M., Rappitsch, G., Perktold, K., Trubel, W., Schima, H., 1996. Numerical study of wall mechanics and fluid dynamics in end-to-side anastomoses and correlation to intimal hyperplasia. Journal of Biomechanics 29 (10), 1297–1308.

[49] Holzapfel, G. A., 2000. Nonlinear Solid Mechanics: A Continuum Approach for Engineering.

[50] Holzapfel, G. A., Gasser, T. C., 2001. A viscoelastic model for fiber-reinforced composites at finite strains: Continuum basis, computational aspects and applications. Computer Methods in Applied Mechanics and Engineering 190 (34), 4379–4403.

[51] Holzapfel, G. A., Gasser, T. C., Ogden, R. W., 2000. A new constitutive framework for arterial wall mechanics and a comparative study of material models. Journal of Elasticity and the Physical Science of Solids 61 (1-3), 1–48.

[52] Hsu, M. C., Bazilevs, Y., 2011. Blood vessel tissue prestress modeling for vascular fluid-structure interaction simulation. Finite Elements in Analysis and Design 47 (6), 593–599.

[53] Huberts, W., Canneyt, K. V., Segers, P., Eloot, S., Tordoir, J. H. M., Verdonck, P., van de Vosse, F. N., Bosboom, E. M. H., 2012. Experimental validation of a pulse wave propagation model for predicting hemodynamics after vascular access surgery. Journal of Biomechanics 45 (9), 1684–1691.

[54] Hughes, T. J. R., Liu, W. K., Zimmermann, T. K., 1981. Lagrangian-Eulerian finite element formulation for incompressible viscous flows. Computer Methods in Applied Mechanics and Engineering 29 (3), 329–349.

[55] Janela, J., Moura, A., Sequeira, A., 2010. A 3D non-Newtonian fluid-structure interaction model for blood flow in arteries. Journal of Computational and Applied Mathematics 234 (9), 2783–2791.

[56] Jansen, K. E., Whiting, C. H., Hulbert, G. M., 2000. A generalized-α method for integrating the filtered navier–stokes equations with a stabilized finite element method. Computer Methods in Applied Mechanics and Engineering 190 (3), 305–319.

[57] Jarvinen, E., Raback, P., Lyly, M., Salenius, J. P., 2008. A method for partitioned fluid-structure interaction computation of flow in arteries. Medical Engineering

& Physics 30 (7), 917–923.

[58] Jermy, S., 2016. 4d flow and displacement sensitive mr imaging of upper-arm arteriovenous connections for haemodialysis. Master's thesis, University of Cape Town.

[59] Kaiser, D. R., Mullen, K., Bank, A. J., 2001. Brachial artery elastic mechanics in patients with heart failure. Hypertension 38 (6), 1440–1445.

[60] Kang, S., Choi, H., Yoo, J. Y., 2012. Investigation of fluid–structure interactions using a velocity-linked P2/P1 finite element method and the generalized-α method. International Journal for Numerical Methods in Engineering 90 (12), 1529–1548.

[61] Kharboutly, Z., Fenech, M., Treutenaere, J. M., Claude, I., Legallais, C., 2007. Investigations into the relationship between hemodynamics and vascular alterations in an established arteriovenous fistula. Medical Engineering & Physics 29 (9), 999–1007.

[62] Kim, Y. H., Kim, J. E., Ito, Y., Shih, A. M., Brott, B., Anayiotos, A., 2008. Hemodynamic analysis of a compliant femoral artery bifurcation model using a fluid structure interaction framework. Annals of Biomedical Engineering 36 (11), 1753–1763.

[63] Kroll, M. H., Hellums, J. D., McIntire, L., Schafer, A., Moake, J., 1996. Platelets and shear stress. Blood 88 (5), 1525–1541.

[64] Krueger, U., Zanow, J., Scholz, H., 2002. Computational fluid dynamics and vascular access. Artificial Organs 26 (7), 571–575.

[65] Lee, S. W., Smith, D. S., Loth, F., Fischer, P. F., Bassiouny, H. S., 2007. Importance of flow division on transition to turbulence within an arteriovenous graft. Journal of Biomechanics 40 (5), 981–992.

[66] Leuprecht, A., Kozerke, S., Boesiger, P., Perktold, K., 2003. Blood flow in the human ascending aorta: a combined MRI and CFD study. Journal of Engineering Mathematics 47 (3-4), 387–404.

[67] Li, X. S., Demmel, J. W., June 2003. Superlu_dist: A scalable distributed-memory sparse direct solver for unsymmetric linear systems. ACM Trans. Mathematical Software 29 (2), 110–140.

[68] Lu, J., Zhou, X., Raghavan, M. L., 2008. Inverse method of stress analysis for cerebral aneurysms. Biomechanics and Modeling in Mechanobiology 7 (6), 477–486.

[69] Malik, J., Tuka, V., Tesar, V., 2009. Local hemodynamics of the vascular access for hemodialysis. Kidney and Blood Pressure Research 32 (1), 59–66.

[70] Manini, S., Passera, K., Huberts, W., Botti, L., Antiga, L., Remuzzi, A., 2014. Computational model for simulation of vascular adaptation following vascular access surgery in haemodialysis patients. Computer Methods in Biomechanics and Biomedical Engineering 17 (12), 1358–1367.

[71] Markl, M., Kilner, P. J., Ebbers, T., 2011. Comprehensive 4D velocity mapping of the heart and great vessels by cardiovascular magnetic resonance. Journal of Cardiovascular Magnetic Resonance 13 (7), 10–1186.

[72] McGah, P. M., Leotta, D. F., Beach, K. W., Aliseda, A., 2014. Effects of wall distensibility in hemodynamic simulations of an arteriovenous fistula. Biomechanics and modeling in mechanobiology 13 (3), 679–695.

[73] Meyerson, S. L., Skelly, C. L., Curi, M. A., Shakur, U. M., Vosicky, J. E., Glagov, S., Christen, T., Gabbiani, G., Schwartz, L. B., 2001. The effects of extremely low shear stress on cellular proliferation and neointimal thickening in the failing bypass graft. Journal of Vascular Surgery 34 (1), 90–97.

[74] Moghadam, M. E., Bazilevs, Y., Hsia, T. Y., Vignon-Clementel, I. E., Marsden, A. L., et al., 2011. A comparison of outlet boundary treatments for prevention of backflow divergence with relevance to blood flow simulations. Computational Mechanics 48 (3), 277–291.

[75] Moireau, P., Xiao, N., Astorino, M., Figueroa, C. A., Chapelle, D., Taylor, C. A., Gerbeau, J. F., 2012. External tissue support and fluid-structure simulation in blood flows. Biomechanics and Modeling in Mechanobiology 11 (1-2), 1–18.

[76] Ngoepe, M. N., Reddy, B. D., Kahn, D., Meyer, C., Zilla, P., Franz, T., 2011. A numerical tool for the coupled mechanical assessment of anastomoses of PTFE arterio-venous access grafts. Cardiovascular Engineering and Technology 2 (3), 160–172.

[77] Niemann, A. K., Udesen, J., Thrysoe, S., Nygaard, J. V., Frund, E. T., Petersen, S. E., Hasenkam, J. M., 2010. Can sites prone to flow induced vascular complications in a-v fistulas be assessed using computational fluid dynamics? Journal of Biomechanics 43 (10), 2002–2009.

[78] O'Rourke, M. F., Staessen, J. A., Vlachopoulos, C., Duprez, D., 2002. Clinical applications of arterial stiffness; definitions and reference values. American Journal of Hypertension 15 (5), 426–444.

[79] Pelteret, J. P., McBride, A., October 2016. The step–44 tutorial program. URL `http://www.dealii.org/8.4.1/doxygen/deal.II/step_44.html`

[80] Pheatt, C., 2008. Intel® threading building blocks. Journal of Computing Sciences in Colleges 23 (4), 298–298.

[81] Polzer, S., Gasser, T. C., Forsell, C., Druckmüllerova, H., Tichy, M., Staffa, R., Vlachovsky, R., Bursa, J., 2013. Automatic identification and validation of planar collagen organization in the aorta wall with application to abdominal aortic aneurysm. Microscopy and Microanalysis 19 (06), 1395–1404.

[82] Quarteroni, A., Formaggia, L., 2004. Mathematical modelling and numerical simulation of the cardiovascular system. Handbook of Numerical Analysis 12, 3–127.

[83] Ren, J. S., 2011. Mechanical performance and negative pressure instability for venous walls. Applied Mathematics and Mechanics 32, 917–924.

[84] Roy, S., Silacci, P., Stergiopulos, N., 2005. Biomechanical proprieties of decellularized porcine common carotid arteries. American Journal of Physiology-Heart and Circulatory Physiology 289 (4), H1567–H1576.

[85] Ryou, H. S., Kim, S., Ro, K., 2013. A numerical study of the effect of catheter angle on the blood flow characteristics in a graft during hemodialysis. Korea-Australia Rheology Journal 25 (1), 19–27.

[86] Safar, M. E., Blacher, J., Pannier, B., Guerin, A. P., Marchais, S. J., Guyonvarc'h, P.-M., London, G. M., 2002. Central pulse pressure and mortality in end-stage renal disease. Hypertension 39 (3), 735–738.

[87] Stein, K., Tezduyar, T., Benney, R., 2003. Mesh moving techniques for fluid-structure interactions with large displacements. Journal of Applied Mechanics 70 (1), 58–63.

[88] Synopses, Mountain View, USA, 2016. Simpleware ScanIP.

[89] Takizawa, K., Christopher, J., Tezduyar, T. E., Sathe, S., 2010. Space-time finite element computation of arterial fluid-structure interactions with patient-specific data. International Journal for Numerical Methods in Biomedical Engineering 26 (1), 101–116.

[90] Taylor, C. A., Hughes, T. J. R., Zarins, C. K., 1998. Finite element modeling of three-dimensional pulsatile flow in the abdominal aorta: relevance to atherosclerosis. Annals of Biomedical Engineering 26 (6), 975–987.

[91] Tricht, I. V., Wachter, D. D., Tordoir, J., Verdonck, P., 2 2004. Hemodynamics in a compliant hydraulic in vitro model of straight versus tapered PTFE arteriovenous graft. Journal of Surgical Research 116 (2), 297–304.

[92] Tricht, I. V., Wachter, D. D., Tordoir, J., Verdonck, P., 2005. Hemodynamics and complications encountered with arteriovenous fistulas and grafts as vascular access for hemodialysis: a review. Annals of Biomedical Engineering 33 (9), 1142–1157.

[93] Tricht, I. V., Wachter, D. D., Tordoir, J., Verdonck, P., 2006. Comparison of the hemodynamics in 6mm and 4-7mm hemodialysis grafts by means of CFD. Journal of Biomechanics 39 (2), 226–236.

[94] Turek, S., Hron, J., 2006. Proposal for numerical benchmarking of fluid-structure interaction between an elastic object and laminar incompressible flow. In: Fluid-structure interaction. Springer, pp. 371–385.

[95] Turek, S., Hron, J., Razzaq, M., Wobker, H., Schäfer, M., 2011. Numerical benchmarking of fluid-structure interaction: A comparison of different discretization and solution approaches. In: Fluid Structure Interaction II. Springer, pp. 413–424.

[96] Vignon-Clementel, I. E., Figueroa, C. A., Jansen, K. E., Taylor, C. A., 2006. Outflow boundary conditions for three-dimensional finite element modeling of blood flow and pressure in arteries. Computer Methods in Applied Mechanics and Engineering 195 (29-32), 3776–3796.

[97] Vignon-Clementel, I. E., Figueroa, C. A., Jansen, K. E., Taylor, C. A., 2010. Outflow boundary conditions for 3D simulations of non-periodic blood flow and

pressure fields in deformable arteries. Computer Methods in Biomechanics and Biomedical Engineering 13 (5), 625–640.

[98] Wick, T., 2011. Adaptive finite element simulation of fluid-structure interaction with application to heart-valve dynamics. Ph.D. thesis.

[99] Wick, T., 2013. Solving monolithic fluid-structure interaction problems in Arbitrary Lagrangian Eulerian coordinates with the deal.II library. Archive of Numerical Software 1 (1), 1–19.

[100] Wick, T., July 2015. Modeling, discretization, optimization, and simulation of fluid-structure interaction. Lecture notes.
URL `http://www.sciencedirect.com/science/article/pii/B9781856176354000145`

[101] Zhuang, Y.-J., Singh, T., Zarins, C., Masuda, H., 1998. Sequential increases and decreases in blood flow stimulates progressive intimal thickening. European Journal of Vascular and Endovascular Surgery 16 (4), 301–310.